THE UNIVERSITY OF QUEENSLAND

AUSTRALIA

Oxidant stimulation of coal seams to increase coal seam permeability

Zhenhua Jing

Master of Engineering

A thesis submitted for the degree of Doctor of Philosophy at
The University of Queensland in 2018

Sustainable Minerals Institute

Abstract

Low permeability renders a significant fraction of coal seam gas (CSG) resources sub-economic. An effective permeability enhancement strategy is thereby crucial in monetising low permeability CSG resources. Though employed in a number of coal basins, conventional low permeability stimulation treatments have not been ubiquitously successful. The natural cleat system of coal is the primary conduit for gas flow and low permeability is in many cases attributed to low cleat porosity and connectivity. Cleat demineralisation by acid has been addressed previously with mixed results. This thesis explores the possibility that coal cleats could be etched and the cleat aperture could be widened by use of oxidants. It could have high potential to increase the cleat porosity and connectivity, thus enhancing the coal permeability in the near well bore region where high permeability is critical.

Two coal samples, from the Bowen (coal B) and Surat (coal S) basins in Queensland, Australia were selected. A screening method was designed based on time-lapse photography to assess the extent of coal particle size change immersed in potential oxidants, including sodium hypochlorite (NaClO), potassium permanganate ($KMnO_4$), hydrogen peroxide (H_2O_2), and potassium persulfate ($K_2S_2O_8$). Results show coal solubilisation and the propensity to swell in all the oxidants as well as coal breakage in specific oxidants (NaClO and $KMnO_4$). Both coals react vigorously with NaClO and $KMnO_4$, where massive coal solubilisation occurs, but react only slightly with $K_2S_2O_8$ and H_2O_2. Given the solid products of the $KMnO_4$ reaction (MnO_2), NaClO is selected as the most promising oxidant stimulant.

After NaClO treatment, the total accessible pore volume of both coals increases. Pore size distributions indicate that oxidation can enlarge the pores, particularly for coal S, which was confirmed by scanning electron microscopy (SEM). A microfluidic cleat flow cell (CFC) was used to inject NaClO into artificial channels scribed on polished coal samples, and measured an increase in the widths of the channels after NaClO treatment. The channel aperture increase indicates that coal solubilisation/etching is a more dominant mechanism than coal swelling when coal is confined in coal cleats. The channel aperture of coal S increases more than coal B.

To chemically interpret the various NaClO oxidation effects on different coals, molecular structures of the two studied coals and their oxidised residues (coal So and coal Bo) were examined using Fourier transform infrared spectroscopy (FTIR), X-ray photoelectron spectroscopy (XPS) and solid state ^{13}C nuclear magnetic resonance spectroscopy (^{13}C NMR). The results qualitatively and quantitatively illustrate that NaClO preferentially reacts with aliphatic chains and oxygen functional groups. After aliphatic chains, NaClO tends to attack small aromatic rings, evidenced by the loss of smaller clusters in coal S, leaving the larger aromatic clusters in the oxidised residue. The oxidised coal B turned out to have a similar molecular structure with coal S. Indeed, the subsequent oxidation of coal Bo gave a similar mass loss (42.5%) to raw coal S (45.2%). Futuremore, NaClO oxidation products were rich in carbonyl (C=O) and carboxylic (O-C=O) functional groups.

Finally, based on coal B, the coal permeability variations after oxidation were examined with core flooding tests under confining pressure and the corresponding coal structure changes were compared using X-ray microcomputed tomography (μCT). NaClO oxidation was found to etch the cleat surface, widen cleat aperture and generate new horizontal fractures and/or void space. Nevertheless, these structural changes did not lead to a vertical permeability increase, which is proposed to be due to fines generation and blockage of cleats in the unreacted area. However, the horizontal permeability was found to increase under confining pressure. Minerals may play a role in acting as pillars to hold the cleat aperture when the cleat is etched and widened. Furthermore, NaClO oxidation is lithotype independent and attacks the coals that are more porous or have initial fractures.

This thesis has confirmed the potential of oxidant stimulation to benefit coal permeability. Some uncertainties remain. For example, given the high heterogeneity of coal, flooding tests with different coal types should be conducted to establish relationships between permeability change and specific coal properties. In the future, the oxidant stimulation targeting at lower rank coals is expected to show substantial permeability increase as NaClO can cause substantial etching of cleats in lower rank coals.

Declaration by author

This thesis is composed of my original work, and contains no material previously published or written by another person except where due reference has been made in the text. I have clearly stated the contribution by others to jointly-authored works that I have included in my thesis.

I have clearly stated the contribution of others to my thesis as a whole, including statistical assistance, survey design, data analysis, significant technical procedures, professional editorial advice, financial support and any other original research work used or reported in my thesis. The content of my thesis is the result of work I have carried out since the commencement of my higher degree by research candidature and does not include a substantial part of work that has been submitted to qualify for the award of any other degree or diploma in any university or other tertiary institution. I have clearly stated which parts of my thesis, if any, have been submitted to qualify for another award.

I acknowledge that an electronic copy of my thesis must be lodged with the University Library and, subject to the policy and procedures of The University of Queensland, the thesis be made available for research and study in accordance with the Copyright Act 1968 unless a period of embargo has been approved by the Dean of the Graduate School.

I acknowledge that copyright of all material contained in my thesis resides with the copyright holder(s) of that material. Where appropriate I have obtained copyright permission from the copyright holder to reproduce material in this thesis and have sought permission from co-authors for any jointly authored works included in the thesis.

Publications included in this thesis

1. Jing, Z., Balucan R.D., Underschulatz, J.R., Steel K. M., 2018. Oxidant stimulation for enhancing coal seam permeability: Swelling and solubilisation behaviour of unconfined coal particles in oxidants. *Fuel*, 221, 320-328.

Publication citation – incorporated as Chapter 3.

Contributor	Statement of contribution	Percentage contributed
Zhenhua Jing	Designed and conducted experiments Interpretation of results Wrote the paper	75%
Reydick D. Balucan	Designed the experiments Interpretation of results	5%
Jim R. Underchultz	Edited the paper Interpretation of results	5%
Karen M. Steel	Edited the paper Interpretation of results	15%

2. Jing, Z., Mahoney, S.A., Rodtigues, S., Balucan R.D., Underschulatz, J.R., Esterle J.S., Rufford, T. E., Steel K. M., 2018. Oxidant stimulation for enhancing coal seam permeability: Effects of sodium hypochlorite oxidation on subbituminous and bituminous Australian coals, *International Journal of Coal Geology*.

Appears in Chapter 3 and Chapter 4.

Contributor	Statement of contribution	Percentage contributed
Zhenhua Jing	Designed and conducted experiments Interpretation of results Wrote the paper	60%
Shilo A. Mahoney	Designed the experiments Interpretation of results	5%
Sandra Rodrigues	Characterised the samples Interpretation of results	5%
Reydick D. Balucan	Interpretation of results	5%

Jim R. Underschultz	Edited the paper	5%
Joan S. Esterle	Edited the paper	5%
Thomas E. Rufford	Edited the paper	5%
Karen M. Steel	Edited the paper Interpretation of results	10%

Submitted manuscripts included in this thesis

1. Jing, Z., Rodrigues S., Strounina, E., Li, M., Wood, B., Underschultz, J.R., Esterle J.S., Steel, K.M., 2018. Use of FTIR, XPS, NMR to characterize oxidative effects of NaClO on coal molecular structures, *International journal of coal geology*.

Appears in Chapter 5.

Contributor	Statement of contribution	Percentage contributed
Zhenhua Jing	Designed and conducted experiments Interpretation of results Wrote the paper	65%
Ekaterina Strounina	Conducted the NMR experiments Edited the paper	10%
Mengran Li	Conducted the FTIR experiments Edited the paper	5%
Barry Wood	Conducted the XPS experiments	5%
Jim R. Underschultz	Edited the paper	5%
Karen M. Steel	Edited the paper Interpretation of results	10%

Other publications during candidature

1. Jing, Z., Balucan R.D. Underschulatz, J.R., Steel K. M., 2016. Oxidant stimulation for enhancing coal seam permeability: Swelling and solubilisation behaviour of unconfined coal particles in oxidants. *China-Australia Unconvential Natural Gas Forum, China*.

2. Jing, Z., Mahoney, S.A., Rodtigues, S., Balucan R.D., Underschulatz, J.R., Esterle J.S., Rufford, T. E., Steel K. M., 2017. Oxidant stimulation for enhancing coal seam permeability: Effects of sodium hypochlorite oxidation on subbituminous and bituminous Australian coals, *The Society for Organic Petrology's 34th Annual Meeting*, Canada.

Contributions by others to the thesis

The coal petrographic analysis was conducted by Dr Sandra Rodrigues, School of Earth and Environmental Science, UQ.

In Chapter 4, the cleat flow cell was designed and updated by Dr Shilo A. Mahoney, School of Earth and Environmental Science, UQ. The SEM images were taken by Mr Jinxuan Zhang, School of Chemical Engineering, UQ.

In Chapter 5, the leaching tests of the two studied coals after oxidation were conducted by Mr Ziqiang Liu, School of Chemical Engineering, UQ. The FTIR, XPS and NMR experiments reported were conducted by Dr Mengran Li, School of Chemical Engineering, Dr Barry Wood, Centre for Microscopy and Microanalysis, and Dr Ekaterina Strounina, Centre for Advanced Imaging, respectively.

The core flooding rig in Chapter 6 was designed and built by Dr Luc G. Turner and Dr Reydic D. Blucan, School of Chemical Engineering, UQ. The CT scanning was conducted by Dr Karine Mardon, The Centre for Advanced Imageing, UQ.

Dr Karen M. Steel and Prof Jim R. Underschultz assisted in the drafting of this thesis.

Statement of parts of the thesis submitted to qualify for the award of another degree

None.

Research Involving Human or Animal Subjects

No animal or human subjects were involved in this research.

Acknowledgements

I would like to thank my supervisors Dr Karen M. Steel and Jim R. Underschulatz, for their encouragement, insightful guidance and positive support. I am grateful to the research opportunity they provided and feel so lucky for always having a very happy discussion atmosphere with them not only in the research area but also for my personal development. Thanks to the support from the Centre for Coal Seam Gas, the School of Chemical Engineering and the Sustainable Minerals Institute. Special thanks to the China Scholarship Council for providing me the scholarship to study in The University of Queensland.

I must also thank the members of my research group for their insightful advice including Prof Victor Rudolph, Prof Brian Towler, Prof Joan Esterle, Dr Tom Rufford, Dr Reydick Balucan, Dr Sandra Rodrigues, Dr Shilo Mahoney, Dr Luc Turner, Dr Robin Dawson, Dr Lei Ge, Ms Lauren Zappala, Dr Syed Raza, Dr Fei Ren. Thanks must also be given to Mr Jinxuan Zhang, Dr Mengran Li, Dr Karine Mardon, Dr Ekaterina Strounina, Dr Barry Wood, Mr Ziqiang Liu for providing support in the experimental design and conduction.

I would also like to extend my deepest thanks to my friends in UQ, Brisbane, especially those who came Australia together with me. I have to put your name here, Dr Xiaoxiao Li, Mr Qi Zuo, Dr Zhe Ren, Dr Yue Xi, Dr Jianhui Qi, Mr Yihang Ding, Dr Shuai Gao, Dr Huihuang Chen, Dr Ziyong Chang, Dr Wei Huang. I really appreciate the time with my teacher and friend Dr Xiaoming Wang. Studying abroad is a really tough and difficult period, but you have made the life so enjoyable and easily bearable with your genius and brilliant sense of humour. I will miss this time with you and hope you all a promising future.

Absolutely to my grandparents and parents, during my 10 years away from home for study, it is your incredible understanding and never-ending support that make it possible. Finally, a special appreciation to Dr Yujian Wang for your listening and understanding of the tough time in my research and life. Those days and nights, when we shared our happiness and sorrow will be my precious memories. Thank you. Best wishes!

Financial support

This research was supported by Centre for Coal Seam Gas, The University of Queensland and its industry partners APLNG, Arrow Energy, QGC and Santos as well as the China Scholarship Council.

Keywords

Coal seam gas, permeability, oxidant stimulation, sodium hypochlorite (NaClO), coal porosity, cleat aperture, molecular structure

Australian and New Zealand Standard Research Classifications (ANZSRC)

ANZSRC code: 091406, Petroleum and Reservoir Engineering, 60%
ANZSRC code: 040309, Petroleum and Coal Geology, 40%

Fields of Research (FoR) Classification

FoR code: 0914, Resources Engineering and Extractive Metallurgy, 70%
FoR code: 0499, Other Earth Sciences, 30%

Contents

List of Figures

List of Tables

List of Abbreviations used in the thesis

ATR-FTIR: Attenuated total reflectance Fourier transform infrared spectroscopy

BDE：Bond dissociation energy

CFC: Cleat flow cell

CSG: Coal seam gas

CT: X-ray computed tomography

GC-MS: Gas Chromatography-Mass Spectrometer

GU: greyscale unit

ICP-OES: Element concentration analysis via inductively coupled plasma optical emission spectroscopy

MIP: Mercury intrusion porosimetry

NMP: N-methylpyrrolidone

NMR: Nuclear magnetic resonance spectroscopy

P_1: Inlet pressure

P_2: Outlet pressure

P_c: Confining pressure

P_e: Effective pressure

PSD: Particle size distribution

SEM-EDS: Scanning electron microscopy -Energy dispersive x-ray spectroscopy

S_R : Swelling ratio

S_r : Swelling rate

TOC: Total organic carbon

VF: void space fraction

MF: Mineral fractin

XPS: X-ray photoelectron spectroscopy

XRD: X-ray diffraction

Chapter 1. Introduction

1.1 Motivation and background

Commercial extraction of methane from coal seams is now well established in a number of countries throughout the world, including the USA, China, Australia, Canada and India [1]. Permeability of coal seams is a key controlling factor for gas migration in coal reservoirs and is often a critical technical barrier preventing economically viable gas production [2]. Therefore, permeability enhancement can be a crucial mitigation strategy to monetise CSG resources.

Low permeability stimulation treatments primarily consist of hydraulic fracturing and multi-lateral horizontal wells [3]. Though employed in a number of coal basins, these coal seam permeability enhancing methods have not been ubiquitously successful [4, 5]. The associated damage to the coal formation, fines migration due to shear failure during hydraulic fracturing, and stress dependent permeability reduction including proppant embedment can significantly reduce the fracture connectivity and thus effective coal permeability [6, 7]. The efficiency of horizontal wells is sometimes decreased by hole collapse, particularly when drilling underbalanced or drilling through depleted coal seams [5]. Some studies have been conducted with respect to the thermal enhancement of permeability [8] which is, however, only at the theoretical stage and currently remains sub-economic. Alternative stimulation approaches are desirable for increasing the gas extraction from coal seams.

Chemical stimulation, therefore, has attracted increasing interest recently, which includes acid stimulation and oxidant stimulation [9-11]. The former targets at removing the minerals from the cleats, while the latter is dedicated to dissolve the coal matrix to etch the initial cleat surface and/or generate new fractures to increase cleat apertures in the near wellbore region which plays a crucial role in dictating long-term productivity.

For low permeability coal seams with highly mineralised fractures, dissolution of mineral occlusions will likely increase fluid flow capacities [9-11]. Vasyuchkov (1985) reported aqueous HCl (2, 4 and 6%) solutions could enhance the coal permeability dramatically from less than 0.1 mD to over 15.1 mD [12]. Turner et al (2016) conducted the core flooding tests with coal samples containing various cleat and mineralogical properties. The permeability enhancement results are mineral type dependent and the increases in permeability can be achieved where cleats are rich in carbonates, however, the presence of clays may place limitations on the extent of enhancement.

Balucan et al. (2016) investigated the effect of mineral alteration by hydrochloric and hydrofluoric acid (HCl-HF) on fracture compressibility and coal permeability. Coal core immersion in 15% HF- 4% KCl solution enhanced coal permeability and reduced fracture compressibility. The overall findings show that mineral alteration by HF yielded relatively large, crystalline minerals that appeared to provide structural support to fractures, resulting in enhanced fluid flow and improved resistance to compression. Later, Balucan et al. (2018) investigated the acid-induced physical and chemical changes in core samples to gain improved understanding of permeability enhancement in the vertical flow direction [13]. There was clear evidence for cleat opening via mineral dissolution as well as mineral mobilization-accumulation. Based on the X-ray microcomputed tomography (μCT) image analyses, they conducted flow simulation and reported that acidizing could enhance permeability not only in the vertical direction but also in the lateral or horizontal direction [13]. Similarly, Ramandi et al (2018) applied the μCT and numerical simulation to investigate the effect of dissolution of syngenetic and epigenetic minerals on coal permeability and they reported that coal permeability increase depends significantly on epigenetic mineral dissolution, and secondarily on syngenetic mineral dissolution [14].

Although the above studies have examined the effect of acidization on coal permeability experimentally and numerically, problems still exist. For example, few results relate to the horizontal permeability which is parallel to the face cleats and more relevant than vertical permeability. Additionally, in the core flooding tests conducted by Turner et al. (2016), the HCl was injected at the same direction with brine [11], which, to mimic how stimulation would be conducted downhole, should be to adopt forward flow to characterise initial permeability, reverse flow with acid to simulate the downhole treatment, and then forward flow again to characterise the final permeability.

Alternatively, oxidants could have potential to increase the coal cleat aperture by etching the coal cleat surface or dissolving a portion of the coal matrix. The schematic oxidant stimulation diagram is shown in Figure 1-1. The oxidant stimulation in the vicinity of the wellbore could increase the coal seam permeability and potentially improve the gas production. In addition, weakening the coal matrix by oxidant reactions may also prove applicable as a pre-hydraulic fracturing conditioning process. Coal oxidation has been studied in coal structure investigations [15-17], desulfurization [18, 19] as well as organic chemical extraction from coal [20, 21]. This research has provided abundant knowledge to facilitate understanding of coal oxidation procedures and mechanisms. However, using the oxidant to enhance coal seam permeability is a novel area with very little research. Therefore, the current study is of particular importance, not only in the CSG area to investigate the novel alternative stimulation method to increase coal permeability, thereby increasing CSG production, but also the knowledge obtained in this study could fill the gap in the research of coal oxidation.

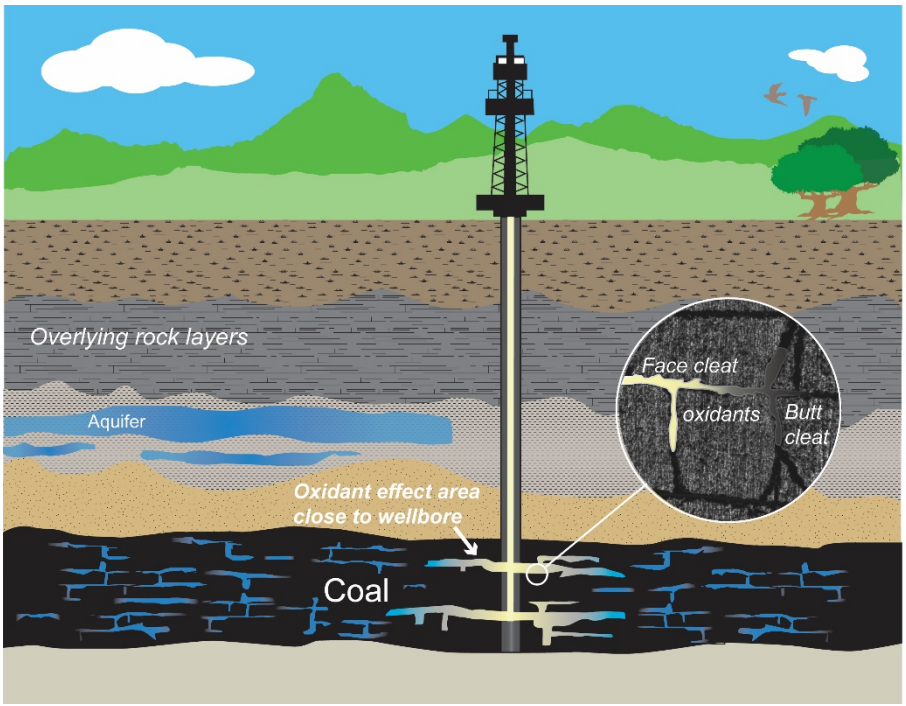

Figure 1-1.Schematic oxidant simulation diagram

1.2 Thesis objectives and outline

The primary objective of this thesis is to investigate the permeability enhancement potential of oxidant stimulation and its mechanisms. The specific objectives of this thesis are as follows:

Objective 1: Investigate coal behaviors in various oxidizing chemicals to select the most promising oxidant.

Objective 2: Investigate the effect of oxidation on coal structures including coal pores and cleats, especially the cleat aperture.

Objective 3: Identify the different oxidation effects associated with the different coal types, including the coal rank, and lithotype.

Objective 4: Understand the molecular structural difference between coals and provide knowledge about the coal oxidation mechanism from a chemistry view.

Objective 5: Evaluate the permeability stimulation potential of the oxidant candidate and examine the permeability variation mechanism.

This thesis is structured into seven chapters, including this introductory chapter. Chapter 2 presents a literature review of coal fundamentals, coal permeability, difficulties associated with current stimulation techniques and the potential of chemical stimulation treatments to enhance coal permeability. Chapter 3 to chapter 6 are developed to complete the above objectives and a thorough experimental plan is designed in each chapter corresponding to various research targets.

Chapter 3 focuses on the coal behaviours in different oxidants to quickly highgrade the promising oxidants and understand the possible coal reactions contacting with oxidants. A swelling/shrink test was developed here based on the optical observation.

After the determination of the optimal oxidant candidate, chapter 4 investigates the oxidative effect on coal properties including coal pores and coal cleat system. Two different rank coals are involved in this chapter, and their different reactions with the oxidant are reported. A cleat flow cell rig is used to measure the cleat aperture change after oxidation and mercury

intrusion porosimetry and scanning electron microscopy (SEM) are used to examine the oxidative effect on pores.

Chapter 5 compares the different molecular structures between the two different coals and also investigates the change on their molecular structures due to oxidation. Attenuated total reflectance Fourier transform infrared spectroscopy (ATR-FTIR), X-ray photoelectron spectroscopy (XPS) and solid state ^{13}C nuclear magnetic resonance spectroscopy (^{13}C NMR) are used in this chapter.

Chapter 6 describes the results of permeability variation and physical structure change after acid stimulation and oxidant stimulation for coal core samples (76 mm in diameter) and cube samples (40*40*40mm) to develop a fundamental understanding of the mechanisms controlling permeability changes. To accomplish these goals, the core flooding apparatus and X-ray computed tomography (μCT) were incorporated.

Finally, chapter 7 provides a summary of thesis conclusions and recommendations for future work.

Chapter 2. Literature Review

2.1. Coal Molecular Representation

The structure of coal is inherently complex and varies widely depending on the climate at the time of accumulation, origin constituent components, geological history age and rank of the particular coal examined [22].

Since 1942, when one of the first 2D models for coal was generated, more than 100 proposed molecular level representations of coal have been reported [23]. In the 1960's, coal chemists attempted to create models of coal structure which would represent and ''average structural unit'' of coal organic matter. By the 1970's, a general view suggested that coal organic matter might show a cross-linked polymer nature based on the observation that insolubility of coal was similar with the manmade cross-linked polymers that formed three-dimensional networks [24]. The molecular models developed at that time were typically based on clusters. Clusters are molecular substructures consisting of, on average, three or four fused aromatic rings that contain appropriate numbers of O, N, and S atoms and have attached short-chain aliphatic groups. The clusters are connected together by hydro-aromatic, etheric, or short aliphatic linkages [22]. For example, Figure 2-1 is a coal molecular representation adapted from Wender [25]. Later, with the development of computer science, more complicated coal molecular structures were constructed and the first computational 3D representations of coal models were reported by Carlson (1992) [22]. Figure 2-2 is an anthracite coal molecular representation adapted from Pappano et al [26].

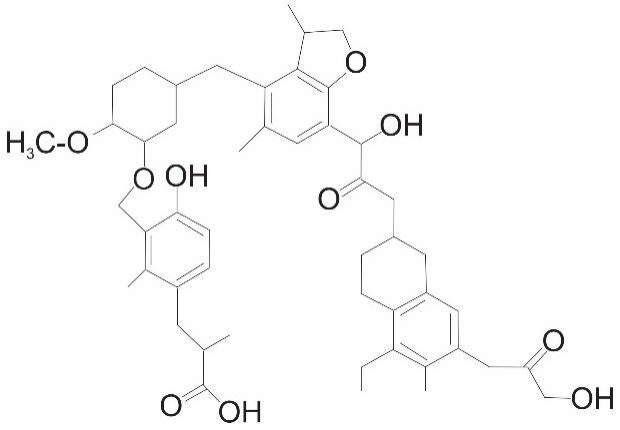

Figure 2-1: Coal molecular representation adapted from Wender [25]

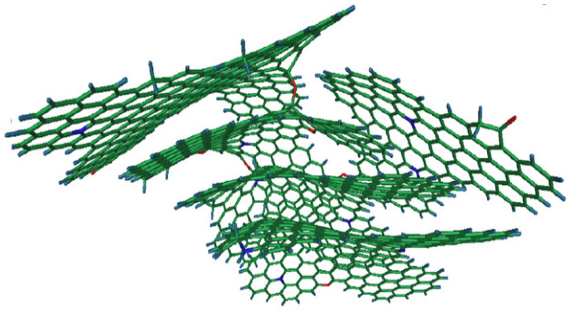

Figure 2-2: Molecular representation of Anthracite, adapted from Pappano et al [26]

Although the possible network structures for coal have been extensively studied using various analytical and experimental methods, the true nature of the structure is still elusive. It is commonly accepted that coal is a three-dimensional macromolecular network structure consisting of polyaromatic and alkyl substituted aromatic units linked by covalent and noncovalent bonds (hydrogen bonds, van der Waals interactions, electrostatic interactions and π–π interactions) [27]. Determining the network structural extent of coal is important for the development of more representative molecular models and to simulate the fundamental principles of coal utilization processes. Two kinds of network structures have been proposed, non-associative (covalent) and associative (noncovalent) network structures (Figure 2-3) [28-30].

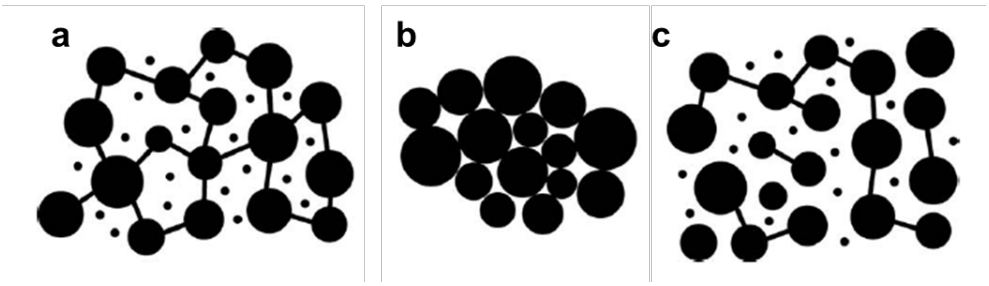

Figure 2-3: Non-associated (left) and associated (middle) and combined (right) molecular network coal structures (adapted from Nishioka [28] and D. V. Niekerk [29])

The non-associative structure model [28], also named as covalent network model [30], consists of a covalently bonded macromolecular system (much like a cross-linked polymer). This network should be relatively insoluble in organic solvents with relatively small amounts of solvent–soluble, low molecular weight substances trapped within the networks. This model, also known as the two phase model, consists of a macromolecular structure and a mobile phase (trapped low molecular weight compounds). The observation that a large portion of coal is typically insoluble has been used to support the validity of this model [23].

Recently, the associate (non-covalent) network model was proposed wherein coal consists of only coal molecules but form huge associates. In the associative structure model, it is assumed that coal consists of various molecules bonded together by noncovalent bonds such as hydrogen bonds, π–π interactions between aromatic rings, Van der Waals interactions, and electrostatic interactions forming a network of associates of coal molecules. The importance of Van der Waals and hydrogen bonds in the formation and stabilization of coal macromolecular structure is widely studied [30]. Carlson (1992) suggested that the relative importance of Van der Waals interaction and hydrogen bonding may be dependent on coal rank and Van der Waals interactions were responsible for most of the stabilization in coal [22]. But Iino Masashi thought hydrogen bonds, π–π interactions between aromatic rings, electrostatic and charge transfer interactions are associative interactions rather than weak Van der Waals interactions [30]. This structure is supported by the high solvent extraction yield obtained from some bituminous coals. It has also been suggested that the network structure may consist of entangled chains [30].

Based on the description above, D.V Nerkiek suggested that coal probably has a combined structure, consisting of both associated and non-associated components. In the combined

structure, coal consists of a distribution of various sized molecules (small to very large macromolecules) in an associated (secondary interactions) and entangled structure [29].

It is clear that the structure of coal is inherently complex and varies widely [23]. Although many 2D and 3D coal molecular models have been proposed in the literature, the majority of these models were generated with whole coals as the basis for the structural elucidation. This severely affects the accuracy of the structural model as coal molecular structures differentiate for different coal maceral compositions and coal ranks [31, 32]. Furthermore, it should be noted that even within a single maceral or the same rank, there could be numerous possible models. Jonathan P. Mathews et al. (2001) presented the molecular model of vitrinites from the upper Freeport and Lewiston-Stockton coal seams, only utilizing pure telocollinite which reduced the complexity of the model and resulted in more realistic molecular structures than those from whole coal analyses. The differences in the structure are significant despite the two vitrinites being very close in maturation [33]. This was in agreement with the statistical research results by Faulon (1993), who reported that there are numerous possible models, even within a single maceral and rank [34].

Van Niekerk D. et al. (2010) also used High-resolution transmission electron microscopy (HRTEM) to determine the different size and distribution of aromatic fringes in vitrinite and inertinite-rich coals from South Africa. They found that the inertinite-rich coal model was more aromatic with a larger portion of the aromatic carbons polycondensed and the vitrinite-rich coal model was more aliphatic and contained more aliphatic side chains and longer aliphatic crosslinks [29]. Patrakov et al. (2005) constructed the structure of a liptinite-rich Barzas coal by means of a molecular modelling software and the model structure corresponded to the mean formula $C_{727}H_{790}N_2S_4O_{36}$ and to a molecular weight of 10,260 g/mol (amu) [35]. Liu et al. (2013) used the oxidation method to investigate the structural features of Shengli lignite, and the results suggest that Shengli is rich in condensed aromatic species and hydroxyl-, methoxy-, and/or methyl-substituted benzene rings, and $–CH_2CH_2–$ is a dominant bridged linkage connecting aromatic rings in Shengli lignite. Aliphatic linkages connecting three aromatic rings also exist in this coal [17].

2.2 Pores and Cleats or Fractures in Coal

Cleat or fracture permeability and matrix porosity of the coal can extremely affect the successful production of coalbed gas. Coal reservoir performance is controlled by pores and

their ability to diffuse gas into the adjoining cleat or fracture system where Darcy flow of gas and water then governs gas transport to production wells. The density of pores (e.g. micropores) and their connectivity in coal matrix can influence the pores capacity to diffuse gas. More importantly, the productivity of the coal reservoir may be affected by this relationship between the cleats or fractures and pore systems during gas desorption and production.

2.2.1 Pores in Coal

The amount of pores in coal, as described by Moore (2012), is the single most important property that makes coal a unique reservoir among the unconventional and conventional reservoirs. Also, what is unique to coal is that the majority of the gas is adsorbed in the porosity system in the coal matrix. It should be noted that a large part of the volume adsorbed in the matrix is held in micropores in contrast to mesopores and macropores [36]. On the basis of the pore sizes distributions, the pore system is classified in increasing size class as micropores of <2 nm (nanometer), mesopores (2-50 nm), and macropores (>50 nm) [37, 38].

Porosity is mainly related to the coal composition and rank. In terms of the relationship between porosity and the maceral composition, the research results conducted by different researchers are not consistent due to the difference of the studied samples, the different measuring methods and sometimes even the different coal size classification standards. For example, Mastalerz (2008) reported that vitrinite maceral predominantly contains micropores and inertinite mostly contains mesopores and macropores[39, 40]. But Harris and Yust (1976) reported that vitrinite is mainly composed of micropores and mesopores, inertinite of mesopores, and liptinite of macropores. These researchers concluded that inertinite is the most porous (predominant macropores) maceral group and liptinite is the least porous [41]. However, it is generally accepted that Vitrinite content is the most important maceral composition because of high internal surface area due to the abundant microporosity [39].

Gan et al. (1972) described coal porosity in a series of coal samples from lignite to anthracite coals. They concluded that pore volume and frequency are controlled by rank [37]. The average pore size of low-rank coals is larger than that of high-rank coals [39]. A report by Rodrigues and Lemos de Sousa (2002) indicated that high-volatile bituminous A and higher

rank coals are dominated by micropores. The high-volatile bituminous C and B coals are dominated by mesopores. Lignite and subbituminous coals are dominated by macropores [40]. However, Parkash and Chakrabartty (1986) argued that micropores instead of macropores are significant in low rank coals, which continues to be debated [41].

The correlation of the porosity volume with coal rank expressed by carbon content (air-dried basis) shown in Figure 2-4 [40] and Figure 2-5 [42]. In lower rank coals, porosity is high and mainly attributed to macropores and that geophysical factors, such as compaction and water expulsion, progressively reduce porosity. At about low-volatile bituminous coal rank, with the formation of meso-and micropores, the porosity increases. This increase of porosity is due to progressive changes in the molecular structure through higher ranks. Moore (2012) demonstrated a detailed relationship of micropores and macropores (Figure 2-5) [36]. In general, macropores increase with decreasing coal rank and micropores increase with increasing rank.

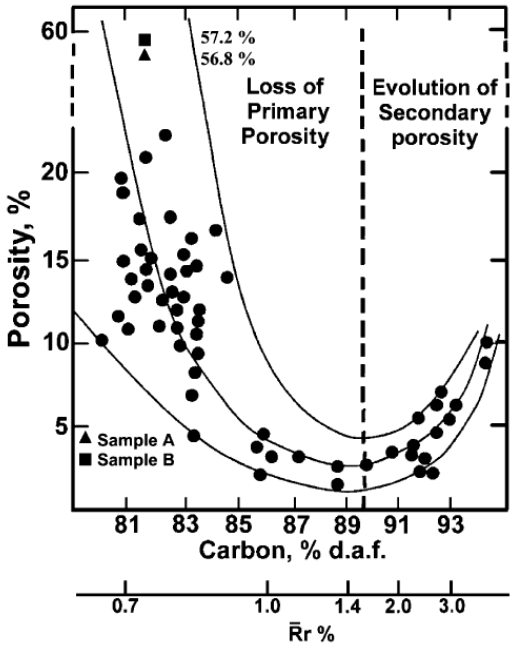

Figure 2-4: Relationship between coal porosity and coal rank (modified from C.F. Rodrigues, 2002 [40]).

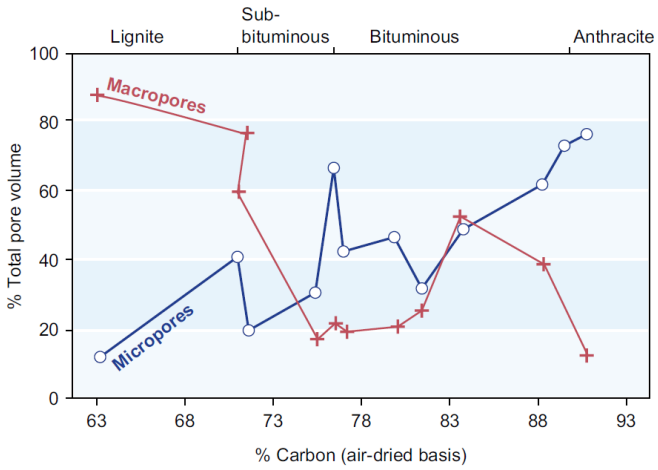

Figure 2-5: Diagram showing relationship of percentage total pore volume, percentage carbon on air-dried basis, and coal rank with micropores and macropores (Tim A. Moore, 2012 [42]).

The origin of coal matrix pores is not too well understood except that they may be inherited from the original peat structures and formed during coalification. Macropores (Figure 2-6) are probably voids or spaces of residual cell structures of precursor plants or in the maceral detritus, which may be termed primary pores [43, 44]. The origin of mesopores is very similar to the macropores, some of which may be smaller compressed macropores [43]. Therefore, macropores and mesopores are related to the original cellular structures of the plant remains or primary pores. The origin of micropores is probably related to the intermolecular spaces in the coal macromolecular structures (e.g. nanopores) developed by gelification of the organic matter during coalification and compression of some primary pores to smaller pores [43, 45]. Thus, the origin of micropores is controlled by coalification or is coal rank sensitive and may be secondary in origin. In general, the percentage total volume of micropores sharply increases and that of macropores sharply decreases from lignite to anthracite coals [2].

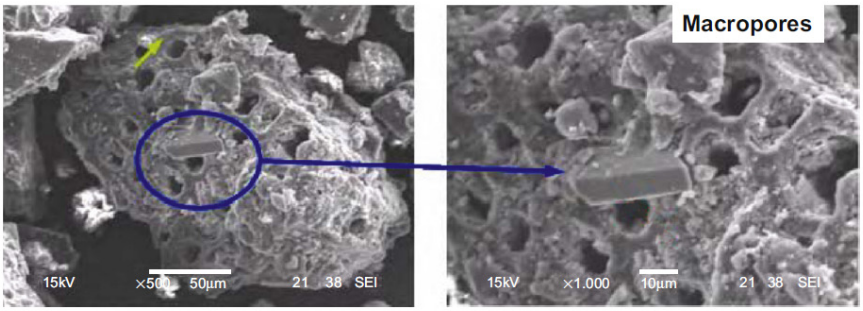

Figure 2-6: Scanning electron microscope images showing very large pores (>10µm) of coal; magnification: 500× for left image and 1000× for right image. Source: Adapted from Lin (2010) [44].

2.2.2 Cleats and Fractures

2.2.2.1 Origin of cleats

Cleats or fractures in coal are the controlling parameter of permeability. Unlike the origin of porosity, which inherently originates within the organic matter and structures, the origin of the cleat or fracture system is unrelated to the organic matter composition. Many workers have proposed dual origins of cleats: (1) inherent to progressive coalification and burial or endogenetic causes and (2) tectonic stresses during deformation or exogenetic causes [46-48]. Other workers suggest a combination of both causes [49, 50].

1) Endogenetic cleats

Endogenetic cleats are early features formed during increased coalification with progressive loss of moisture, which caused desiccation of coal [51]. Another proposed cause of endogenetic cleats is differential compaction causing folding around interbedded channel sandstones (Figure 2-7) [50].

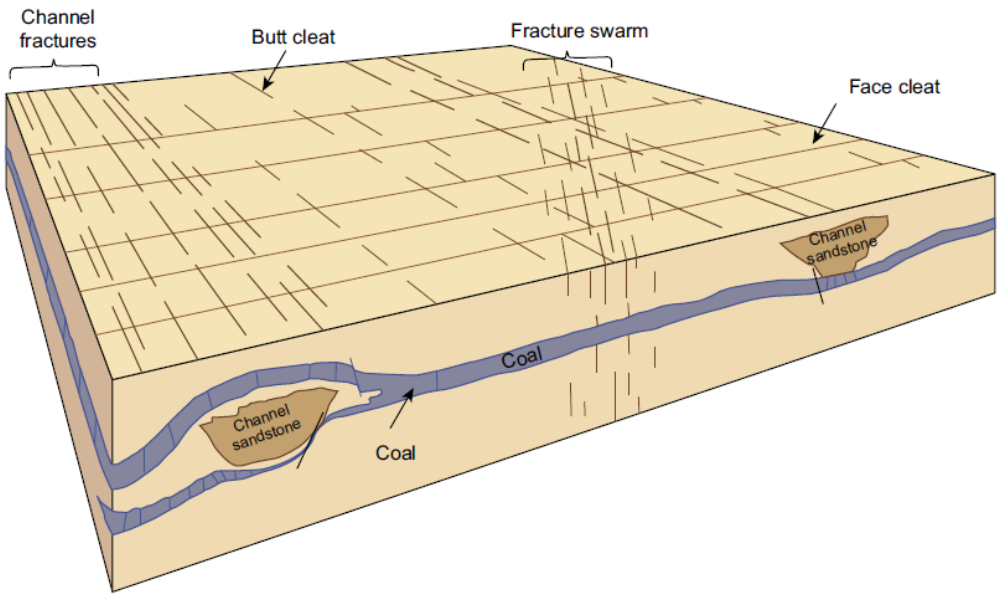

Figure 2-7: Face and butt cleat patterns and fractures associated with compactional folds around channel sandstone resulting from differential compaction (adapted from Laubach et al., 1998 [50])

① Shrinkage from Loss of Moisture

Loss of moisture during progressive coalification is demonstrated by that about 65% bed moisture loss from peat to subbituminous A coal or to high-volatile bituminous C coal [52]. Law (1991) proved the shrinkage in coal caused by moisture loss by the evidence that it is coincident between vitrinite reflectance versus cleat spacing and vitrinite reflectance versus bed moisture [53]. In addition, Law (1993) described that cleat spacing decreased with coal rank as a function of loss of moisture [54]. Another factor, related to shrinkage, is the elevated pore pressure during the development of cleats in coal. Secor (1965) also proposed that the development of cleats in coal is caused by high fluid pressure [55]. Ryan (2002) suggested that cleats are related to shrinkage of the bulk coal caused by loss of both moisture and volatile matter during coalification [56]. Figure 2-8 (modified from Ryan) shows the decrease of percentage volume with increasing rank by using average inherent water and as-received volatile matter contents for different ranks starting with lignite.

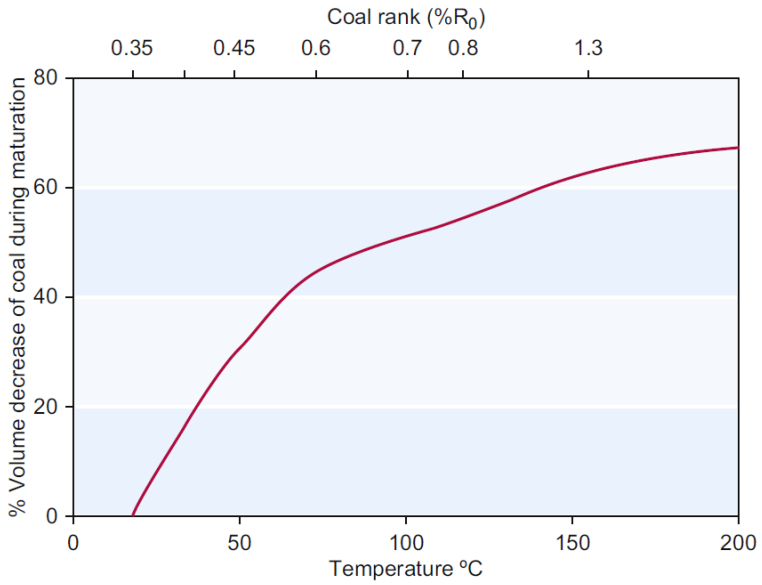

Figure 2-8: Diagram showing estimate of coal volume decrease related to rank expressed in vitrinite reflectance (modified from Ryan, 2002 [56])

② Differential compaction

A second mode for formation of endogenetic cleats is differential compaction during burial. Differential compaction of interbedded channel sandstones, fine-grained siltstone and mudstone, and coal beds promotes development of coal cleats or fractures, master joints, and microfaults below and above the sandstone geobodies (Figure 2-7). This stratigraphic

relationship between channel sandstones and intervening fine-grained clastics and coal beds is well illustrated in the Paleocene Fort Union Formation in the Powder River Basin, Wyoming, United States (Figure 2-9 A; Flores, 1986). The differential compaction between the channel sandstone and interbedded siltstone, mudstone, and coal produced about 40% reduction of the interval along the margins of the channel sandstone. The coal beds below and above the thickest part of channel sandstones are densely cleated or fractured (Figure 2-9 B) [57].

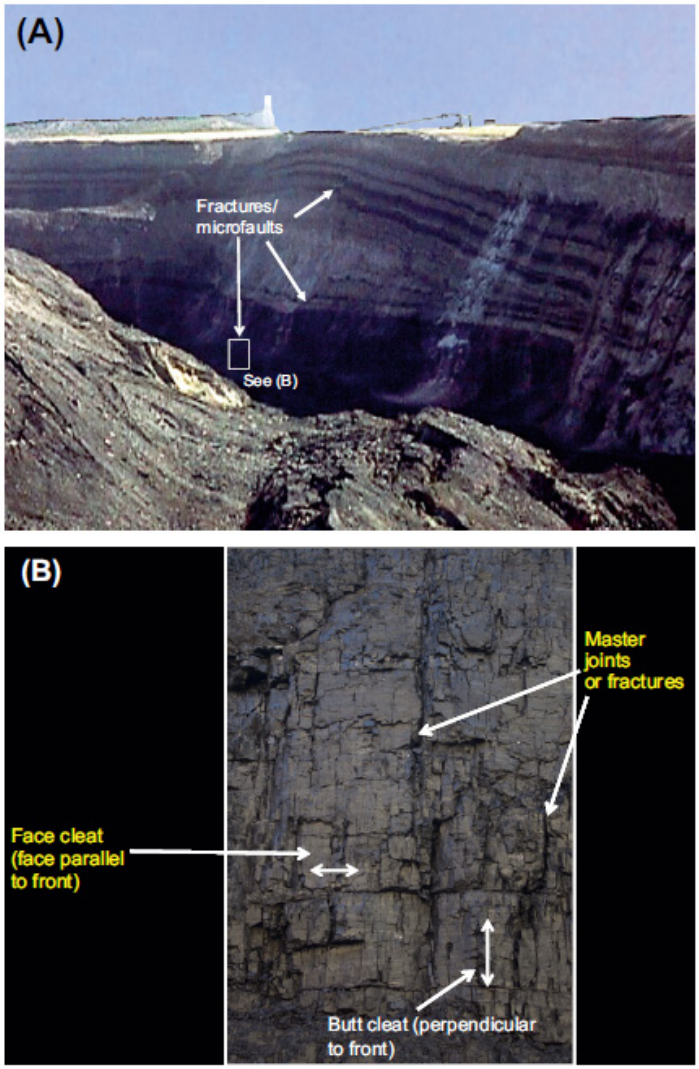

Figure 2-9: Photographs showing (A) fold around a fluvial channel sandstone due to differential compaction and (B) coal cleats and master joints formed directly below the sandstone in the Powder River Basin, Wyoming, United States (modified from flores, 1986) [57].

2) Exogenetic Cleats

The causes of exogenetic cleats or fractures are not straightforward because of typically multiple generations of formation due to complex geology, tectonic deformations, and local structural conditions. Laubach et al. (1998) in reviewing the origin of exogenetic cleats, proposed the following potential causes: i. a thermoelastic response of coal to regional tectonic extension and/or uplift of the basin and surrounding areas, ii. stress from disturbances due to local folding and faulting [50].

2.2.2.2 Characteristics of cleats

Cleat or fracture systems in coal consists of two virtually orthogonal sets of face and butt cleats. The 'face cleat' is the dominant fracture system whereas the 'butt cleat' is less laterally continuous and perpendicular with the face cleats. Butt cleats always terminate where they intersect a face cleat (Figure 2-10) [2, 52]. The attributes of cleats in coal include aperture, length, spacing, height, frequency (density), and connectivity (Figure 2-10). These attributes control the permeability, which in turn, influence the productivity of gas from coal reservoirs.

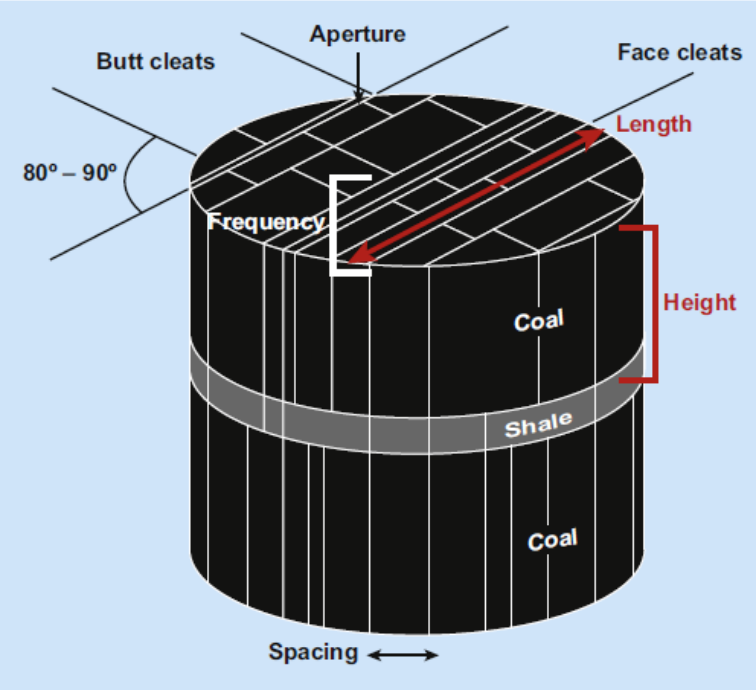

Figure 2-10: Diagram of an idealized coal core showing idealized face and butt cleat system consisting of aperture, length, height, spacing and frequency (source from Flores, 2013 [52]).

(1) Coal cleat aperture is the width of the crack and is microscopic to macroscopic in size [58]. It is one of the important parameters controlling permeability in coal.

(2) Coal Cleat Length is the extent or distance along the bedding plane from end to end of cleats depending on the scale or magnitude of the coal “sample” being measured (e.g. from core to outcrop through field size).

(3) Coal Cleat Height is the distance from the bottom to the top of a cleat perpendicular to bedding plane. Close (1993) recognized the relationship between cleat heights and coal composition (e.g. macrolithotypes) [49, 59]. Dawson and Esterle (2010) reclassified coal cleat heights to macrolithotype specific for Australian bituminous coals, which includes vitrain and durain (Figure 2-11). Cleats heights are related to the following macrolithotypes: i. cleat confined within a single vitrain layer; ii. cleat confined within multiple stacked vitrain layers; iii. cleat confined exclusively within durain layers; iv. master cleat, which crosses both vitrain and durain layers; and v. a large master cleat or joint that extends across many macrolithotype layers and partings [46].

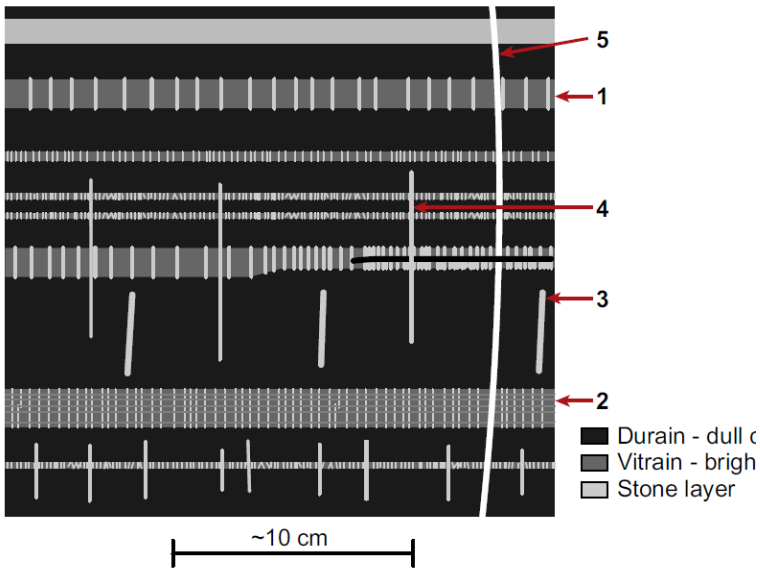

Figure 2-11: Cleat or fracture classification as related to macrolithotypes in Australian Permian coals. Dawson and Esterle (2010). 1) cleat confined within a single vitrain layer; 2) cleat confined within multiple stacked vitrain layers; 3) cleat confined exclusively within durain layers; 4) master cleat, which crosses both vitrain and durain layers; and 5) a large master cleat or joint that extends across many macrolithotype layers and partings [2].

(4) Coal Cleat Spacing is the perpendicular distance between two adjoining cleat surfaces. The factors that control cleat spacing include coal rank, coal composition (e.g. macrolithotypes), bed thickness, and coal cleat height [46, 51, 60]. Cleat spacing decreases from lignite to bituminous coal as a result of moisture and volatile matter loss (Figure 2-12) [51, 54]. On the basis of vitrinite reflectance, Law (1993) reported that coal cleat spacing is greater for lignite (0.25-0.38% *Ro*) than anthracite (2.6% *Ro*) [54]. Laubach and Tremain

(1991) observed in the Fruitland coals (San Juan Basin in the USA) that cleat spacing increases with increasing thickness of medium-bright bituminous coal [51]. Detailed core and mine studies of Permian bituminous coals in Australia by Dawson and Esterle (2010) show a clear relationship between cleat spacing and height where the coal spacing generally increases with the increasing cleat height (Fig. 13) [46].

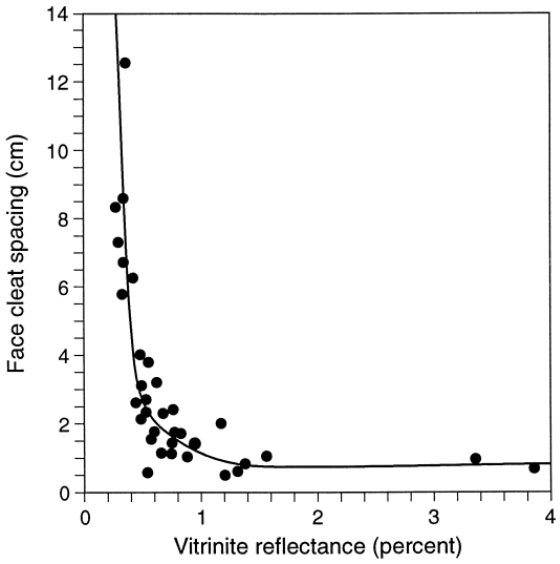

Figure 2-12: Cross-plot of vitrinite reflectance versus cleat spacing for coals ranging from lignite to anthracite. Adapted from Laubach (1998) [50].

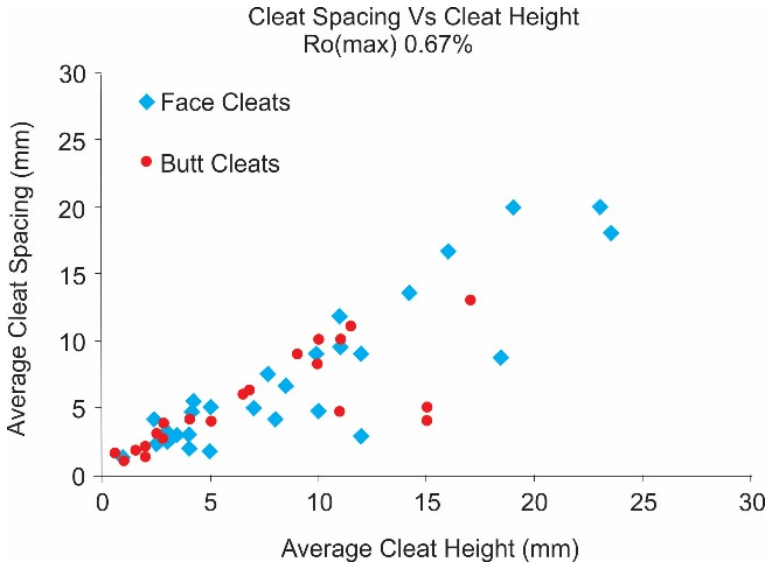

Figure 2-13: Cross plot of face and butt cleat spacing against cleat height for the high volatile bituminous coal core. Adapted from Dawson and Esterle (2010) [46].

(5) Coal cleat connectivity, which drives the bulk permeability of coal, is defined as lateral (one direction horizontal) continuity due to interconnection of the cleat network that includes face and butt cleats as well as other fractures formed by tectonic stress. Laubach et al.

(1998) suggest that the network geometry of and increased connectivity of fractures enhance permeability [50]. McCulloch et al. (1974) observed that permeability in the face cleat direction is 3-10 times greater than in other cleat directions [61].

2.3 Coal Permeability Enhancement

Permeability is the most critical parameter for economic viability of a coal seam gas reservoir. The ease with which a fluid moves through the interconnected pores and fissures of a rock is termed permeability. Whereas porosity informs us about the storage capacity of gas in coal, permeability defines the level of transportability of that gas. Even though a coal may contain gas, the lack of permeability constrains gas recoverability and production. Additionally, permeability can have a significant effect on the drilling, completion, stimulation, and production strategies essential to successful development [62, 63]. The frequency of the natural fractures, their interconnections, direction of butt and face cleats, the degree of fissure aperture openings, burial depths, water saturations, matrix shrinkage upon desorption, and the nature of the in-situ stresses all affect permeability. Additionally, since coal seam gas production involved reduction of formation pressure and desorption of gas, the permeability is complexly transient due to changes in net effective stress and matrix shrinkage [64].

However it is vital to understand that there are two broad types of permeability: matrix and fracture. How these two types of permeability interact with each other determines, to a very large degree, the gas production profile for a well [42]. The natural fractures, or cleats, running through a coal deposit are several orders of magnitude more permeable than the coal matrix (millidarcies or tens of millidarcies versus microdarcies) and control fluid movement through it [65]. However, unlike other naturally fractured reservoirs, where matrix permeability often dominates reservoir performance, especially at long times, coal matrix permeability plays an insignificant role in fluid movement in a coal because of sorption [66]. It is generally thought that matrix permeability is higher in lower rank coals because of the remnant inherent plant porosity, and it decreases with rank [2].

The permeability of many CBM reservoirs is anisotropic, i.e. permeability is greater in one orientation than another, and this is thought to be the influence of differential in situ stress on cleats. The directionality of permeability is important in optimising well placement.

Anisotropy of permeability has mostly been ascribed to the greater continuity of the face cleat, which tends to occur in one direction, over that of the butt cleat, which occurs in a nearly perpendicular direction [64]. The specific nature of the connectivity between the butt and face cleats however may prove to be as important in controlling permeability anisotropy as any other property.

The most predictable relationship with permeability is depth (though from basin to basin the exact permeability corresponding to a depth will be quite different because of differing coal type, tectonics and basin burial histories). Almost without exception, the deeper you go, the less permeable the coal reservoir will be. Note that at any particular depth there can still be considerable variability in permeability. In the example given in Figure 2-14, even at depths of 400 m the permeability varies from tenths to tens of mD [2].

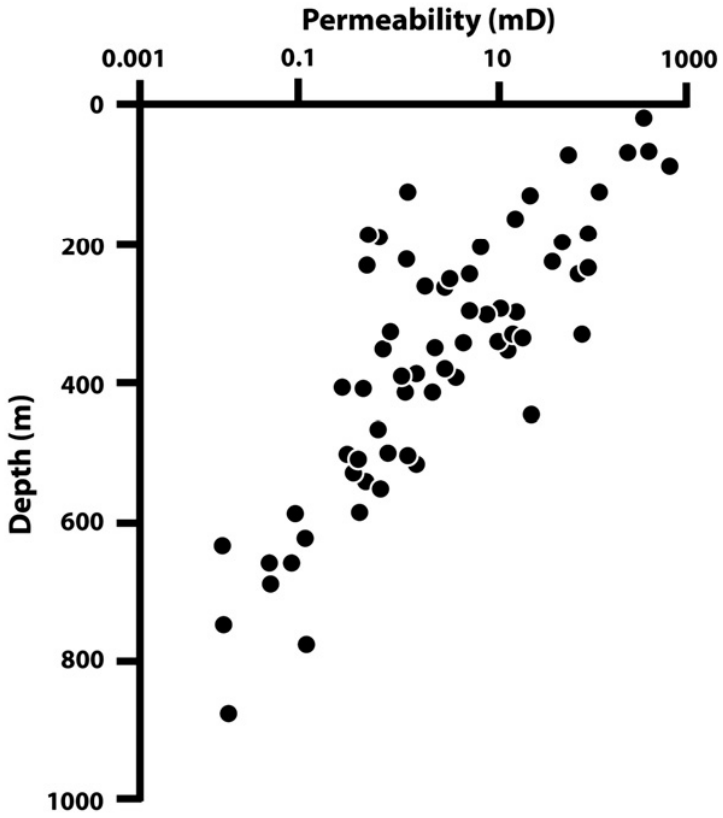

Figure 2-14: In situ coal bed permeability versus depth in a Permian coal basin in Australia. Source modified from Moore (2012) [2].

Due to the important role of permeability and the fact that the permeability is often not high enough for economic CSG production, there is a demand for research into methods that can enhance coal permeability. Normal coal reservoir stimulation is a process of enhancing coalbed gas production by cleaning up the borehole of damage during drilling and then

completion of the well using different physical fracture stimulation treatments. Stimulation can dilate, and extend the width, length, and connectivity of the natural fracture systems of the coal reservoir. Low permeability stimulation treatments primarily consist of hydraulic fracturing and multi-lateral horizontal wells [3].

2.3.1 Hydraulic Fracturing

Hydraulic fracturing is the application of fluids consisting of water or water-based additives, which are pumped into the coal reservoir at pressure that exceeds the tensile strength of the coal such that the fluids open, lengthen, and enlarge fractures and cleats. This may extend tens of meters from the well, improving their connectivity (Figure 2-15 a. b. c). As the fractures open (supported by proppants), it permits the fluids to penetrate further from the injection wellbore that subsequently allows water and gas to flow (e.g. Darcy flow) during de pressuring and gas production.

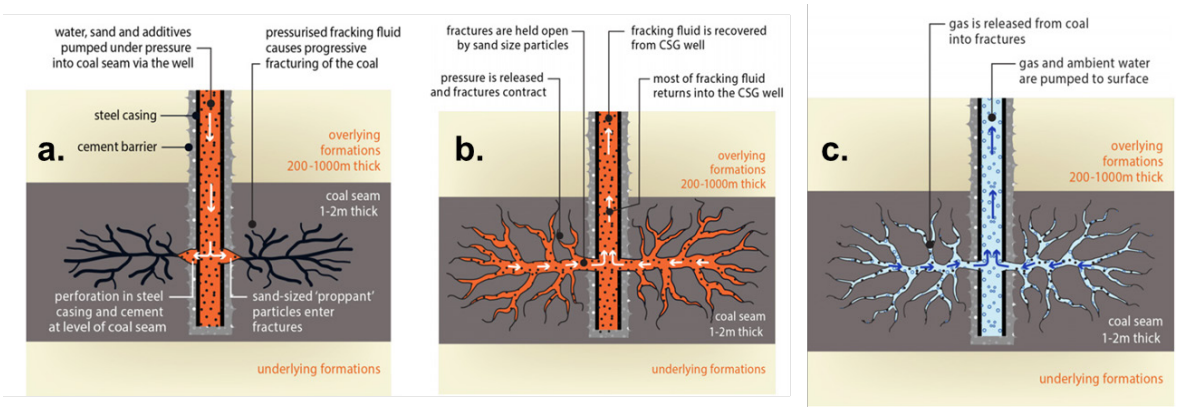

Figure 2-15: Schematic of hydraulic fracturing stimulation: a. flow in of fracking fluids; b. removal of fracturing fluid; c. post recover of fracturing fluid and gas production. Source modified from department of primary industries office of water, NSW [67].

Hydraulic fracturing is widely accepted and applied to improve the gas recovery in coal reservoirs. However, coal reservoirs are often with very low permeability, complicated geological settings and in-situ stress field etc. All of these factors make the effectiveness of hydraulic fracturing a challenging task [67].

In certain circumstances the application of hydraulic fracturing can inadvertently cause damage to the coal reservoir and negate its intended benefit. As R. Puri et al. (1991) reported, permeability damage happened in the whole core samples of coals from San Juan and Black Warrior basins after they were exposed to gelled fracturing fluids and the efforts to restore coal permeability by prolonged flushing with water and HCI/HF solutions failed [7].

They also concluded that the permeability damage is usually caused by cleat plugging, particularly by gelled fluids and fluid sorption, which can lead to the coal matrix swelling, consequently the reduction of the coal permeability [7]. In addition, hydraulically stimulated vertical holes have the disadvantage of requiring large numbers of surface sites with associated increase number of production and maintenance operations [3].

2.3.2 Horizontal Wells

A long horizontal borehole intersects a much greater volume of the coalbed than a vertical borehole and the borehole trajectory can be controlled to take advantage of coalbed directional cleat permeability anisotropy. In addition, a large area 2.6 km^2 (640 acres), can be drained from a single surface site with multiple lateral wells in different directions. Compared to vertical wells, 16 vertical wells drilled on 0.16 km^2 (40 acres) spacing greatly reducing the environmental impact of the methane drainage project and results in drilling, infrastructure, and maintenance cost savings [68].

Horizontal wellbores are considered to be very effective in reservoirs that are relatively thick, naturally fractured, and anisotropic with regard to permeability. Horizontal well drilling and completion is an alternative technique to overcome low production as well as reservoir heterogeneities in coalbed reservoirs [3].

2.3.3 Acid Stimulation

Acid stimulation is traditionally used as a permeability enhancement method in conventional reservoirs, particularly when formation damage happens [69] or for carbonate reservoirs or carbonate cemented reservoirs. However, the usage of acid stimulation in coal is relatively rare [10, 70].

For low permeability coal seams with highly mineralised fractures, dissolution of mineral occlusions will likely increase fluid flow capacities [9-11]. Vasyuchkov (1985) reported aqueous HCl (2, 4 and 6%) solutions could enhance the coal permeability dramatically from less than 0.1 mD to over 15.1 mD [12]. Turner et al (2016) conducted the core flooding tests with coal samples containing various cleat and mineralogical properties. The permeability enhancement results are mineral type dependent that the increases in permeability can be achieved where cleats are rich in carbonates, however, the presence of clays may place limitations on the extent of enhancement.

Balucan et al. (2016) investigated the effect of mineral alteration by hydrochloric and hydrofluoric acid (HCl-HF) on fracture compressibility and coal permeability. Coal core immersion in 15% HF- 4% KCl solution has enhanced coal permeability and reduced fracture compressibility. The overall findings show that mineral alteration by HF yielded relatively large, crystalline minerals that appeared to provide structural support to fractures, resulting in enhanced fluid flow and improved resistance to compression. Later Balucan et al. (2018) investigated the acid-induced physical and chemical changes in core samples to gain improved understanding of permeability enhancement in the vertical flow direction [13]. There was clear evidence for cleat opening via mineral dissolution as well as mineral mobilization-accumulation. Based on the X-ray microcomputed tomography (μCT) image analyses, they conducted flow simulation and reported that acidizing could enhance permeability not only in the vertical direction but also in the lateral or horizontal direction [13]. Similarly, Ramandi et al (2018) applied the μCT and numerical simulation to investigate the effect of dissolution of syngenetic and epigenetic minerals on coal permeability and they reported that coal permeability increase depends significantly on epigenetic mineral dissolution, and secondarily on syngenetic mineral dissolution [14].

Although the above studies have examined the effect of acidization on coal permeability experimentally and numerically, problems still existed. For example, few of their results is about the horizontal permeability which is parallel to the face cleats and more realistic than the reported vertical permeability. Additionally, in the core flooding tests conducted by Turner et al. (2016), the HCl was injected at the same direction with brine [11], which, to mimic how stimulation would be conducted downhole, should be adopt forward flow to characterise initial permeability, reverse flow with acid to simulate the downhole treatment, and then forward flow again to characterise the final permeability.

2.4 Oxidant candidates and their reaction with organic matters

Oxidation of coal has been widely studied in coal molecular structure investigation and to obtain high-value organic chemicals such as low-molecular weight fatty acids and some long-chain aliphatic hydrocarbons [71-73]. It has also been reported in other coal related industries, but with less attention, such as coal coking [74], caking [75], desulfurization before utilization in power plants [76, 77], coal self-heating and subsequent spontaneous combustion in coal mines and stock piles [78-80] and even in terms of the biogenetic

methane production [81]. A comprehensive overview of coal oxidation methods under mild conditions has been provided by Yu et al. (2014), consisting primarily of hydrogen peroxide (H_2O_2), sodium hypochlorite (NaClO) and secondarily of potassium permanganate ($KMnO_4$), oxidizing acid, oxygen, and ozone [82]. Although coal oxidation has been investigated as described above, little research has focused on the potential for permeability enhancement by oxidation.

2.4.1 Hydrogen peroxide (H_2O_2)

Hydrogen peroxide is one of the most commonly used oxidants across a wide range of industries. This is because in the course of reaction, H_2O_2 will generate ·OH-radical which is a powerful oxidant and the reaction rate of a compound in ·OH-radical oxidation is usually several orders of magnitude higher than the reaction rate with molecular ozone under the same conditions [83]. Application of hydrogen peroxide has some advantages. ·OH-radicals are non-selective oxidants which offer a large number of possible reactions [83]. There is no deposition of unwanted chemical substances while oxidizing with hydrogen peroxide [17].

The following summaries in the literature prove the wide use of hydrogen peroxide. Jones et al. (2013) employed 5% H_2O_2 to oxidise coal as a proxy for chemical oxidation by O_2 to investigate the effect of coal partial oxidation on biogenic methane potential [84]. A. Matilainen et al. (2010) employed hydrogen peroxide to remove natural organic matter from drinking water and also introduced the basic oxidation mechanism by H_2O_2 [83]. Miura et al. (1996) postulated a new method to utilize the low-rank coal by oxidizing the coal with H_2O_2 to produce small molecule and water-soluble organics. The experimental results showed that a large amount of oxygen and hydrogen was introduced into the coal and aliphatic C-H increased significantly, which showed that some of the aromatic rings of the coal are ruptured by the H_2O_2 oxidation. They also introduced the fatty acid generation procedure, that firstly breaks the weak -C-O- linkages, producing a large amount of water-soluble large molecular compounds and CO_2, and secondly, the large molecules gradually decompose with the progress of oxidation to produce small molecule fatty acids [73]. The bench scale experiment, in which H_2O_2 was used as the oxidant for remediation of polycyclic aromatic hydrocarbon-contaminated soil, suggested that the removal efficiency increases with the oxidant dose if the dosage is low, while if the oxidant dosage increase above a certain threshold level, the removal efficiency may decrease. This effect is thought to be due to the very strong and rapid reactions caused by the high reactant dosages, which may subsequently prevent good contact between oxidant and pollutants (too strong and rapid

reactions) [85]. Mae et al. (1997) proposed that the pre-treatment with H_2O_2 could partly break some covalent bonds and simultaneously introduced oxygen functional groups such as -COOH and -OH into coals, and hence facilitated coal extraction [86]. Liu et al. (2013) also proved this by laboratory experiments where they found that NaClO could dissolve more coal samples pre-treated with H_2O_2 than the raw coals [20].

Once free radical reaction has been initiated by hydrogen peroxide, a series of simple reactions will ensure. The reactions of ·OH-radicals with coal organic matter proceeds by three different ways: (i) by the addition of ·OH-radicals to double bonds, (ii) by H-atom abstraction, which yields carbon centred radicals and (iii) by reaction mechanism where ·OH-radical gets an electron from an organic substituent. The carbon centred radicals then react very rapidly with oxygen to form organic peroxyl radicals. The reactions of peroxyl radicals among themselves can lead to production of ketones or aldehydes and/or carbon dioxide [87].

2.4.2 Sodium hypochlorite (NaClO)

NaClO has been used for fundamental research about coal structure [15, 16] and obtaining organic substances from coal [21]. Because of its availability, NaClO is attractive as an industrial oxidant [17]. Coal oxidation with NaClO was used in Chakrabartty and co-workers' research to investigate coal's molecular structure [15] and then similar research was conducted by Mayo et al. [16, 88, 89]. They reported that during NaClO oxidation, the condensed aromatic rings in the coal structure could be attacked to generate primarily, a base-soluble "black acid", and secondarily, water-soluble light-colour acids and carbon dioxide [88]. The presence of oxidation products indicates the potency of NaClO to degrade coal. Recently, Wei and his team published a series of research articles about coal oxidation by NaClO to acquire an industrially useful organic substance and to investigate the coal oxidation mechanisms [17, 20, 21, 72, 90, 91]. Employing Gas Chromatography-Mass Spectrometer (GC-MS), they found that most of the coal, regardless of coal rank, could be oxidised by NaClO and the main oxidative products were short-chain alkanoic acids, benzene polycarboxylic acids and some carbon dioxide [72].

NaClO has higher reactivity toward coal oxidative degradation than H_2O_2, and the inexpensive, environmentally friendly, and easily available features make it an attractive industrial oxidant [17, 20]. NaClO has been used for fundamental research about coal

structure [15, 16] and obtaining organic substances from coal [21]. Coal oxidation with NaClO was firstly used in Chakrabartty and co-workers' research to investigate coal's molecular structure [15] and they concluded that NaClO tended to attack aliphatic carbons because they found aromatic hydrocarbons were not oxidized at 60-70 °C in aqueous NaClO. However, similar research conducted by Mayo et al. [16, 88, 89] showed that during NaClO oxidation, the condensed aromatic rings could also be attacked, especially in the existence of hydroxylated aromatic rings [16], to generate primarily, a base-soluble "black acid", and secondarily, water-soluble light-colour acids and carbon dioxide [88]. The products in Mayo's work had a higher ratio of aliphatic/aromatic content than the original coal. The presence of oxidation products indicates the potency of NaClO to degrade coal.
Recently, Wei and his team published a series of research articles about NaClO oxidation of various coal types to acquire an industrially useful organic substance and to investigate the coal oxidation mechanisms [17, 20, 21, 72, 90, 91]. Employing GC-MS, they found that most of the coal, regardless of coal rank, could be oxidised by NaClO and the main oxidative products were short-chain alkanoic acids, benzene polycarboxylic acids and some carbon dioxide [72].

Firstly Liu et al. (2013 a) used NaClO to oxidise a Chinese lignite in a series procedures. They found that less than 14.7% of the original mass was left and the products predominantly consist of bezene carboxylic acid (especially benzenetricarboxylic and benzenetetracarboxylic acids), chloro-substituted short-chain alkanoic acids and alkanedioic acids [17]. Based on the same sample, Liu et al (2013 b) pre-treated the sample using H_2O_2 and then oxidised it with NaClO and finally found that more coal sample was converted to water-soluble portions. They also proposed the benefit of the pre-treatment as weak bridged bonds like C-O-C connecting condensed aromatic rings were broken by H_2O_2 and led to the formation of aromatic or alcoholic C-OH. Both covalent bond cleavage and organic functional groups introduction resulted in higher reactivity and hydrophilicity of the sample. The increase in hydrophilicity improved interaction between coal particles and NaClO aqueous solution, and thereby promoted coal oxidation [20].

Yao et al. (2010) used NaClO to oxidise a low sub-bituminous coal and found that the short chain alkanoic acid, probably derived from phenoilic moiety in coal and benzene polycarboxylic acid were the most abundant components in the NaClO product. However, they did not show the exact portion ratio in the whole products [72]. Later, Zhao et al. (2015) investigated the effects of oxidation conditions on a bituminous coal sample, such as

temperature, reaction time, the ratio of coal sample to NaClO volume and pH, on the product distributions and compositions. They reported that the temperature slightly influenced the product and 5 hrs was long enough for convert most of the coal samples into water soluble products. When the ratio of coal sample to NaClO volume was below 1 g/100 mL, the sample residue mass was similar. Of particular interest is the influence of pH in the range from 8.5 to 12, where the coal residue mass decreased with decreasing pH. This agreed with Mayo's study which also reported that pH 13 might be the optimum condition for NaClO oxidation [88]. Finally, they optimised the most favourable coal oxidation in aqueous NaClO condition as: reaction temperature of 30 °C; reaction time of 9 h; the ratio of coal to aqueous NaClO of 1 g/100 mL and high pH (12). In the same study, they also reported the phenomenon of reaction mixture colour change from black brown to yellow brown during oxidation as the generation of humic acid [92].

In terms of the NaClO oxidation of anthracite coal, Wang et al. (2014) compared anthracite coal oxidation results in two different patterns: one run oxidation and sequential oxidation (6 times). They found that significantly more organic matter in anthracite coal was oxidized into a water-soluble portion by sequential oxidation (62.15%) than by one-run oxidation (42.49%) for the same period. The difference was explained as the water-soluble portion reacted much easier with oxidant than the coal residue, so in one-run oxidation the water-soluble portion consumed more oxidant and prohibited the coal residue oxidation. In the sequential oxidation, it is of particular interest that the water-soluble portion decreased in the first three runs but suddenly increased in the fourth run and then decreased to the end. They proposed that the coal oxidation happened from the external surface to internal surface and in the fourth oxidation run, the oxidant reached the internal surface. They concluded of the two parts that the external part was cata-condensed aromatics while the internal part was rich in peri-condensed aromatics [21]. However, the small size and the porous property of the coal sample (74 μm) raised the question if the interface really existed.

The oxidation reaction with NaClO is complex, and several reactions may occur simultaneously such as addition, substitution, free radical formation, and oxidation. Despite this, reaction mechanisms have been postulated by analysing the reaction products, especially the water-soluble portion. NaClO might oxidize the side chain on the benzene ring and poly-nuclear aromatics in the presence of oxygen functional groups [15, 72, 82, 89, 90]. A simplified mechanism schematic is shown in Figure 2-16.

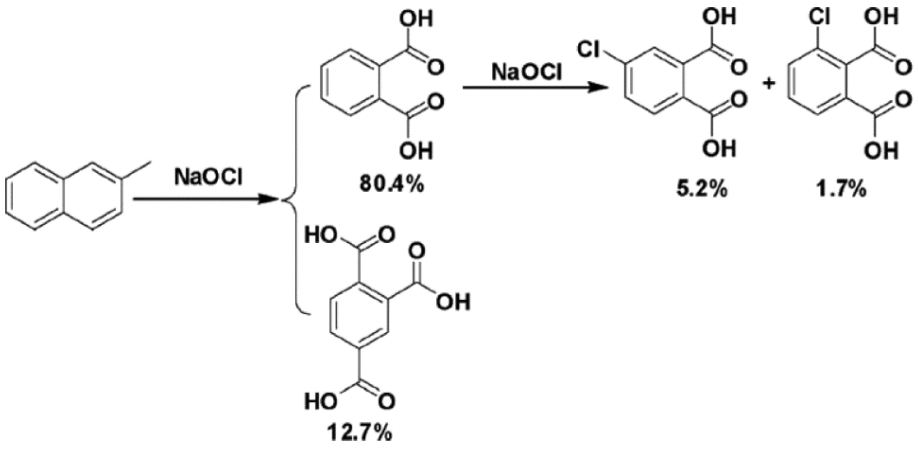

Figure 2-16: Simplified mechanism schematic of NaClO reaction with coal [82].

2.4.3 Potassium permanganate ($KMnO_4$)

Despite the relatively low standard oxidation potential (1.7V), permanganate salts are considered strong oxidizing agents, able to break organic molecules containing carbon–carbon double bonds, aldehyde groups, or hydroxyl groups [93]. Potassium permanganate ($KMnO_4$) is a common oxidant for remediation of contaminated soil, and has a high redox potential [94-97]. For example, Wang et al. (2015) conducted a study to assess the feasibility of using $KMnO_4$ as an oxidant to reduce the polycyclic aromatic hydrocarbon content in coal tar pitch and it had been observed to reduce of major polycyclic aromatic hydrocarbon after oxidation [94]. Alyol et al. (2009) also investigated the performance of oxidation of residual trichloroethylene trapped either in karst soil or at the regolith contact with carbonate bedrock by $KMnO_4$ [95].

However, $KMnO_4$ oxidation used in coal is rare. It was only reported to be used in etching coal polished surfaces to observe the original constituents in coal [98, 99].

The interaction between $KMnO_4$ and organic matter is mainly an electrophilic substitution reaction. Specifically, the π-electron cloud of the aromatic rings are attacked by the $OMnO_3^-$ which generates a new π-complex, and then there is a donation of two electrons from the π-complex to form a σ-complex, the carbon atom linked to $OMnO_3^-$ changes from sp^2 hybrid orbital to a sp^3 hybrid orbital, and the change can lead to the closed conjugate system being destroyed, and no more p-orbital [100, 101]. The σ-complex, as an instable system, would lose a proton from the carbon atom of the sp^3 hybrid orbital to reform a closed system of

conjugate, which reduces the system energy and generates a relatively stable substituted oxide [100, 101].

Of the few papers that report coal oxidation by $KMnO_4$ solutions, Norton et al. showed information about the coal desulfurization with permanganate [102] and the limitations of this method, such as the necessity of multiple reactions and the deposition of manganese dioxide from the decomposition of $KMnO_4$ [19]. Moore et al. etched the coal surface using $KMnO_4$ with sulphuric acid to observe the fossil plant particles [98]. With $KMnO_4$ commonly used in soil and water remediation to remove excessive organic matter [103, 104], it shows promise for our application.

2.4.4 Potassium persulfate ($K_2S_2O_8$)

Although no research has been reported on oxidising coal with $K_2S_2O_8$, its high oxidation potential (E° =2.1V) [71] and its wide exploitation in industrial processes, such as oxidation of contaminated soil and groundwater, metal surface oxidation and organic chemical manufacturing [105], make it an interesting potential oxidant candidate in this study. Recent work has reviewed procedures to activate persulfate such as the use of heat, ultraviolet light, high pH, hydrogen peroxide and transition metals [71, 106, 107].

2.4.5 Nitric Acid (HNO_3)

Nitric Acid is widely used in the desulfurization of coal and the corresponding process parameters such as temperature and acid concentration have been extensively studied [108-110]. The major products resulting from nitric acid oxidation of coal are benzene carboxylic acids, short chain aliphatic acids and humic acid material [111]. Pietrzak (2002) ran coal oxidation experiments with different oxidants and found that the 5% HNO_3 acid is so effective that a significant part of the organic components of coal were converted into soluble products accompanied by an increase in oxygen and nitrogen content and a decrease in carbon and hydrogen content. Aromatic structures undergo oxidation and are converted into low molecular compounds soluble in acids [111]. Alvarez et al. (2003) examined the behaviour of a Spanish lignite during its oxidative treatment with nitric acid (20% or 30% wt%) and several phenomena were detected including the coal mass loss, a relative increase of aliphatic hydrogen, an increase of total hydrogen carbon and a significant increase in carbonyl groups that indicate nitric acid attack [109].

In terms of the nitric acid oxidation, the system temperature, and solvent concentration are the most important parameters. Alam et al. (2009) found that temperature has a significant influence on the reaction rate where oxidation is more violent when the temperature reached 90 °C, however, at a temperature above 90 °C, the nitric acid will be rapidly destroyed and converted to NO_2 [110]. This is also supported by the research conducted by Rodríguez et al. (1996) [108]. They employed nitric acid (5% and 30% wt%) to desulfurize a Spanish coal of intermediate rank and during the treatment, they also found breakage occurred leading to size degradation of the coal particles [108]. Rodríguez et al. (1997) studied the desulfurization of Mequinenza coal with nitric acid leaching and the decrease of carbon content as well as an increase of oxygen content in the organic matter was detected. However, this phenomenon only happened above a critical temperature (50 °C in Rodriguez's work). The colour of the samples changed from black in the beginning to a brown colour after the treatment [112]. By contrast, in the research conducted by Alam et al. (2009), the acid concentration was regarded as the most effective parameter on the desulfurization process of Mezino coal [110].

Although coal oxidation has been widely studied previously as described above, little research has focused on the application of permeability enhancement by this method and a large number of technical and practical application questions still need to be answered. For example, the oxidation results might vary between different coal types including different rank coals and different coal maceral compositions. Besides, the pressure might play a significant role in the coal oxidation, because the coal is exposed to high pressure and temperature *in-situ*. The diversity of chemical composition, physical properties and porous structure of coal adds to the complexity of achieving effective and reliable coal oxidation methodology [79]. Therefore, the study of coal oxidation to enhance coal seam permeability will be important, not only as an alternative to increase the coal seam gas production, but also to provide new knowledge which could benefit a wide range of areas such as coal processing.

2.5 Conclusion of the literature review

Permeability of coal seams is a key controlling factor for gas migration in coal reservoirs and is often a critical technical barrier preventing economically viable gas production. The literature review has highlighted the importance of increasing coal seam permeability and meanwhile, demonstrate the fact that conventional stimulation techniques such as hydraulic

fracturing and multiple horizontal wells have been problematic in some basins. Oxidant stimulation to increase coal seam permeability, as an alternative, is of great importance. However, few research has been conducted in this area.

Coal oxidation has been reported widely in the areas such as coal molecular structure investigation and obtaining high-value organic chemicals [71-73], coal desulfurization before utilization in power plants [76, 77], coal self-heating and subsequent spontaneous combustion in coal mines and stock piles [78-80] and even in terms of the biogenetic methane production [81]. In these studies, different oxidants have been used mainly including NaClO, $KMnO_4$ and H_2O_2. However, few research has reported a thorough comparison of the oxidative efficiency between these oxidative candidates, especially on specific coal types. No research so far has studied the oxidative effect on coal structures like coal pores and cleat systems, which are critical properties to coal permeability. Therefore, a screening method of the most promising oxidant candidate is reported in chapter 3 and chapter 4 describes the oxidative effect on coal structural properties.

The studies that do exist on coal oxidation have only focused on examining the dissolved organic substances in the solution. This limits the application of knowledge gained for our purpose. The limitation is further amplified given the high heterogeneity of coals. In the current study, the molecular structure identification of the raw coals and their oxidative residues are reported in chapter 5.

The lack of research in coal oxidation, particular in the permeability change after oxidation raises the question whether coal oxidation could benefit the coal permeability or ruin the coal integrity thereby ruining the permeability. To answer it, in chapter 6, we use the core flooding test combining with CT scanning to examine the permeability change after oxidation as well as the associated coal structure change to explain the effect on permeability.

Chapter 3. Swelling and solubilisation behaviour of unconfined coal particles in oxidants

3.1 Introduction

Oxidants could have potential to increase the coal cleat aperture by etching the coal cleat surface or dissolving a portion of the coal matrix. In addition, weakening the coal matrix by oxidant reactions may also prove applicable as a pre-hydraulic fracturing conditioning process. This chapter specifically aims to identify promising oxidants, those that can etch/dissolve the surface of a coal cleat whilst minimising matrix swelling. This is a critical step prior to the lengthy and relatively complex core flooding studies, such that insights gained from this work on coal behaviour in oxidising solutions will complement and improve the understanding of chemical and physical mechanisms that occur when coal comes into contact with oxidants.

Coal oxidation has been studied in coal structure investigations [15-17], desulfurization [18, 19] as well as organic chemical extraction from coal [20, 21]. Commonly used coal oxidation agents include sodium hypochlorite (NaClO), potassium permanganate ($KMnO_4$) and hydrogen peroxide (H_2O_2), potassium persulfate ($K_2S_2O_8$).

All the oxidants show various degrees of effectiveness in oxidising coal, as described in chapter 2. However, very few investigations exist in the application of these oxidants for enhancing coal seam permeability.

Coal matrix swelling in solvents like pyridine has been widely studied [113-116]. A large body of research with regard to coal particle size change has been conducted using multiple methods [114, 117], among which, camera observation is a simple and sufficient method as described in Van Niekerk's work [118, 119]. Other researchers, such as Murata [116], Gao et al.[114, 117, 120] also utilised 2 or 3 cameras to study the anisotropic swelling of single coal particles with a size between 200-250 μm in solvents including pyridine and N-

methylpyrrolidone (NMP). Therefore, this study employs the camera based swelling test in conjunction with leaching tests to screen potential oxidants that solubilise coal.

The net effectiveness of oxidation on coal seam gas stimulation may be contingent on either the coal rank or maceral composition or both. Low rank coals have previously been proposed to be easily oxidized by NaClO. For example, Liu et al. (2013) reported that low rank lignite (C%=70.84 wt.%, d.a.f.) was easily oxidized in a 6% NaClO solution with more than 85.3 wt.% water soluble organic matter obtained after oxidation [17]. In contrast, Wang et al. (2014) obtained with the same method only 42 wt.% water soluble organic substances after oxidation of anthracite (C%=88.40 wt.%, d.a.f) [21]. Furthermore, the oxidative products in each experiment were different with mostly alkanoic acid and alkanedioic acids produced in lignite oxidation and benzene carboxylic acids from anthracite oxidation [17, 20, 21]. The difference in oxidative products from different rank coals is due to different coal structures with lignite being more aliphatic and more oxygen-containing structures than anthracite [31, 121-124]. Additionally, although the reactivity of H_2O_2 might be relatively low toward coal degradation, it is also reported seems to be suitable for low-rank coals to obtain value-added chemicals [20].

Therefore, two coals, with different rank, from CSG production basins (Bowen and Surat basins) in Queensland, Australia, were used to investigate the different coal behaviours with various ranks. With knowledge of coal's behaviour in oxidising solutions, it is aimed to develop an appropriate technique to increase the coal permeability. Additionally, the oxidants with negligible environmental impact, would be considered further.

3.2 Experimental

3.2.1 Coal sample

Bituminous (coal B) and subbituminous (coal S) coal drill core samples were collected from the Bandanna Formation in Bowen Basin and the Walloon Subgroup from Surat Basin, respectively. The chemical and petrographic analyses of each sample are summarised in Table 3-1 and Table 3-2. The ultimate and proximate analyses of the coal samples were carried out at the ALS Coal Division – Richlands, Australia. Elemental oxygen contents were determined by difference (Table 3-1).

Random vitrinite reflectance (R_O) and the maceral composition were determined at the School of Earth and Environmental Sciences laboratory, The University of Queensland. Sample blocks were ground, polished and examined under a Leica DM6000 microscope® fitted with an internal 10x lens and a 50x reflected light oil immersion objective, giving a total of 500x magnification. For imaging a high resolution black and white camera and a colour camera are attached to the microscope. The former is also used for reflectance analysis according to ISO 7404-5 [125]. Hard- and software for this microscope system were made by Hilgers Technisches Buero (Diskus Fossil). The group macerals were quantified by a 500 point-count technique following the procedures described in the standard ISO 7404-3 [126].

Table 3-1: Ultimate and proximate analysis of coal drill core samples

Coal Sample	Ultimate analysis (wt.%, d.a.f)					Proximate analysis (wt.%, d.b)			(wt.%, ar)
	C	H	S	N	O (diff.)	Ash	VM	FC (diff)	MC
Coal B	85.54	5.06	0.33	1.97	7.10	6.6	28.7	62.2	2.5
Coal S	77.88	6.15	0.57	1.31	14.08	12.3	43.1	39.5	5.1

C – carbon; H – Hydrogen; S – Sulphur; N – Nitrogen; O – Oxygen; VM – Volatile Matter, FC – Fixed carbon; MC – Moisture content; d.a.f: dry ash free base; d.b: dry base; ar: as received

Table 3-2: Petrographic analysis based on maceral groups of coal drill core samples

Coal sample	Petrographic analysis (vol.%)				Vitrinite reflectance
	Vitrinite	Inertinite	Liptinite	Mineral Matter	*Ro, %*
coal B	62.8	32.4	2.2	2.6	0.84
coal S	56.4	3.6	29.0	11.0	0.47

3.2.2 Swelling test

A time-lapse photographic method was developed to study the swelling behaviour of coal particles in various solutions and candidate oxidant stimulants. In the current method one camera was used with multiple coal particles (between 20 and 40 mg, 3–4 mm). This is to increase the representativeness of the test, because although the coal particles are from one single coal core sample, they might have different maceral compositions and internal structures. The advantage of this method is that the extent and rate of swelling or shrinkage

of larger individual coal particles can be studied. Each test was repeated to check the confidence of the results.

Because air and moisture within the coal pores could limit solvent diffusion into the coal structure, the particles were dried for 2 hours at 110 °C. The dried particles were subsequently saturated in 4% KCl solvent for 10 hours in a vacuum oven at room temperature. 4% KCl mimics production water and is well-known to inhibit clay swelling [11]. Therefore, we had 4% KCl in all solutions with one sample having 4% KCl and no oxidant, i.e. blank test.

Individual coal particles were placed in quartz glass tubes (length = 130 mm, inner ø = 5 mm, outer ø = 6 mm, internal volume = ~5 ml) and mounted against a well-lit white background. A typical experiment involves seven particles. The solution volume is > 10 times the particle volume [127]. Once the particles are immersed, the tubes were sealed with a plastic stopper. All the tests were conducted at room temperature (22±1 °C) and under ambient pressure. Note that several research experiments have demonstrated that the swelling behaviour of coal particles is independent with temperature up to 60 °C [128-130].

A modification of the standard test was applied for experiments with $KMnO_4$ as the native colour of the solution is deep purple and the presence of MnO_2 precipitate (black) renders the coal-solvent boundary delineation impossible. In order to circumvent this limitation, the swelling test with $KMnO_4$ was performed in the following manner: Firstly, 4% KCl was added to the tubes as the background solvent and 30 images were taken as the baseline. This was followed by adding permanganate in the tubes except the blank one. At the end of the test, most of the permanganate was siphoned out and 1% HCl was added to dissolve the MnO_2 precipitate and react with the residual $KMnO_4$, yielding a clear, transparent solution.

3.2.3 Image analysis

Digital images were captured at 5 min intervals over different periods with different solvents. Image analysis was conducted using ImageJ (2015) software. Firstly, the digitally-acquired images were loaded onto ImageJ to form an image stack. The image stack could be saved as a video to examine the reaction phenomenon such as colour change, gas generation and particle movement. Where particle movement occurred, the particle was removed from the analysis.

The images in the stack were then adjusted by increasing the brightness and contrast values to delineate the phase boundary between the solid (coal particle, black) and liquid (solvent, hues of white). The well-contrasted images where then binarised (all colour hues assigned to be either 0, black, or 255, white) to allow for the subsequent quantification of particle projection area. Following stack binarisation, the projection area (pixels) of the coal particle in each image was ascertained using the in-built plugin.

As each individual image is associated to time, a swelling ratio (S_R) can be determined by dividing the projection area of the treated coal particle at any particular time step by the projection area at the start. The blank test also provides an excellent reference whereby any external effects (i.e., lighting fluctuation, camera flicker, vibration) can be detected and used to form good judgement of reaction progress. Finally, a graph of S_R versus time was created. A value of S_R = 1 corresponds to no particle size change with S_R <1 indicating particle shrinkage, whilst S_R>1 indicates particle swelling.

Based on the swelling ratio, the swelling rate (S_r) could be calculated using Equation 3-1.

Equation 3-1

$$S_r = \frac{S_{R(t+\Delta t)} - S_{Rt}}{\Delta t}$$

Where, S_r is swelling rate, $S_{R(t+\Delta t)}$ is swelling ratio at time t+Δt, Δt is the unit time, and S_{Rt} is the swelling ratio at time t.

3.2.4 Leaching test

The leaching test was performed to investigate the mass change and total organic carbon (TOC) after coal oxidation. Leaching tests involved reacting 1g of crushed coal (75-212 μm) in 100 ml of solutions (blank test/oxidants) for 24 hours at ambient temperature and pressure (1 atm) with continuous stirring at 300 rpm. Coal samples were dried at 110 °C to allow mass comparison before and after oxidation. Solutions were prepared by diluting concentrated oxidants in distilled water, leaving one solution with distilled water alone to achieve a blank test. Concentrations of candidate oxidant stimulants used in the leaching tests are as follows: NaClO (0.1%, 1% and 10 %), $KMnO_4$ (0.1%, 1%, 3%, 5%), H_2O_2 (1%, 3%, 10%, 30%) and $K_2S_2O_8$ (1% and 3%).

In addition, a series of leaching tests with different pH conditions were also conducted for coal B. The different pH conditions were provided by initially diluting the oxidants to its

designed concentrations with 1% H_2SO_4 (acid condition) or 2% KOH (base condition). Noteworthy is that the mixture pH values were all measured initially and not kept stable during reaction.

At the conclusion of the tests, the coal particles and leachate solution were separated via vacuum filtration using filter paper with a pore size of 5 µm in order to retain the coal particles. After filtration, the coal samples were dried at 110 °C for 24 h and weighed, while the filtrate was subjected to total TOC analysis. The TOC analysis was conducted using an Elementar Vario TOC Cube instrument in the School of Earth and Environmental Sciences (SEES), The University of Queensland.

3.3 Results

Before testing the coal behaviour in candidate oxidants, 4% KCl and pyridine were firstly used to determine the sensitivity of the swelling test set-up and validate the results by comparing with the reported data. Then three solvents used in the CSG industry were used to approve the reliability of the swelling test results and provide some experimental data that could be useful to industry. Finally, the coal behaviour in candidate oxidants were examined.

3.3.1 Method development

3.3.1.1 Baselining

An initial test was conducted on repeatability for 4% KCl. The S_R for 4 coal particles are shown in Figure 3-1. The S_R shows that the coal particle size did not appreciably change in 4% KCl. A maximum variation of +/- 0.002 or 0.2% was obtained from this test, indicating a sensitivity of 0.2%. Afterwards, a blank test with 4% KCl in each experiment was implemented to provide a baseline from which solvent-induced changes in coal can be referenced from.

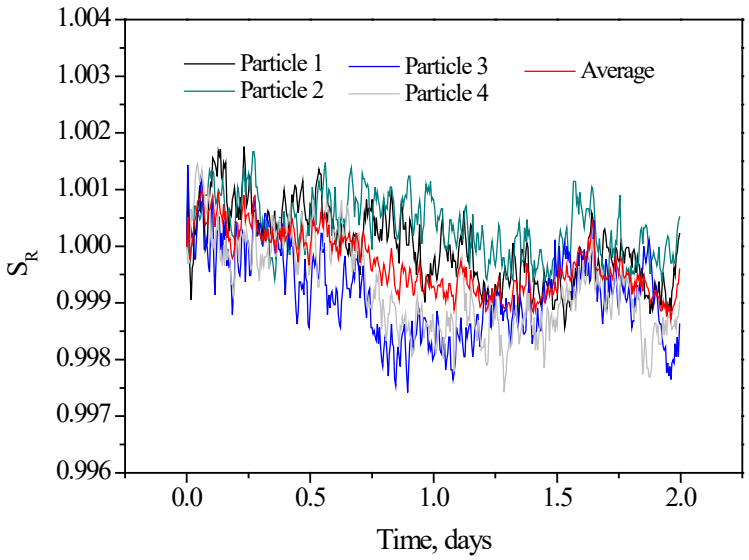

Figure 3-1: Baseline swelling ratio, S_R, of unconstrained coal particles in 4% KCl.

3.3.1.2 Method validation

Pyridine, known to cause significant swelling of coal, was used for method validation by comparison to reported swelling indices obtained from various techniques. During the tests, the solvent discoloration prevented accurate discrimination of the coal particle from the bulk solution. This effect has also been observed in Van Niekerk's work [119]. In this study, it was resolved by increasing the solution/coal volume ratio, from 10/1 to 15/1.

The method validation run with pyridine and coal B is shown in Figure 3-2. The S_R data (Figure 3-2a) show that coal particles in pyridine appeared to swell, with the S_R between 1.6 (+60%) to 2.4 (+140%) and with an average value of 1.98 (+98%). This is in good agreement with the research conducted by Murata using a photographic method (S_R = 1.7 to 2.3) [116], the study by Otake who used a volumetric method (S_R = 1.9 to 2.4) [128] and Otake's research (S_R = 1.58 to 2.42) [130].

The corresponding S_r of coal B in pyridine is shown in Figure 3-2b, in which the dash line indicates the moving average of S_r. S_r of coal B particle increased firstly and reached a peak of 14% change per 6 hrs at approximately t=16 hrs followed by a sharp drop until t=24 hrs. Afterwards, S_r generally dropped to almost zero at around 36 hrs, which indicates the point that the coal stopped swelling.

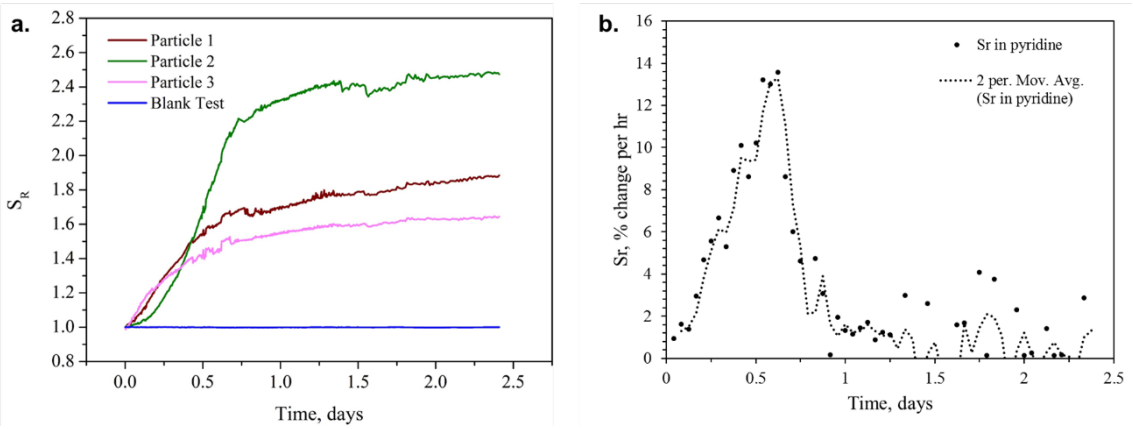

Figure 3-2: Swelling ratio, S_R (a) and swelling rate, S_r (b) of unconstrained coal particles in pyridine.

The relatively large S_R ranges for pyridine could be attributable to the tendency for anisotropic swelling that Cody [113] and Gao [120] observed, and the different lithotypes of coal particles, even though they were all from the same coal core. Therefore, in this study, the average S_R of all the particles was used as a representative swelling value. Although not shown in Figure 3-2, some particles were observed to swell and break into smaller particles.

The above test results indicate that the swelling test rig performed as designed with results validated against published literature and that it has the capacity to detect the coal behaviour in solutions that could react with the coal significantly like pyridine as well as in those that do not react with the coal, like 4% KCl. Therefore, we used this method as a rapid screening approach to look for the promising chemicals that may have the potential to enhance permeability.

3.3.2 Coal B swelling behaviours in solvents

This section explores coal B particle behaviour in solvents namely ammonia, ethanol and tetramethylammonium chloride. 1% ammonia is used in the CSG industry to dissolve hydraulic fracturing gels [131], while ethanol is used as a surfactant to increase fluid recovery from fractures [132]. Additionally, tetramethylammonium chloride is used as clay stabilizer [133].

The S_R values for 1%, 10% and 30% ammonia were 1.001 (0.1%), 1.004 (0.4%), and 1.008 (0.8%), respectively (Shown in Figure 3-3). Although all swelling ratios for coal B particles in the three ammonia solvents were very low, it is clear that the extent of coal swelling increased with the ammonia concentration.

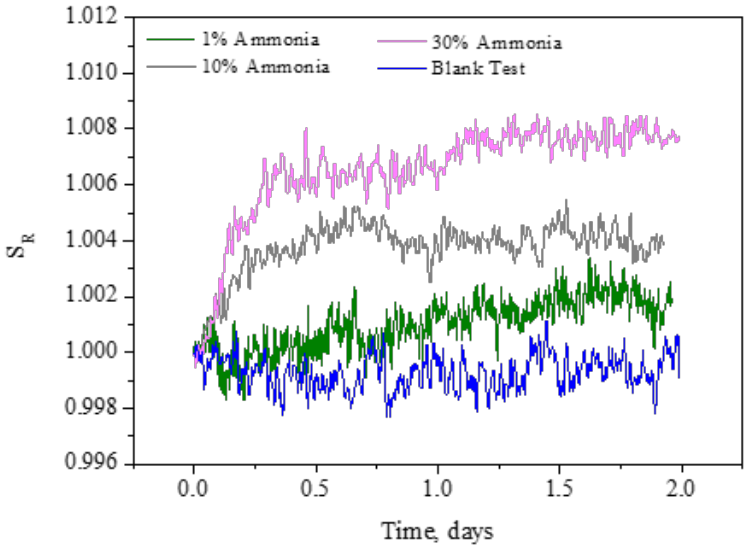

Figure 3-3: Swelling ratio, S_R of unconstrained coal B particles in ammonia.

The S_R for 1%, 10% and 70% ethanol solutions were 1.004 (0.4%), 1.010 (1.0%), and 1.026 (2.6%), respectively (Figure 3-4a). The S_R of coal B particles in ethanol also increased with the increasing ethanol concentration.

In terms of S_r for 70% ethanol (Figure 3-4b), the increase in S_r could not be observed in the time frame used (6 hrs), indicating a rapid reaction at the beginning. S_r reached its peak value and then kept dropping until 16 hrs, at which point, particle swelling stopped.

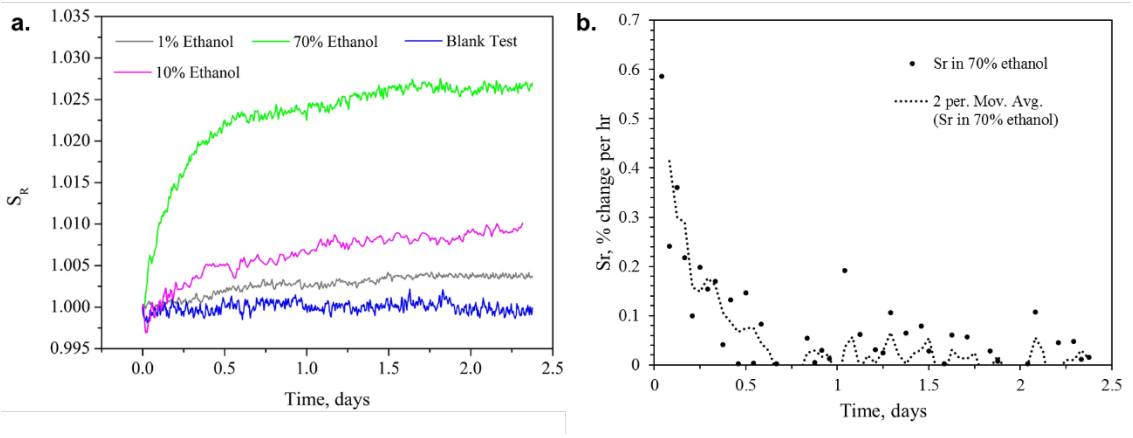

Figure 3-4: Swelling ratio, S_R (a) and swelling rate, S_r (b) of unconstrained coal B particles in ethanol.

Figure 3-5 shows the swelling test result for 10% tetramethylammonium chloride. The S_R curve in clay stabilizer almost overlaps the blank curve, which means coal B is not expected to react with the clay stabilizer.

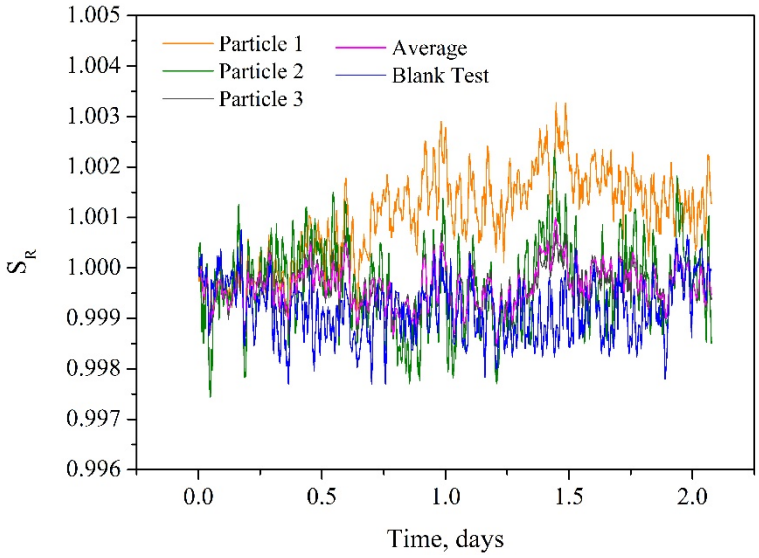

Figure 3-5: Swell ratio (S_R) of unconstrained coal B in 10% tetramethylammonium chloride.

3.3.3 Coal B swelling behaviour in candidate oxidants

In terms of permeability, the importance of the swelling test is that it can quickly screen the behaviour of the coal particles in different oxidants to mimic the phenomenon that may occur in the coal cleats where the oxidants would flow.

The basic hypothesis is that if the coals swell in the cleat in situ, it would decrease the cleat aperture, thus decreasing the permeability. However, if they could shrink due to reactive dissolution (etching) in oxidants, it would dilate the cleats and increase the permeability. Additionally, numerous researchers have reported that coal, regard less of the types, could be dissolved by oxidants [16, 20, 21]. The permeability might be increased by coal solubilisation and the enlargement of the original fractures and/or the generation of new fractures.

3.3.3.1 Sodium Hypochlorite (NaClO)

Coal B swelling tendency in NaClO was examined under increasing oxidant concentration (0.1%, 1% and 10%). Figure 3-6 and Figure 3-7a show the swelling trends in 0.1% and 1% NaClO, respectively. Coal B particles in 0.1% NaClO showed an average S_R of 1.005 (+0.5%), whilst those particles in 1% NaClO swelled as well, with an average S_R of 1.15 (+15%). Coal B swelling in 10% NaClO was conducted but no meaningful trend could be derived due to excessive particle breakage and movement.

Due to the low S_R of coal B in 0.1% NaClO, only S_r of particle 1 in 1% NaClO was generated, as shown in Figure 3-7b. It marginally increased in the first 20 days and shot up to a peak

in the following 5 days and then generally decreased. The general S_r trend here is similar with that in pyridine, although they had very different swelling periods.

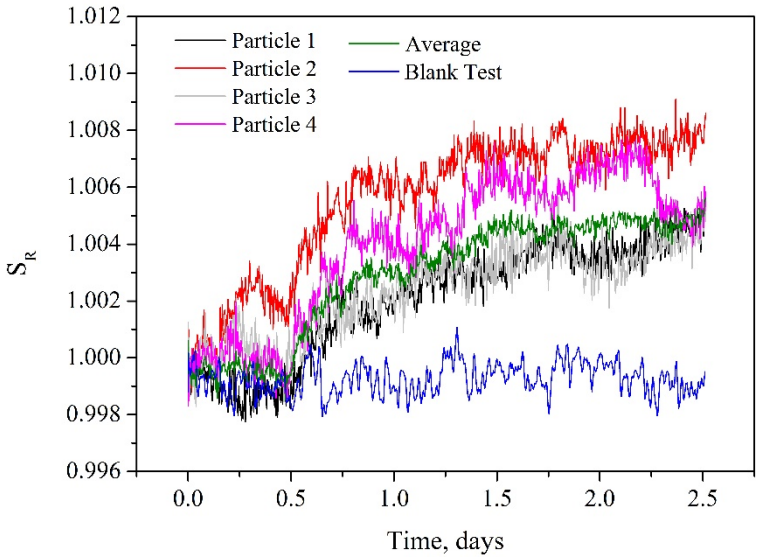

Figure 3-6: Swelling ratio, S_R of unconstrained coal B particles in 0.1% NaClO.

For 1% NaClO, the details of individual coal B particles are of particular interest shown in Figure 3-7a. Firstly, the blank test (blue line) provides a clear reference from which to distinguish the unreacted coal from the swollen oxidant-reacted particles.

Particles 1 and 2 showed gradual swelling for the first 35 days and apparently ceased to swell and maintained their swollen state for another 10 days. This swelling behaviour could also be observed in Figure 3-8, where images of the particles before and after the oxidation in 1% NaClO are compared. In Figure 3-8, the blue solid line, showing the outline of particle 2 post-treatment, is larger than the red dash line, showing the same particle outline pre-treatment. This difference indicates the swelling of particle 2. Additionally, it is noteworthy that this particle expanded to a greater extent in the X axis, rather than Y axis, which illustrates that the coal swelling is not uniform, but anisotropic. Coal anisotropic swelling is widely reported whereby the coal tends to swell more in the direction perpendicular to the bedding plane than parallel to it [113, 119, 120]. Cody et al. proposed the main reasons for the anisotropic swelling to be the pressure to which coals are subjected during their formation and maturation as well as the anisotropic distribution of cross-links [113]. The anisotropic swelling is also observed with other particles in 1% NaClO, but just not shown here.

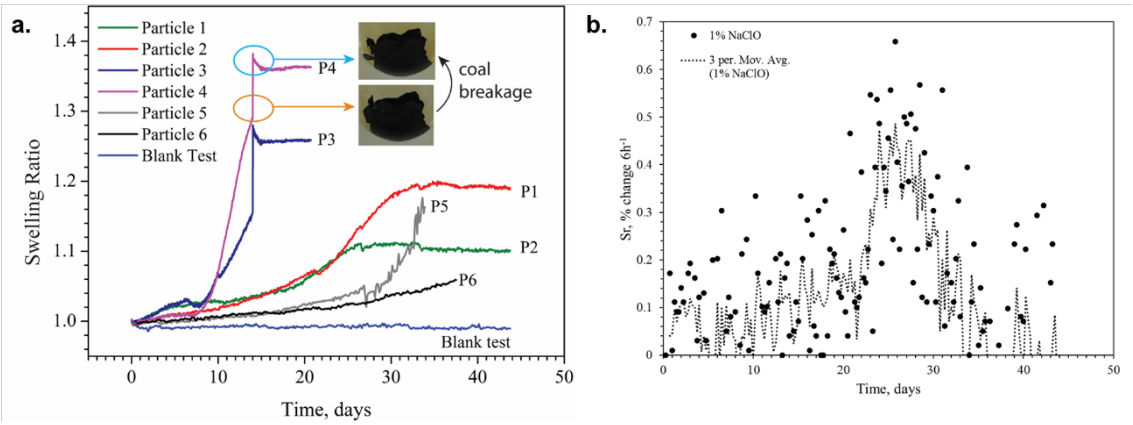

Figure 3-7: Swelling ratio, S_R (a) and swelling rate, S_r (b) of unconstrained coal B particles in 1% NaClO.

In addition to swelling, some coal B particles in 1% NaClO broke (Figure 3-7a, particles 3 and 4). In detail, coal particles 3 and 4 displayed rapid swelling followed by breakage after 13 days. The breakage of particle 4 is clearly shown by comparing the two images in Figure 3-7a.

Images a and b in Figure 3-8 show the swelling test images of coal B before and after oxidation, respectively. Comparing particle 4 in these 2 images, clear coal breakage could be observed and the particle seems to sit together as a single particle in Figure 3-8b, but when the solution was siphoned out, it was clear that the particle had broken into small parts (Figure 3-8c). This was also observed for the pyridine swelling experiment.

In Figure 3-7a, particles 5 and 7 kept swelling for 31 days, but no data recorded afterward. This is due to the serious discolouration of the solution, which disabled the camera to capture the actual outline of the particles. The discolouration of the solution indicated that coal solubilisation in NaClO was occurring.

The various reaction phenomenon displayed from coal particles sourced from a single coal core highlight the unique physico-chemical make-up of each particle. This is likely due to the highly heterogeneous nature of coal, wherein maceral compositions and physical geometry differ spatially.

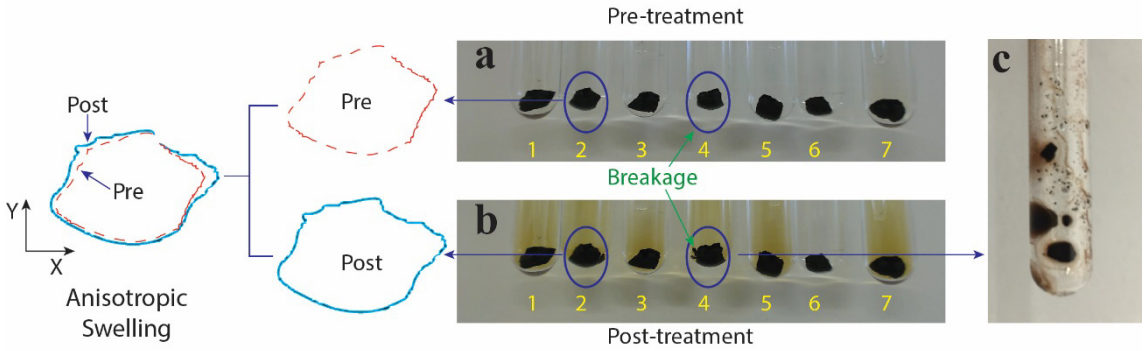

Figure 3-8: Different coal B behaviours in 1% NaClO.

Figure 3-9 shows the leaching test results of coal B in NaClO solutions. Results show elevated amounts of dissolved organics with increasing NaClO concentrations. Sample mass loss in 0.1%, 1% and 10 % NaClO were 0.95%, 2.21% and 14.61%, respectively, while the corresponding TOC in the filtrate were 23 mg/l, 376 mg/l and 526mg/l, respectively. Sample mass loss and TOC in filtrate increased with increasing NaClO concentration. Both the change in mass and TOC provides clear indication of coal component solubilisation in NaClO.

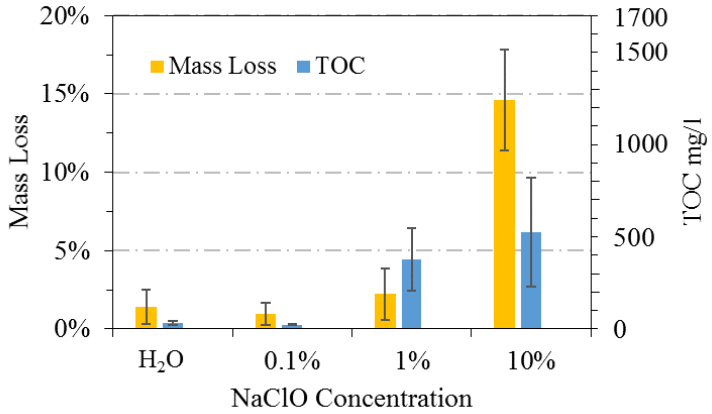

Figure 3-9: Mass loss and TOC in the leachate after coal B oxidation by NaClO solutions.;

The samples used in the leaching test were carefully selected without visible minerals. TOC results illustrate that sample mass loss was predominantly attributable to carbon loss. As shown in Table 1, the carbon content of the coal sample was 85.54%. In Figure 3-9, the scales of mass loss and TOC on the Y axes were designed to match each other according to carbon material balance if the filtrate was the only destination for the carbon in coal after oxidation. It shows that within the error limit, the sample mass loss matched well with the

TOC in 0.1% and 1% NaClO, except for 10% NaClO, in which the mass loss is higher than TOC suggesting that carbon might be released in the form of CO_2. Researchers have found that the products from coal oxidation in NaClO are mainly composed of benzene carboxylic acids, chloro-substituted short-chain alkanoic acids or long-chain alkanedioic acids and CO_2 if strong oxidation occurs [16, 17].

Combining image analysis of coal particles treated with NaClO and leaching test results, coal swelling, coal solubilisation and coal breakage were all observed. Coal swelling may cause coal cleat apertures to decrease and consequently cause permeability to decrease, while coal solubilisation could allow increase in permeability. The effect of coal breakage is not clear, because if the new cracks could be generated and connect the coal cleats, this could increase the permeability. Although, if coal breakage generates coal fines, it could block the coal cleats and decrease coal permeability. The phenomena described above renders the net effect of NaClO on coal permeability unclear, therefore further investigation of the effect of NaClO is warranted, especially permeability testing under confining pressure.

3.3.3.2 Potassium Permanganate ($KMnO_4$)

Few references exists that report coal oxidation by permanganate and only limited information could be found in the study of Norton et al. [102] and Moore et al. [98]. Manganese in permanganate oxidises coal by reducing from +7 to +4 oxidation state.

Because the permanganate is a coloured solution, which will influence the calculation of the S_R from image analysis, a modification of the swelling test was applied as described in section 3.3.2. Therefore, only the S_R in the initial (with 4% KCl) and the final stage (after HCl injection) were obtained to calculate the S_R. The final S_R results are shown in Table 3-3. Results show that the coal B particles tended to swell more with increasing permanganate concentration until a threshold, 3% in this study, where the coal particles appeared to disintegrate.

Table 3-3: Summary of swell ratios of unconstrained coal in $KMnO_4$.

[$KMnO_4$], %	0.015	0.03	0.1	1	3	5
Swelling Ratio, S_R	1.008	1.015	1.02	1.05	Undetermined*	Undetermined*

* Undetermined due to particle breakage

Leaching test results also show that the coal could be oxidised significantly in permanganate (Figure 3-10). After oxidation by 5% $KMnO_4$, around 13% of coal could be dissolved and the TOC could be as high as 1800 mg/l in the liquid. A similar trend as that in the swelling test, higher permanganate concentration yielded more mass loss and TOC. Additionally, only permanganate concentration above 1% seems to be effective compared with the blank test in distilled water. A general mass balance was also achieved based on the mass loss and the TOC in the solution after permanganate oxidation. The reason that the TOC in filtrate was higher than the mass loss might be due to the generation of MnO_2 remaining in the coal sample residue, although the residue underwent 1% HCl flushing after filtration.

The massive mass loss as well as the coal breakage indicate that the coal B structure could be changed significantly with permanganate oxidation. Under confining pressure, it may have the potential to create void space or new cracks that could increase the permeability.

The main challenge is the potential deposition of MnO_2 from the decomposition of potassium permanganate [102]. Published experiments have shown the reduction in permeability of sandstone caused by the pore plugging of MnO_2 precipitates when the authors tried to use the $KMnO_4$ to remove the dense non-aqueous-phase liquids [134, 135]. Therefore, how to prevent the MnO_2 generation or remove the MnO_2 properly could become the main research target in terms of the permanganate oxidation to increase coal permeability.

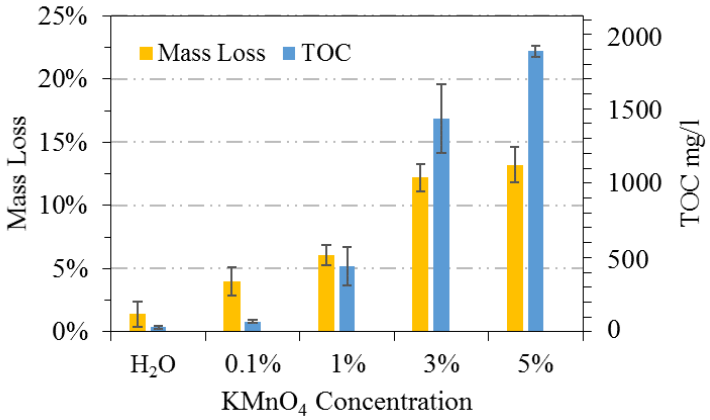

Figure 3-10: Mass loss and TOC in the leachate after coal B oxidation in $KMnO_4$ solutions.

3.3.3.3 Potassium Persulfate ($K_2S_2O_8$)

The persulfate ion ($S_2O_8^{2-}$) is a strong oxidant (E° = 2.1 V) that under certain reaction conditions can generate free sulphate radicals ($SO_4^{\bullet-}$, E° = 2.6 V) [71].

1% and 3% $K_2S_2O_8$ were used in both of the swelling test and leaching test for coal B. The solubility of $K_2S_2O_8$ in water is only 4.5% at 20 °C, which means 3% $K_2S_2O_8$ is a relatively high concentration. Figure 3-11 shows the S_R for coal B in 3% $K_2S_2O_8$. The coal did swell in 3% $K_2S_2O_8$ but with a relatively lower S_R (1.02) compared with 1% NaClO (1.15).

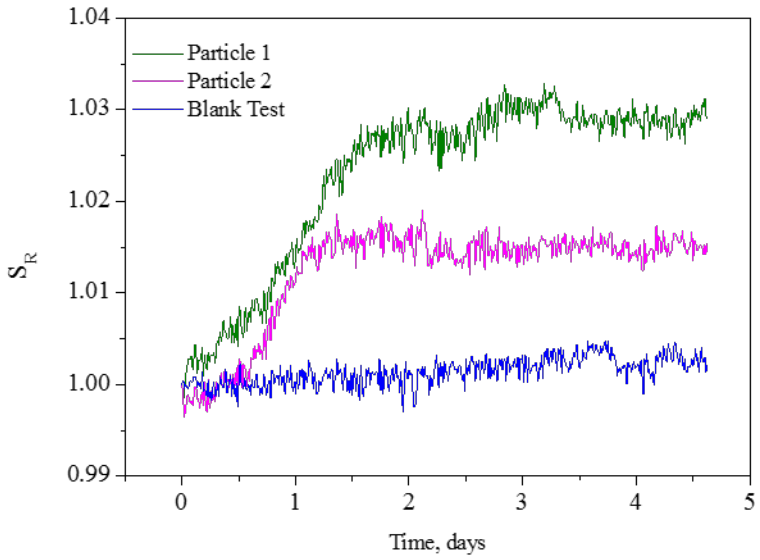

Figure 3-11: Swelling ratio, S_R of unconstrained coal B particles in 3% $K_2S_2O_8$.

Coal B swelling behaviour in 1% $K_2S_2O_8$ is not shown here because of the discolouration that happened during the test, whereby the solvent became brown and prevented the identification of coal particle outlines. This colour change indicates the reaction between coal and persulfate. After HCl injection, however, the solvent returned back to transparent. The final S_R was calculated as 1.02. The solution discoloration in 3% $K_2S_2O_8$ was not as high as in 1% $K_2S_2O_8$.

Figure 3-12 shows the leaching test results in $K_2S_2O_8$. Compared with the leaching test results in NaClO or $KMnO_4$, the mass loss and the TOC are relatively low in persulfate, similar with those in distilled water, even less as in 3% $K_2S_2O_8$.

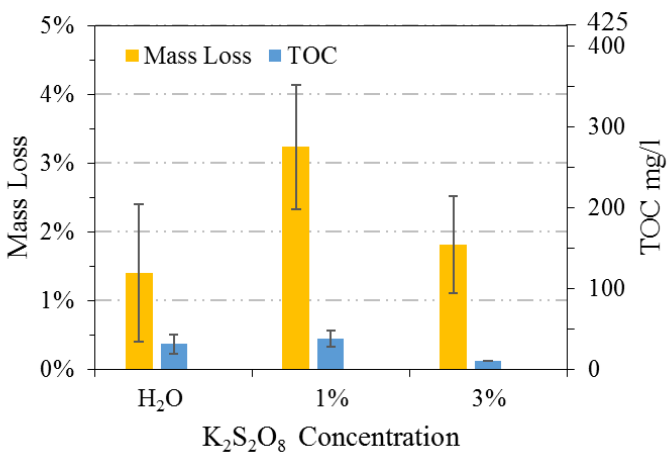

Figure 3-12: Mass loss and TOC in the leachate after coal B oxidation in $K_2S_2O_8$ solutions.

The results from both swelling test and leaching test indicate that the reaction between $K_2S_2O_8$ and coal B was not vigorous.

3.3.3.4 Hydrogen Peroxide (H_2O_2)

H_2O_2 is also a commonly used industrial oxidant as describing previously. The S_R could not be calculated in the tests with H_2O_2 due to coal particle rotation caused by the bubbles generated during the test. The bubbles could be oxygen from the degradation of hydrogen peroxide [136] or CO_2 as the oxidation product [73, 137]. The leaching results, as shown in Figure 3-13, indicate that H_2O_2 seems not to react with coal B significantly, because the mass loss is similar to the blank test and the TOC is negligible even in 30% H_2O_2.

The relatively slight reaction between H_2O_2 and coal matrix has been reported. Vasilakos et al. found that H_2O_2 could remove the sulphur that is pyrite in coal, but not affect the rest of the organic coal matrix [18]. Liu et al. also reported that the H_2O_2 seems to be suitable only for low-rank coals because of its relatively low reactivity toward coal degradation [20].

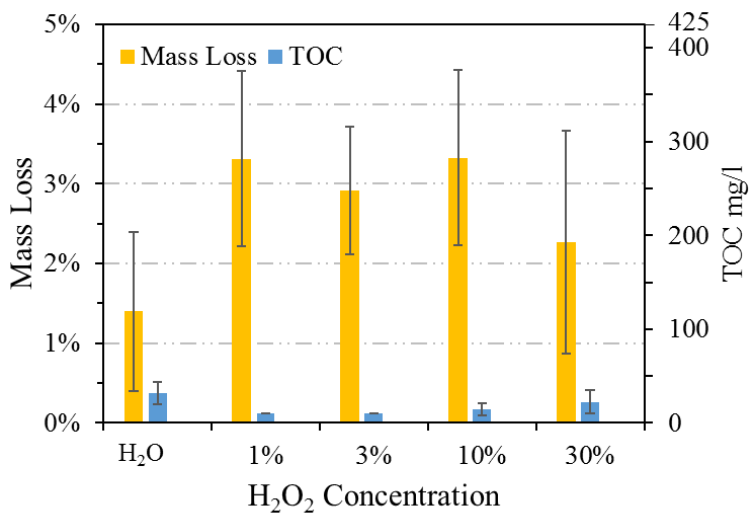

Figure 3-13: Mass loss and TOC in the leachate after coal B oxidation in H_2O_2 solutions.

The coal oxidation mechanism by H_2O_2 was reported by Mae et al who proposed that H_2O_2 could introduce –OH and –COOH into coal, and break the weak bridged bonds like C–O–C connecting condensed aromatic rings to generate CO_2 and water soluble organic compounds [137]. Liu et al. proposed both covalent bond cleavage and organic functional groups introduction resulted in higher reactivity and hydrophilicity of coal, so they used H_2O_2 to pre-treat the coal and then oxidised the coal with NaClO and they proved that the increase in hydrophilicity improved interaction between coal particles and NaClO, and thereby promoted coal oxidation by NaClO [20]. Additionally, Vasilakos et al. found that the reaction between H_2O_2 and coal could be enhanced significantly when a small amount of sulphuric acid was added [18]. Therefore, the H_2O_2 oxidation of coal under acid conditions might produce improved results.

3.3.4 Effects of large particle and higher viscosity oxidant on coal B swelling behaviour in aqueous NaClO

Given the fact that coal displayed swelling and breakage when it came into contact with oxidants (e.g. NaClO), a reasonable assumption was proposed that the oxidant molecule penetrates into the coal structure and cause the coal structure to relax. To hinder the oxidant penetration and keep the oxidation at the surface of the coal, some trials were conducted including using larger coal particles (~20mm) and higher viscosity solution.

Figure 3-14 compares the different behaviours between small and large particles of coal B in 1% NaClO. The equilibrium stages show the less swelling of larger coal particles, indicating that the swelling could be reduced by increasing particle size.

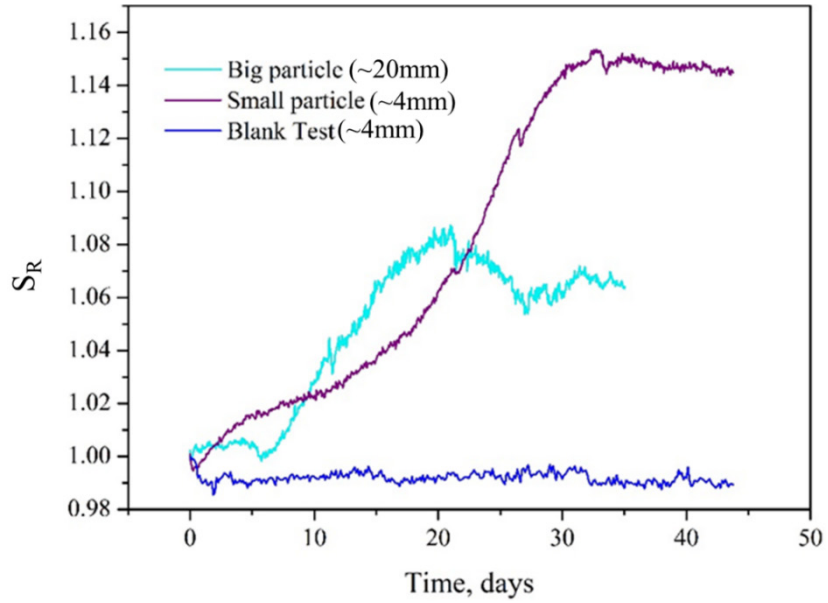

Figure 3-14: Comparison of behaviours between small and large particles of coal B in 1% NaClO

Figure 3-15 described the difference of coal B behaviours in 2.4% gel NaClO and 2.4% aqueous NaClO in the first 8 days, because afterwards, the gel solution colour was too dark to distinguish the actual coal particle shape. In this period, gel NaClO caused more swelling than aqueous NaClO, suggesting that the gel also interacts with the coal.

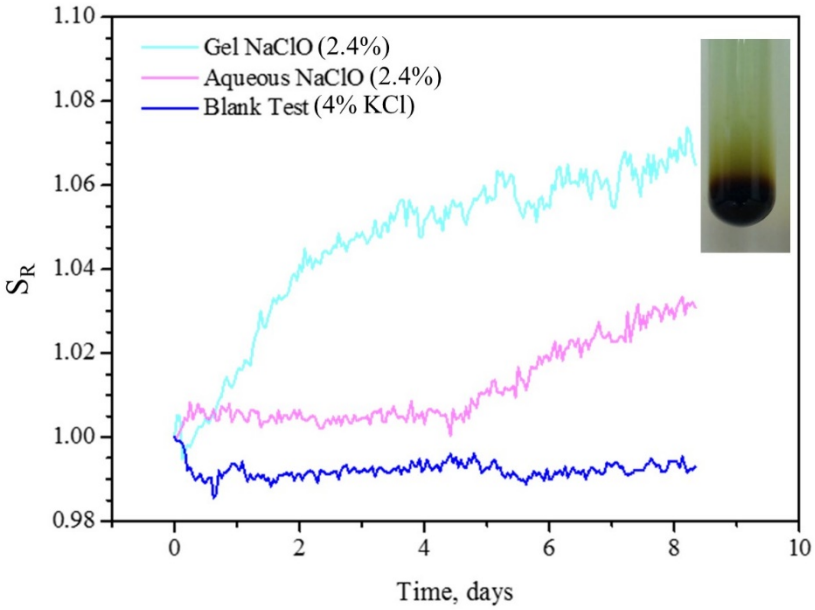

Figure 3-15: Comparison of coal B behaviours in 2.4% gel NaClO and aqueous NaClO

3.3.5 Comparison of two different coal behaviours in oxidants

The net effectiveness of oxidation on coal seam gas stimulation may be contingent on either the coal rank or maceral composition or both. Low rank coals have previously been proposed to be easily oxidized by NaClO [17]. Therefore, the swelling and leaching test were conducted based on two different coals as mentioned in section 3.1.

This research found that NaClO was the effective for coal dissolution and that the difference between coal S and coal B oxidation was significant in NaClO but indiscernible in other oxidants including $KMnO_4$, $K_2S_2O_8$, H_2O_2. Therefore, the comparison of swelling behaviour of the two studied coals are examined in detail for NaClO, and generally in other oxidants.

3.3.5.1 Comparison of behaviours of coal S and Coal B in 5% NaClO

The swelling test is a valuable method not only to examine coal particle size change but also to visualise the coal particle behaviours in oxidants. For instance, the solution colour variation in the swelling test could give clues about the reaction occurring during the experiment, and the breakage of coal particles might illustrate physical effects of oxidation on coal structures. For both coal B and coal S, swelling tests were conducted as shown in Figure 3-16, where the green line shows coal B swelling ratio (S_R) and the red line shows coal S S_R.

For each coal, the swell test procedure was divided into 3 stages based on the solution colour. In stage I, the solution was clear where the coal outline could be accurately distinguished by visual examination. For coal B, this stage lasted on average 9 days and coal swelling (S_R=1.5) could be observed. However, for coal S, this stage was less than one day with an indiscernible S_R.

Stage II was a brown colour stage where the dark colour shows the product from coal oxidation (Figure 3-16). This was also observed by Mayo et al. (1979) [88]. In this stage, the optical recognition of the particle boundary is diminished, thus the S_R was less accurate, as represented by dash line for each coal. The solution colour change was accompanied by coal breakage in both samples. For coal S, the dashed line fluctuation is due to refreshment of the solution after siphoning the old solution out. Coal S quickly progressed to stage II with a dramatically dark colour change, so the solution was refreshed three times to examine the particle behaviour. After each refreshment, again the solution quickly became dark.

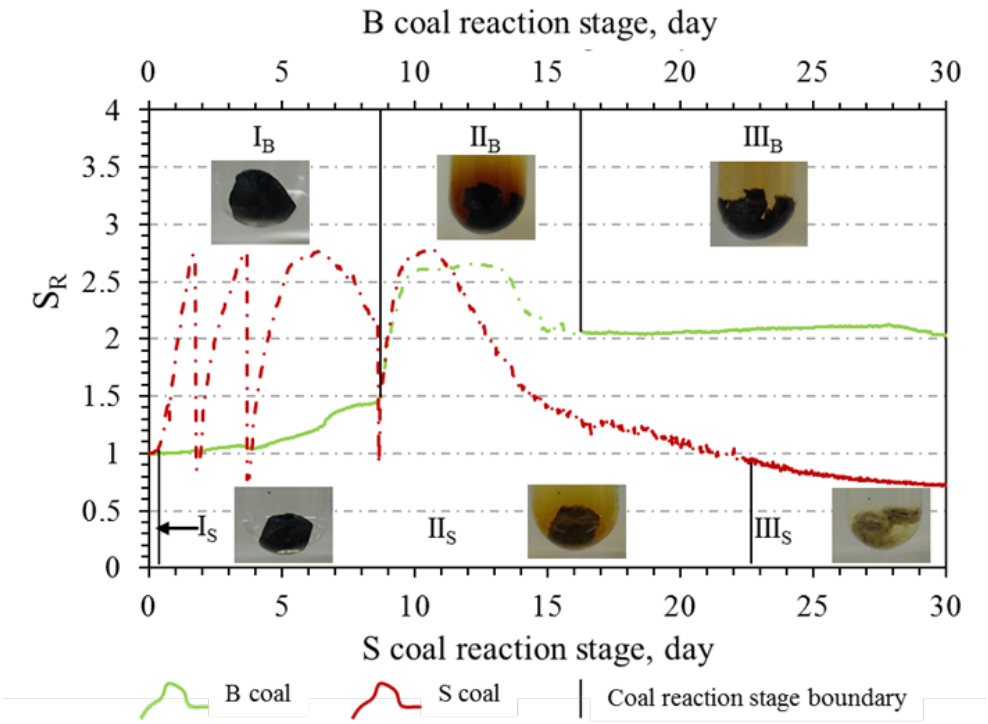

Figure 3-16: Swell/shrink behaviours of different coal sample particles in 5% NaClO.

Finally, Stage III is where the solution becomes clearer again probably due to the remaining NaClO decomposing the initial oxidation products and reaction was approaching equilibrium. The solution colour changing from dark to light during oxidation was also observed previously [17, 73]. In stage III, although the solution was not perfectly clear, it is

clear enough to observe the particle outline more accurately. The Final S_R for coal B and coal S were 2.0 and 0.73, respectively. Coal breakage occurred for both coals. The oxidation product could be visually observed on the surface of the coal particle, most prominently for coal S (stage III_s in Figure 3-16). It could be concluded from the images that swelling, breakage and dissolution are occurring where dissolution is dominating for coal S, thereby giving a swelling ratio <1, while swelling appears to be dominating for coal B with a swelling ratio >1.

The colour change in the swelling test qualitatively indicates coal solubilisation in 5% NaClO, while the leaching test demonstrates the reaction quantitatively by measuring the coal sample mass loss as well as the TOC in the filtrate. Figure 3-17 shows the leaching test results for coal B and coal S as well as the blank test based on coal B. The blank test was used to investigate artefacts of stirring and filtration on experiment results. Artefacts were proven negligible with only a slight mass change (1.4%) and negligible TOC (37 mg/L) in the blank test compared with those in 5% NaClO. Coal B exhibited 4.5% mass loss and 430 mg/L TOC and coal S showing 49% mass loss and 3840 mg/L TOC in the filtrate. The solubilisation of the coal was based on powdered samples, with a large particle size surface area. It should be noted that while only 4.5% of coal B dissolved in NaClO on this initial leach, 42.5% dissolved in an identical second leach which is described in Chapter 5 (section 5.3).

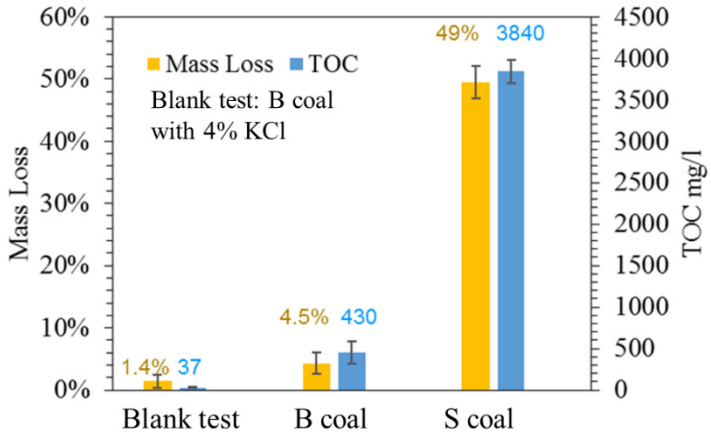

Figure 3-17: Mass loss and TOC in the filtrate of different coal samples after oxidation by 5% NaClO.

3.3.5.2 Comparison of coal S and coal B oxidation in $KMnO_4$, $K_2S_2O_8$ and H_2O_2

Coal S was exposed to $KMnO_4$ with 4 different concentrations (0.1%, 1%, 3% and 5%). In all the tests, coal S showed swelling behaviours, although the S_R varied with different concentrations. The coal S S_R in 0.1% $KMnO_4$ was 1.01 while the corresponding S_R of coal B was1.02. Coal S behaved similarly in 1% $KMnO_4$ (S_R=1.01) as in 0.01% $KMnO_4$, and swelled less than coal B (1.05) in the same solution. In higher concentrated $KMnO_4$ solution, coal S were oxidised to produce coal fines, which was the same for coal B.

Coal S exhibited similar behaviour in $K_2S_2O_8$ and H_2O_2 as Coal B. In 3% $K_2S_2O_8$, coal S swelled slightly less (S_R=1.01) than coal B (S_R=1.03). In 10% H_2O_2, indiscernible difference could be observed between the two studied coals. For both coals, H_2O_2 caused massive bubbles leading to the coal particle movement which disabled the calculation of the S_R.

Besides, leaching test results did not indicate any difference between the two studied coals in $KMnO_4$, $K_2S_2O_8$ and H_2O_2, regardless of the oxidant concentrations. In $KMnO_4$, the generation of MnO_2 cause significant error to the measurement of mass change before and after oxidation, while $K_2S_2O_8$ and H_2O_2 only dissolved negligible coal S, similar with coal B, compared with the blank test in pure water.

3.4 Discussion

In terms of the swelling tests, the highest S_R of coal B in the different concentrations of NaClO, $KMnO_4$ and $K_2S_2O_8$ observed in this study were 15%, 5% and 2%, respectively. No S_R data was available in H_2O_2 due to the drastic particle movement during test. Coal breakage was observed in NaClO and $KMnO_4$, but not $K_2S_2O_8$ and H_2O_2.

Comparing the leaching test results for all the oxidants involved, coal B dissolution was primarily achieved in NaClO and $KMnO_4$, while negligible in $K_2S_2O_8$ and H_2O_2 as shown in Figure 3-18a and Figure 3-18b, which summarise the mass loss and TOC after oxidation in different candidate oxidants, respectively.

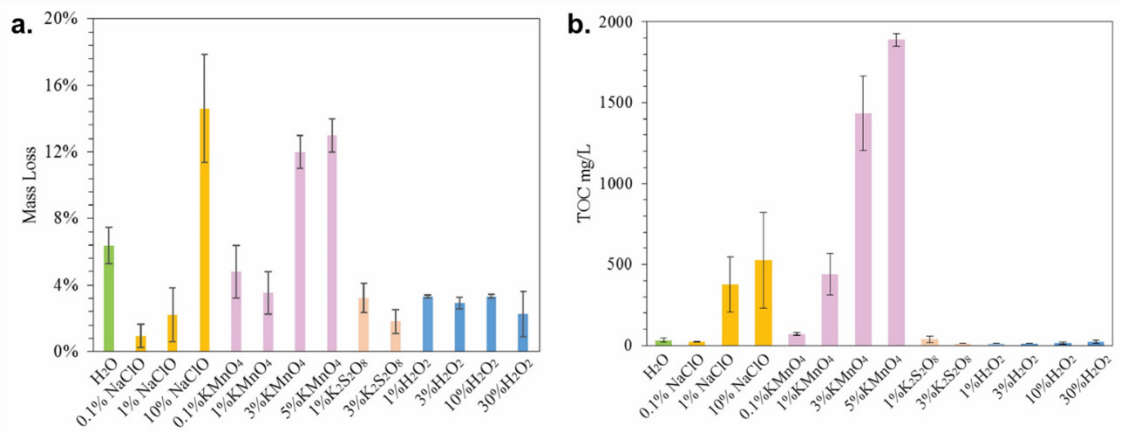

Figure 3-18: Comparison of the mass loss from coal (a) and TOC (b) after leaching tests.

Above all, compared with $K_2S_2O_8$ and H_2O_2, NaClO and $KMnO_4$ could dissolve coal significantly with the associated effect of relatively large coal swelling. Based on the current results, $KMnO_4$ is less favourable than NaClO because it has a solid oxidation product (MnO_2), which might precipitate in the coal cleats, thus decreasing coal permeability. Therefore, NaClO is considered to be the most promising oxidant compared with other oxidants involved in this study.

The interaction between oxidants and coal appears to be a combination of physical and chemical mechanisms. This research set out to examine whether oxidants could cause etching, i.e. a reaction at the coal surface to give soluble reaction products. Given that in all the tests, coal B swelling was prevalent and no coal particle size decreased, it appears that etching is difficult to achieve for this coal. However, the particle size of coal S did decrease after oxidation and this decrease might be resulted from the massive dissolution of coal S in NaClO.

The prevalence of swelling for coal B, regardless of using big coal particles or the gel oxidant, indicates that the oxidant is not reacting at the surface of the coal, but rather it is penetrating into the particle and reacting internally. This internal reaction caused the coal structure to relax leading to swelling.

If the general consideration of swelling would be to decrease the cleat aperture, then the observation of anisotropic swelling might indicate that swelling is not detrimental to cleat aperture, because the coal might swell in the direction parallel to the cleats rather than

perpendicular to them. Therefore, the swelling might not decrease the cleat aperture. This should be investigated further.

The TOC measurements show that coal oxidation is resulting in soluble reaction products. The solubilisation of coal might benefit the coal permeability by generating new channels in the coal matrix.

The breakage of the particles in oxidants is of particular interest and has not been reported. It seemed to occur when the degree of swelling or rate of swelling was high. The breakage could be due to a combination of chemical and physical mechanisms. Chemical mechanisms are by way of bond breaking leading to soluble reaction products, and physical mechanisms are by way of the propensity for swelling causing internal stress to build up to a level that is sufficient for the physical breakage of bonds.

The physical breakage is particularly interesting in this research. The coal particles in this study are unconfined, however, the coal seams are confined, and it is not yet known how the coal would respond to the oxidants under confined conditions. Perhaps the propensity for swelling will cause higher internal stresses and more breakage. The next phase of this research involves core flooding experiments combined with micro-CT analysis to examine the chemical and physical effects that have been noticed here and their influence on permeability.

The swelling and leaching test results suggest that coal S is more reactive to NaClO oxidation than coal B. The high solubilisation (50% in coal powder samples) and low swelling ratio (<1) of coal S in 5% NaClO illustrate that coal S permeability might be increased after 5% NaClO oxidation.

3.5 Conclusion

Screening of potentially useful oxidants for coal seam gas application was achieved by a time-lapse photography-image analysis test combined with leaching test in oxidising solutions. Coal oxidation to increase coal permeability shows promise.

Three oxidation effects, of coal swelling, coal solubilisation and coal breakage were observed. The coal used in the experiment (Permian coal) tends to swell in both solvents and oxidants, and swelling increases with higher concentrations.

Four oxidants were tested in the study, including NaClO, $KMnO_4$, $K_2S_2O_8$ and H_2O_2. Coal B reacted vigorously with NaClO and $KMnO_4$, but only slightly with $K_2S_2O_8$ and H_2O_2. After a certain amount of swelling coal B particle breakage was observed (1% and 10% NaClO and 3% and 5% $KMnO_4$). Anisotropic swelling was clearly observed for coal B in 1% NaClO. Higher dissolution for coal B appears to happen in NaClO and $KMnO_4$, and negligible in $K_2S_2O_8$ and H_2O_2. In terms of oxidation to enhance permeability for coal B, NaClO and $KMnO_4$ are more promising than $K_2S_2O_8$ and H_2O_2.

The lower rank coal S was more reactive with NaClO than coal B according to coal mass loss and TOC in solute filtrate. Coal S showed 49% mass loss and 3840 mg/L TOC in the filtrate, while coal B exhibited 4.5% mass loss and 430 mg/L TOC. Based on the results and discussion, coal S permeability is expected to increase more after NaClO stimulation at in-situ conditions.

For the situation of in-situ application, it remains unclear if the net effect of coal swelling and coal solubilisation will be an increase or decrease in permeability. The anisotropic swelling of coal is expected to relieve the detrimental effects of coal swelling on permeability. In addition, coal breakage may lead to new void space or new cracks in the coal matrix, which has the potential to increase the coal permeability. Confined core-flooding tests that simulate in-situ conditions are required to elucidate this behaviour.

Chapter 4. NaClO oxidation effects on coal pores and cleats

4.1 Introduction

In chapter 3, unconfined coal particles presented different behaviours including dissolution, swelling, and breakage. It was proposed that coal dissolution by NaClO might enlarge coal cleat apertures, while swelling might narrow them, but the net effect was unclear. The effect of breakage was also indiscernible, as breakage might generate new fractures in coal seams increasing fracture system connectivity. On the other hand, coal breakage might lead to coal fines generation that can block the fractures thus decreasing the permeability. Due to the propensity for swelling, it was apparent that the effects of oxidants on both confined and unconfined samples needed to be studied. This chapter reports the effects of oxidants on artificial coal cleats within a cleat flow cell that enables cleat aperture to be measured before and after treatment.

While the coal cleats play a significant role in contributing to the permeability [50, 58, 64, 138], matrix permeability may also be important [2]. How these two types of permeability interact with each other determines the overall gas production characteristics for a well [2, 50, 64]. The matrix permeability is determined primarily by the connectivity and distribution of the pore system within the coal matrix, especially macro- and mesopores [2]. It has been shown that higher diffusivity was generally related to greater macropore porosity in coals [138]. Gamson et al. (1996) [138] also suggested that the presence of open and continuous microstructures (micro-fractures in bright coal and micro-cavities in dull coal) might enable laminar flow to begin before gas enters the cleat. Therefore, if the process of coal oxidation increases the pore system connectivity or generates “micro-structure” in the matrix, it might be of particular importance with respect to total permeability and overall gas production. Additionally, this stimulation method only targets small areas in the near wellbore region, so it is not likely to influence future mining activities.

Therefore, two coals, coal S and coal B, from CSG production basins (Surat and Bowen basins) in Queensland, Australia, were used to investigate the effects of NaClO oxidation

on coal pore and cleat structures. The relationship between these structure changes and the coal permeability is discussed.

4.2 Methodology

4.2.1 Porosity characterisation

The bulk or apparent density (ρ_{Hg}) of the coal samples was measured by mercury intrusion porosimetry (MIP, Micromeritics PoreSizer 9320) and the skeletal density (ρ_{He}) by helium pycnometry (Micromeritics AccuPyc II 1340). The total accessible coal porosity ($\emptyset$) was calculated using Equation 4-1.

$$\emptyset(\%) = \left(\rho_{He} - \rho_{Hg}\right)/\rho_{He} \times 100 \qquad \textit{Equation 4-1}$$

As coal porosity change could not be measured on the same coal particles, because MIP is a destructive test, a total of 10 g (3-4mm coal particles) from each coal core was divided into 4 sub-groups by “cone and quartering”. Then any two of these sub-groups were randomly collected to conduct the porosity test. The two chosen sub-groups were separately treated with 5% NaClO and 4% KCl for 7 days. After treatment, the samples were filtered and dried in an oven at 110 oC for 12 hrs. The porosity tests were repeated twice to assess reliability.

4.2.2 SEM and microscope imaging before and after oxidation

For SEM imaging, two groups of coal particles (3-4 mm) were arbitrarily picked from each of the coal cores and were saturated in 5% NaClO and 4% KCl for seven days, respectively. After treatment, the samples were rinsed with distilled water and dried at 110 °C for 12 hours. The dried coal particles were mounted on aluminium stubs, and sputter-coated with a layer of iridium using a Q150 TS sputter coater (Quorum Technologies, UK). The coal particles were then viewed using SEM JSM-7001F at 15 kV.

For microscope imaging, the machine and procedures were descripted in section 3.2, and the coal particles (< 1mm) were treated with 5% NaClO and 4% KCl, respectively, to examine the effect of NaClO oxidation.

4.2.3 Cleat Flow Cell (CFC)

To investigate the oxidant effect on coal cleats, we used the cleat flow cell (CFC) reported by Mahoney (2017) [139] to observe the change in the width of artificial channels in coals before and after oxidation by flowing oxidant through scribed channels, as shown in Figure 4-1.

Coal cubes (each 15mm length) were cut perpendicular to the bedding plane and mounted in epoxy blocks. The mounted samples were ground and polished for incident light microscopy according to the procedures in Australian Standard AS2061 (1989). Following the polishing, coal samples were scribed with a 100 μm tungsten-carbide cutting tool at an angle of approximately 55° to ensure that only the sharp corner edge of the cutting tool would scribe the coal surface. The cutting tool was moved by hand control across the coal block at speeds of approximately 5 - 10 mm/s. Cutting speed within this range does not have a significant effect on the produced channel characteristics [139].

For the scribed channel, an optical image was first collected with a Leica DM6000 light microscope equipped with a Leica DFC365 FX Digital high-speed camera. Image analysis was performed with the Leica Application Suite Advanced Fluorescence software package. Channel apertures were measured with Image-J Version 1.46r. Due to the fine polish of coal, the maceral composition where the artificial channel passed could be identified on the coal sample surface from the microscope image. After the initial image was obtained, the top of the coal channel was sealed with a polyolefin film.

The oxidant was injected to the channels from a 10 mL syringe pump connected with Tygon tubes to inlet and outlet holes (1.5 mm in diameter), as described in Mahoney et al. (2015) [140] and Mahoney et al. (2017) [139].

The 5% NaClO solution was injected at a rate of 10 μL/min to reduce the physical effect of fluid flooding on the channel structure. After injection, the sealing film was peeled off and channel images after oxidation were collected. The peeled off film was clean in the channel area excluding the artificial effects on the cleat aperture change. Based on the images before and after oxidation, the channel apertures and shapes of interest could be compared. A set of channels were also flooded with 4% KCl to provide a reference experiment without oxidation.

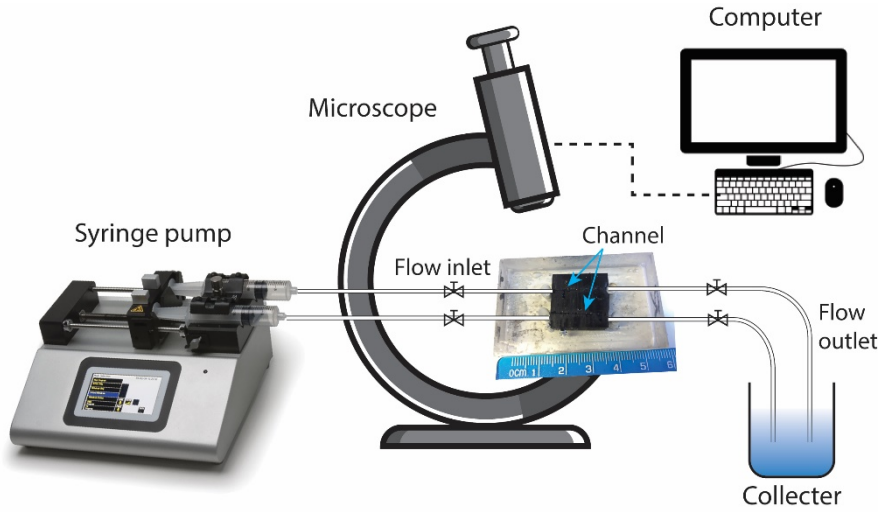

Figure 4-1. Schematic of the cleat flow cell apparatus with the expoxy-mounted coal sample containing 2 scribed channels.

4.3 Results

4.3.1 Porosity characterisation of the coals

Coal porosity changes were observed for both coals as shown in Figure 4-2a. The porosity of coal B increased from initial 8.6% to 8.9%, while the porosity of coal S rose from 4.6% to 6.1%.

In addition to the increase in total porosity, the pore size distribution (PSD) derived from MIP showed the enlargement of pores after oxidation. Figure 4-2b and Figure 4-2c show the pore size distribution for coal B and coal S, respectively, both before (dashed lines) and after (solid lines) oxidation. For coal B, the number of pores in the size ranging from 0.008 μm to 0.05 μm declined after oxidation, while the number of pores in the size range between 0.05 μm to 5 μm increased, suggesting that some smaller pores (0.008 to 0.05 μm) were enlarged due to oxidation. For pores larger than 5 μm, there was a slight increase in size. Comparatively, there was an increase in the number of pores for coal S across a larger pore size range (from 0.01 to 100 μm), with no decline of any specific pore size range after oxidation.

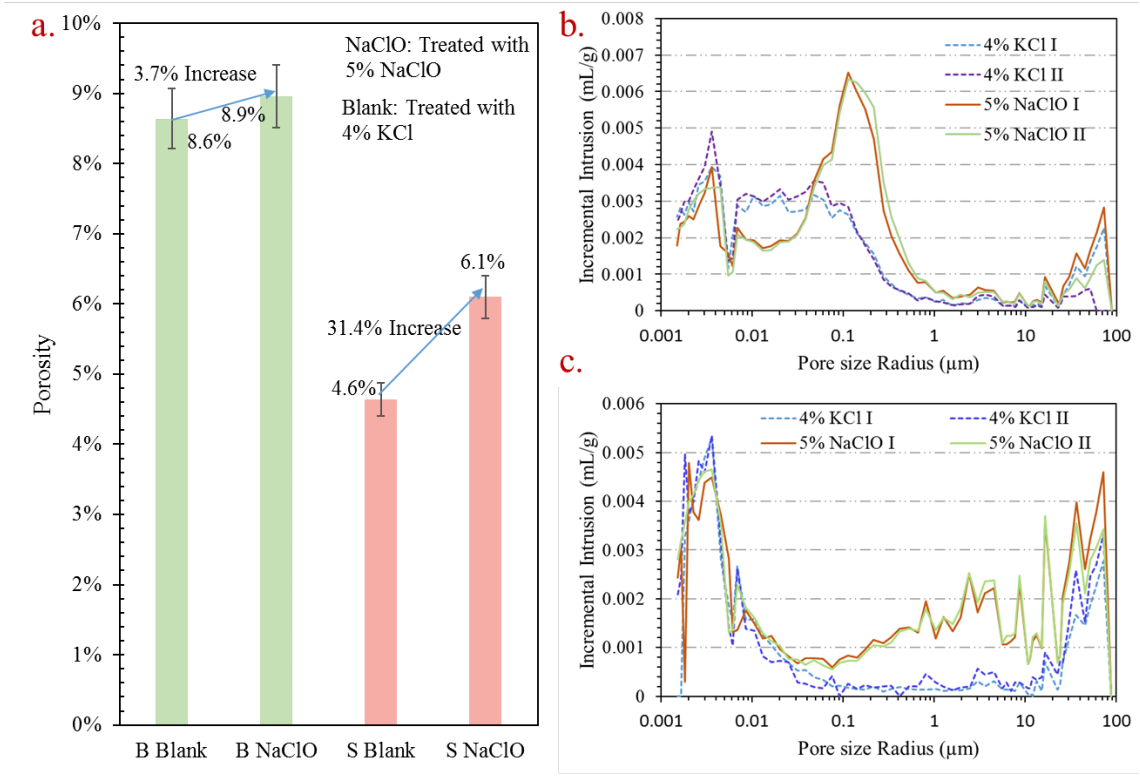

Figure 4-2: Total porosity increase (a) and PSD variation of coal B and coal S (b and c, respectively) after oxidation by 5% NaClO.

4.3.2 Scanning Electron Microscopy (SEM) and Microscope images

Comparing Figure 4-3a and b by SEM, coal B surface was generally roughened by oxidation, changing from a smooth morphology to a mottled surface but no obvious new pores or fractures. However, for coal S, a more dramatic change occurred to the surface topography (Figure 4-3c and d). Coal pores explicitly appeared after oxidation from what was a previously smooth surface. On a smaller scale, skeletal parallel structures in the top right to bottom left direction could be detected. The parallel texture evident in coal S might be related to a remnant inherent plant structure [141].

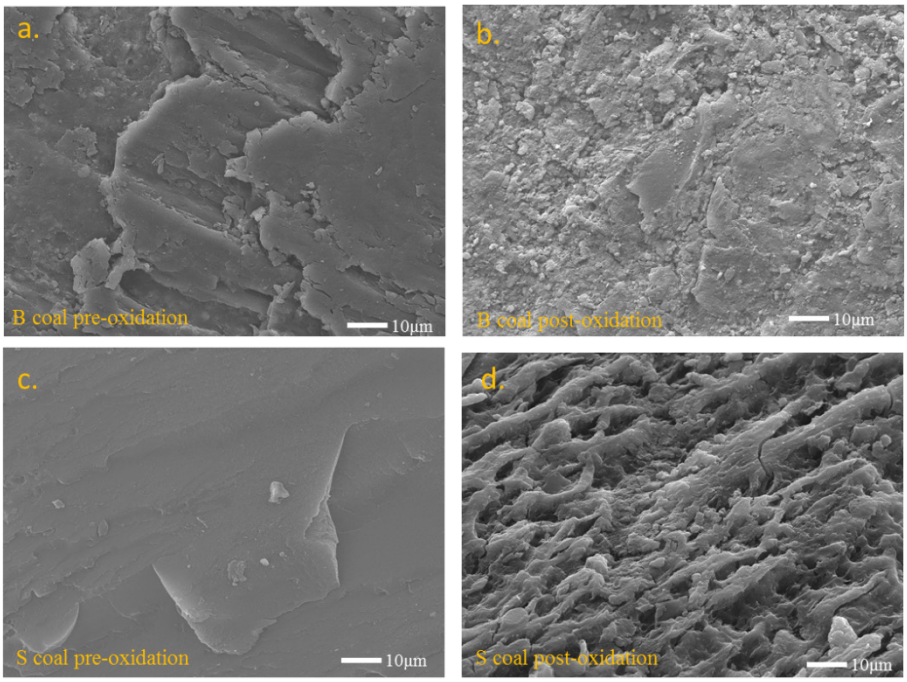

Figure 4-3: SEM images of coal B and coal S showing the surface morphology change after oxidation. a. coal B pre-oxidation; b. coal B post-oxidation; c. coal S pre-oxidation; d. coal S post-oxidation. Images were taken in secondary electrons mode.

Photomicrographs of the original/untreated samples are shown in Figure 4-4 (coal B) and Figure 4-6 (coal S). In both coals, the particle edges were sharp and well-defined before oxidation, compared with the jagged edges after treatment with 5% NaClO, as shown in Figure 4-5 (coal Bo) and Figure 4-7 (coal So). The external part of the coal was oxidised and its molecular structure was examined in the following chapter 5. The internal part of the coal particles appeared to be unchanged. Looking at various coal particles under the microscope, it was not possible to observe a preferential oxidation of a particular maceral or maceral association or even a particular particle size. It appears that the oxidant reacts where it can access the coal via surfaces, pores and inside cracks, as shown in Figure 4-7c and d that the oxidant penetrated into the fractures and reacted with the fracture surface.

The similar results can be indicated by more photomicrographs for the two studied coals before and after oxidation, which can be found in appendix from Figure 1 to Figure 4.

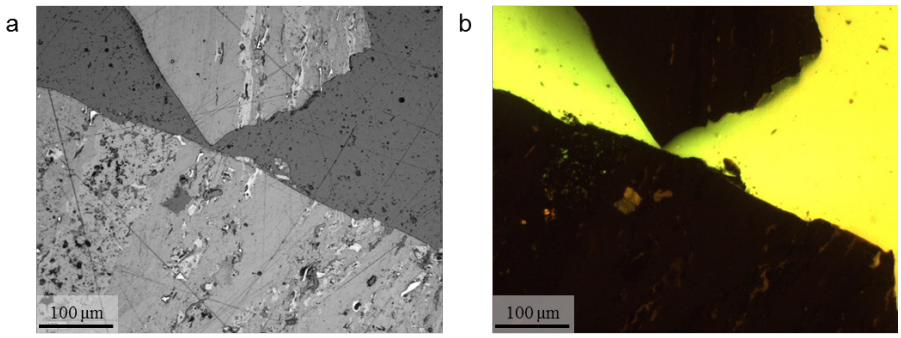

Figure 4-4. Photomicrographs coal B before treatment. (a) reflected white light; (b) fluorescent light. Images taken with air objectives (20x)

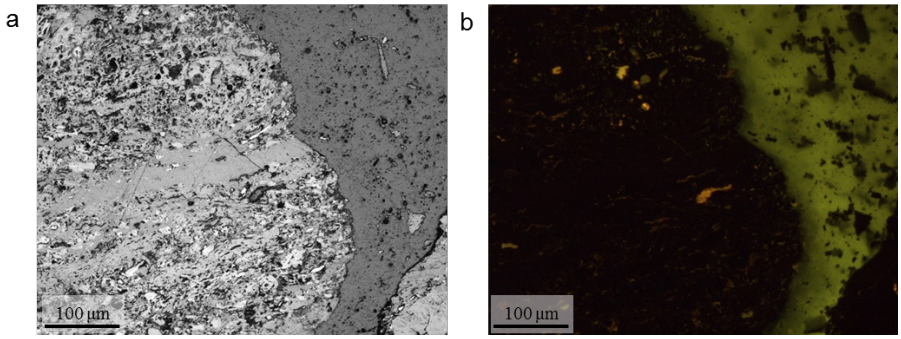

Figure 4-5. Photomicrographs for coal B after treatment. (a) reflected white light; (b) fluorescent light. Images taken with air objectives (20x)

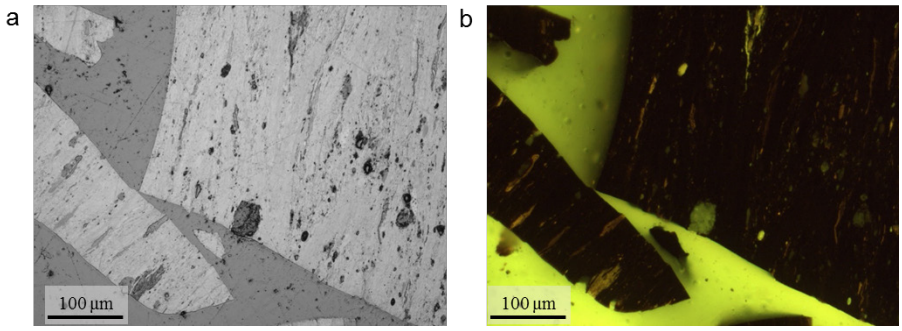

Figure 4-6. Photomicrographs for coal S before treatment. (a) reflected white light; (b) fluorescent light. Images taken with air objectives (20x)

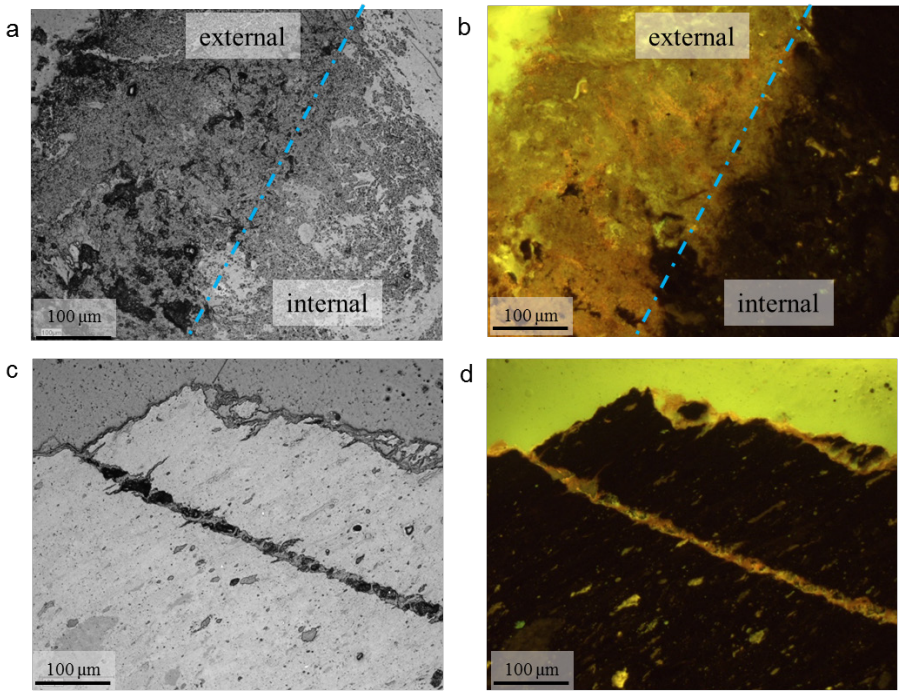

Figure 4-7. Photomicrographs for coal S after treatment. (a) particle 1 reflected white light; (b) particle 1 fluorescent light; (c) particle 2 reflected white light; (d) particle 2 fluorescent light. Images taken with air objectives (20x)

4.3.3 Cleat Flow Cell (CFC)

The artificial cleat aperture and the change of cleat shape were examined before and after coal oxidation for both coals. Firstly, to investigate the physical influence of fluid injection on channel aperture and shape, blank tests with 4% KCl were conducted prior to oxidation as shown in Figure 4-8 and Figure 4-9 for Coal B and Coal S, respectively. The photomicrographs show that the changes in both channel aperture and shape were indiscernible, regardless of maceral composition along the channel.

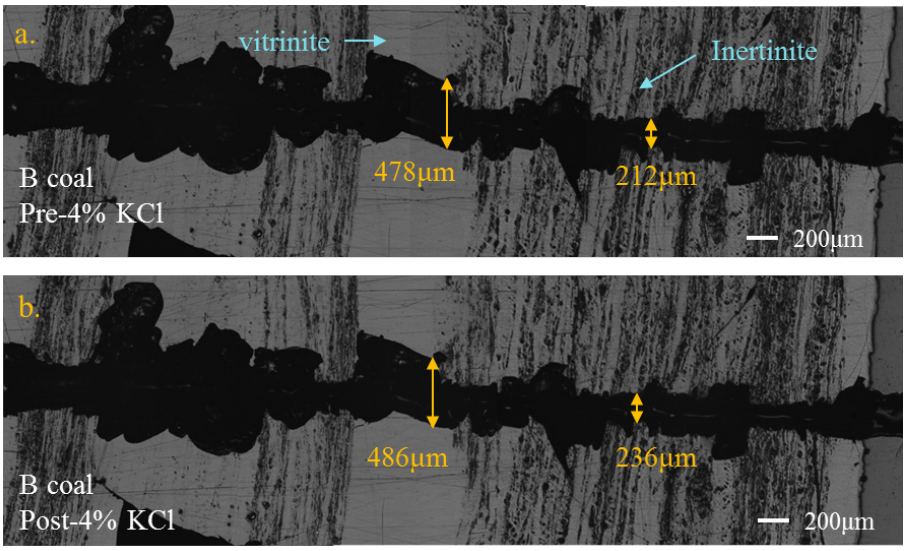

Figure 4-8: Photomicrographs of CFC blank test of coal B. a. initial channel; b. channel after 4% KCl injection.

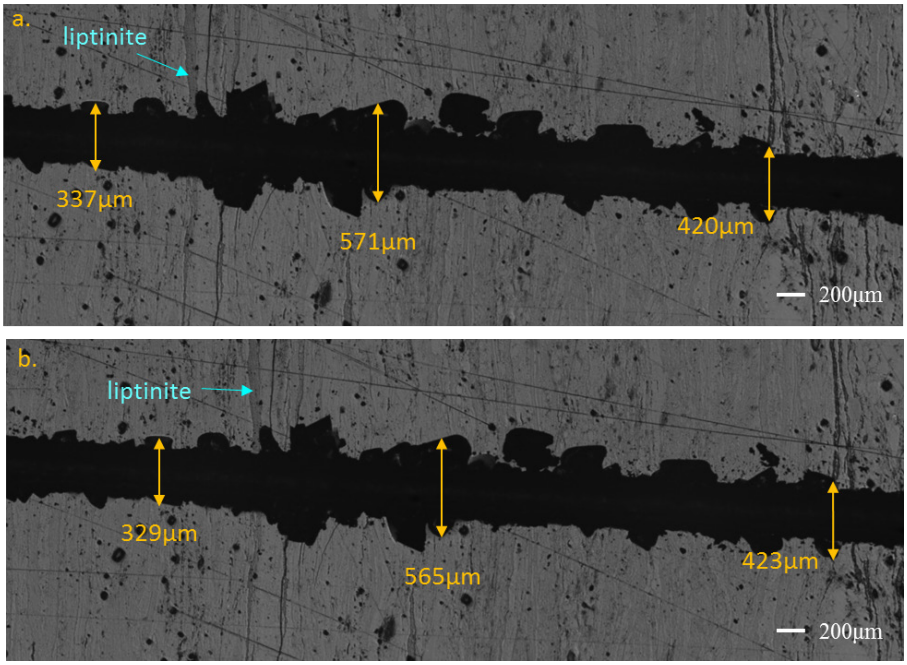

Figure 4-9. Photomicrographs of cleat flow cell blank test of Coal S (Ro %=0.47). a. initial channel; b. channel after 4% KCl injection.

After the blank test, 5% NaClO was used to flow through the channels for both coal B and coal S. Figure 4-10a and Figure 4-10b show the images zoomed to a section of channel 1 of coal B before and after 5% NaClO oxidation. The results illustrate that oxidation effect on channels varied between coal macerals. The channel aperture in the inertinite bands increased 56.8% from 322 µm to 505 µm, while the aperture in the vitrinite bands only increased 3.6% from average 631 µm to 658 µm. The channel shape also changed significantly in the inertinite bands but indiscernibly in vitrinite bands.

For channel 2 of coal B (Figure 4-11a and b), the NaClO increased the channel aperture and etched the inertinite rich area more than bright coal band. Note that the missing piece of the vitrinite shown in the dash rectangle was due to the sample handling.

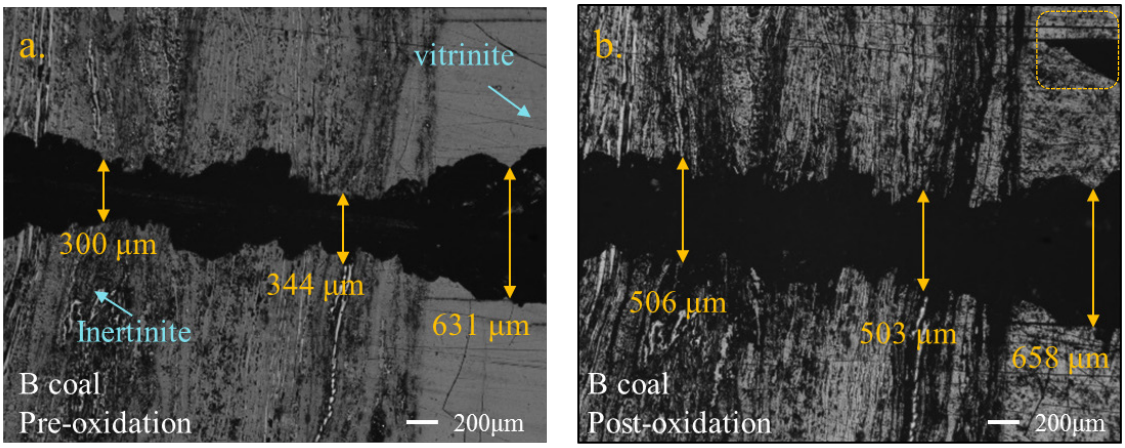

Figure 4-10: Photomicrographs of CFC test of coal B (channel 1). a. initial channel; b. channel after 5% NaClO injection.

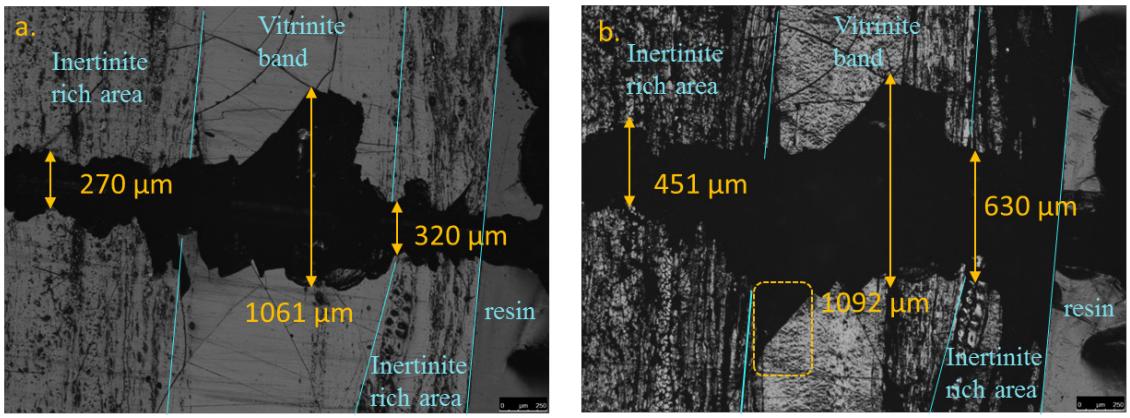

Figure 4-11. Photomicrographs of CFC test of coal B (channel 2). a. initial channel; b. channel after 5% NaClO injection.

Comparing the coal S channel post-oxidation (Figure 4-12b) with pre-oxidation (Figure 4-12a), the channel aperture increased 118% from an average width of 350 µm to 762 µm, which was much higher than that for coal B, even comparing to the inertinite bands that were more reactive. Moreover, all the initial sharp angles on the coal S channel wall were altered to result in much less roughness (Figure 4-12b). A similar result could be identified based on the examination of the aperture change for channel 2 of coal S (Figure 4-13a and b). The NaClO oxidation increased channel aperture more than twice from averagely 442 µm to 1011 µm.

Note that two new channels were also generated roughly perpendicular to the original artificial channel (Figure 4-12b). The new channel on the left followed an original fracture (Figure 4-12a), suggesting that the oxidant penetrated that original fracture. The new channel on the right was in an inertinite-rich banding. Inertinite is known to be porous [64, 142] and perhaps the oxidant has penetrated that porosity leading to enhanced reactive dissolution.

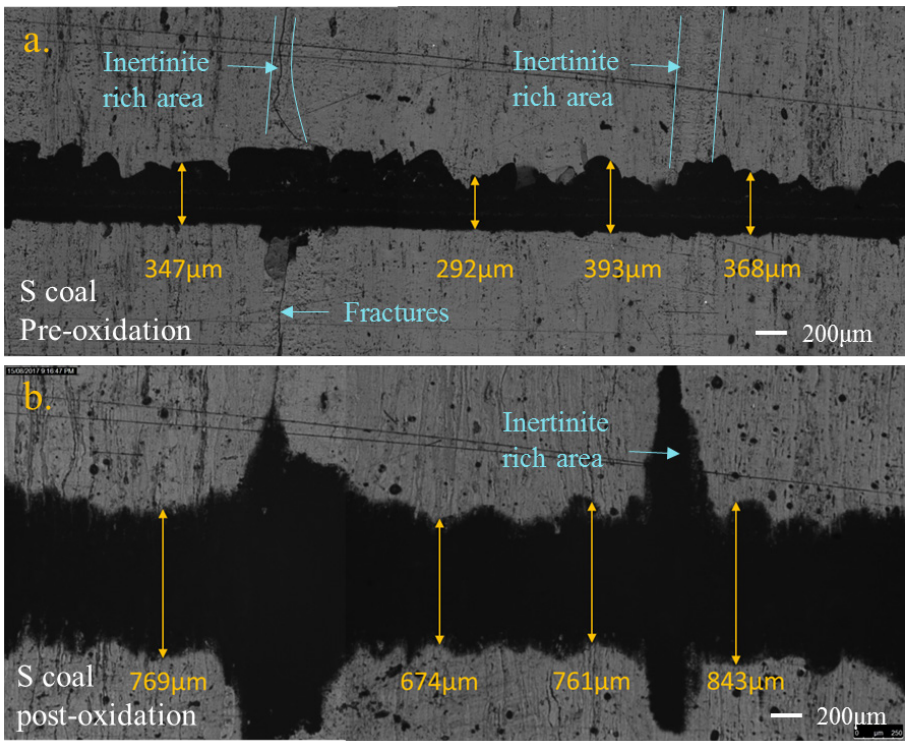

Figure 4-12: Photomicrographs of CFC test of coal S (channel 1). a initial channel; b. channel after 5% NaClO injection.

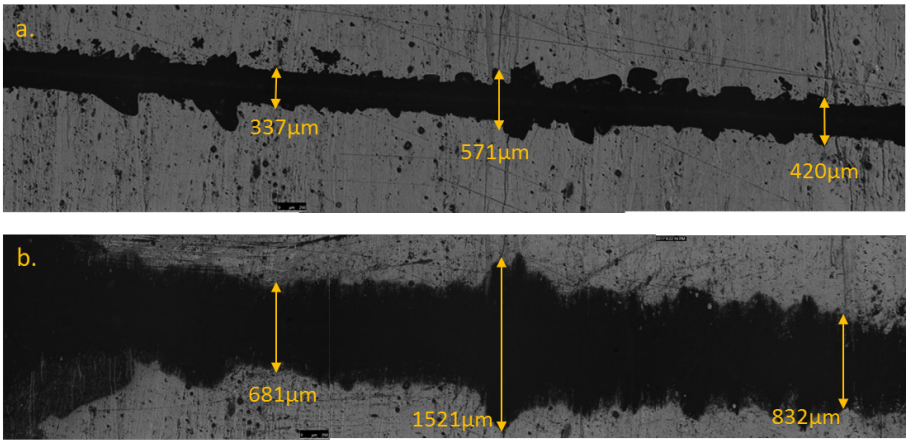

Figure 4-13. Photomicrographs of CFC test of coal S (channel 2). a initial channel; b. channel after 5% NaClO injection.

4.4 Discussion

Coal permeability is predominately controlled by the coal cleat system [2, 50, 64, 143]. Additionally, Gamson et al. (1996) found that between the gas diffusion in micropores and the laminar flow in cleat system, there existed an intermediate level for methane flow through “microstructures” in the coal matrix [138]. They defined these microstructures as micro-fractures mainly in bright coal and micro-cavities in dull coal. The existence of microstructure might advance laminar flow of gas and significantly influence gas flow in coal seams [138]. Therefore, oxidation that induces changes to coal structure may benefit both the bulk permeability by increasing cleat aperture, but also enhance the microstructural architecture of the matrix that delivers desorbed gas to the cleat, as observed in the results including the enlargement of coal pores, an increase in coal cleat aperture, and the generation of new microstructures.

From laboratory experimentation and imaging before and after oxidation, it was observed that total porosity of both coals increased after oxidation, especially coal S with total porosity increasing by 34.1%. The total porosity increase was demonstrated by the PSD change, where the coal pores were enlarged by oxidation. SEM results visualised this enlargement in pores and the generation of new pores, especially on coal S surfaces. In terms of the cleat aperture, CFC tests showed the etching of cleats resulting in increased aperture for both coals. Specifically, the channel aperture of coal B increased by 56.8% in inertinite bands and 3.6% in vitrinite bands, while it increased more than 118.0% in coal S, especially in the areas with new fractures developing perpendicular to initial channels. The generation of new channels in coal S is of particular interest. Firstly, the right channel (Figure 4-12b) occurs in an inertinite-rich (semi-fusinite) band. Secondly, the left channel (Figure 4-12b) followed an original fracture located in an intertinite-rich band. This illustrates that when the oxidant is injected into the coal seams, it might follow existing fractures and increase the fracture aperture.

Therefore, both the porosity and CFC tests showed the potential of coal oxidation to enlarge or even generate new microstructures as defined by Gamson et al. (1996) in coal to facilitate the gas diffusion in the coal matrix and enhance laminar flow in the coal cleat system [138]. Coal S appears to be more reactive than coal B. To quantify the permeability enhancement,

coal core flooding tests under *in situ* confining and fluid pressures are suggested for future research.

The change in the coal structure after oxidation appears to be due to coal swelling and dissolution. According to the coal associated and non-associated combined structure model [119], coal consists of a macromolecular structure and a mobile phase (trapped low molecular weight compounds). When the coal macromolecular structure is swollen, those trapped substances in the coal structure may be released which could provide void space in the coal structures, thus increasing the coal porosity. Additionally, NaClO could oxidise coals to generate a series of water-soluble products including benzene carboxylic acids, chloro-substituted alkanoic acids and alkanedioic acids [16, 17, 20, 21]. Coal solubilisation in NaClO was reported previously [15, 16, 122] and has been demonstrated in this research. The partial solubilisation of coal could also lead to porosity increase. The parallel structures of coal S observed by SEM is direct evidence of the partial oxidation, indicating that the oxidant preferentially reacts with certain parts of the coal. The resulting post reaction texture and morphology highlights coal heterogeneity indicative of being inherited from the original plant structure. In the early stages of coalification, the cell walls (composed by lignin-cellulose) were likely gelified within themselves without destruction of the cell tissue and humic gels precipitated in the open cell lumens. During oxidation with NaClO the humic gels may react with the oxidant agent, but the cell wall being more resistant may remain preserved (Figure 4d). Furthermore, within the Walloon Subgroup coals (coal S) the suberinite maceral is usually the main maceral of the liptinite group [144]. Suberin is a polymer containing polyesters and aromatics [145] and also ready reacts with the oxidising agent.

The NaClO oxidation preference is complex and could be affected by sample molecular structures and/or coal properties, which control the accessibility of NaClO to react with coal. In terms of the coal molecular structures, NaClO was reported to preferentially oxidize the long aliphatic side chains and some polynuclear aromatics where oxygen functional groups exist, although uncertainty still exists [15, 16, 72, 82, 122]. Coal molecular structures vary with coal rank and maceral compositions. Previous studies have found an increase in aromaticity and a loss of aliphatic and oxygen-containing structures with increasing maturation [121, 146, 147]. Additionally, a higher content of organic oxygen in lower rank coals was also reported [32, 122]. Among the maceral groups, inertinite shows the highest aromaticity, more polycondensed and structurally more ordered, while liptinite shows lower

aromaticity and longer aliphatic chains [27, 31, 148, 149]. According to the ultimate and petrographic analysis, coal B is of higher rank with abundant inertinite group macerals, whilst coal S has more liptinite and oxygen content (Table 3-2). Therefore, coal S was characterised as lower aromaticity with abundant long alkyl side chains and methylene bridges. All these characteristics demonstrate the favourability of coal S for NaClO oxidation.

Taking NaClO oxidation preference and the molecular characterisation of different maceral groups into consideration, it should be expected that the inertinite bands in coal B and coal S would be less reactive when exposed to NaClO. However, the opposite was observed (Figure 4-10b). Actually, the molecular structural similarity of inertinite and vitrinite groups in the same coal rank was reported by Niekerk et al. (2008) [27]. They found that although inertinite-rich coal was structurally more ordered and more aromatic, the general structures of both coals had similar average aromatic cluster sizes (16 carbons for vitrinite-rich and 18 carbons for inertinite-rich coals) and similar number of cluster attachments (6 attachments for vitrinite-rich and 5 attachments for inertinite-rich coals). Since the chemical-structures cannot explain the oxidative heterogeneity between inertinite and vitrinite bands in Coal B, the different pore systems in these two maceral groups might primarily affect the behaviours [27].

Since the chemical-structures cannot explain the oxidative heterogeneity between inertinite and vitrinite bands in Coal B, the different pore systems in these two maceral groups might primarily affect the behaviours. Inertinite was reported as the most porous maceral group [64, 142] and primarily composed of mesopores and macropores associated with the original plant fragments, while vitrinite-rich coal mainly contains micropores [138, 139, 142]. The surface morphology difference of the two maceral groups was also observed by SEM, where the inertinite-rich bands had a rougher texture compared to the smooth surface displayed on vitrinite-rich bands [138, 139]. The larger pores in inertinite bands are favourable for oxidant molecules to penetrate and react with coal surface. In the case of cleat-rich bright coal bands, the cleat system can also favour the oxidation process.

Further research will study the reaction between NaClO and those coal samples with different maceral compositions in the same coal rank as well as those containing similar coal maceral compositions but different ranks. This is of particular importance, because it will help to decide what oxidative method to target in future experiments or field trial.

4.5 Conclusion

NaClO was determined to be a promising oxidant for coal dissolution, particularly for subbituminous coal used in our experiments when compared to the high volatile A bituminous coal. To examine the change in coal structure after oxidation, tests including swelling and leaching tests, porosity measurement, SEM image analysis and cleat flow cell tests were conducted and the results, when integrated, demonstrate that:

1. NaClO oxidation appears to increase the coal porosity by enlarging the pore size, which was also demonstrated by SEM imaging.
2. NaClO oxidation could increase an artificial channel aperture on the natural coal surface and might be able to increase the cleat system connectivity, particularly demonstrated by the more reactive coal S sample.
3. The lower rank coal S was more reactive with NaClO than coal B according to the higher increase of coal porosity and the artificial channel aperture for coal S.
4. Higher coal S reactivity with NaClO is speculated to be due to its higher liptinite content and oxygen content.
5. Inertinite was found to be more reactive than vitrinite, which may be due to its porous structure allowing oxidant penetration.

Based on the results and discussion, Coal S permeability is expected to increase more after NaClO stimulation at *in-situ* conditions. To examine this further, core flooding tests with both coals and NaClO are recommended to measure time lapse permeability changes with the core under confining and pore pressure conditions matching typical CSG reservoir conditions. The specific effects of coal rank and maceral compositions on NaClO oxidation should be further studied on coal samples with similar maceral composition but different ranks and vice versa.

Chapter 5. Use of FTIR, XPS, NMR to characterise effects of NaClO on coal molecular structures

5.1 Introduction

In previous chapters, NaClO was reported to react more significantly with lower rank coals. This tendency has been observed by researchers who tried to generate valuable organic acids from coal through NaClO oxidation [17, 21]. The different reaction behaviours with different coal types were hypothesized to be related to key features in coal molecular structures and NaClO oxidative mechanisms [150]. Regarding coal molecular structure differences, the lower rank coals have been proposed to contain longer aliphatic side chains and more oxygen functional groups, while the higher rank coals are more aromatic with more poly-condensed structures [31, 122-124]. NaClO has been reported to preferentially oxidize side chains on the benzene rings and some aromatic rings in the presence of oxygen functional groups [15, 16, 72, 122], which might explain the more significant NaClO oxidation of lower rank coals.

These hypotheses were mainly proposed according to the study on the water-soluble oxidative products [20, 21, 82, 90], and the molecular structures of the initial coal and the oxidised residue have never been examined and compared. Besides, there remained some questions about the oxidation mechanism to be answered. For example, what is the nature of the reaction between NaClO and aromatic clusters? Does it prefer to attack the smaller aromatic rings or dissolve them at all? What are the oxidation products for the coal residue? If NaClO prefers to oxidise the aliphatic chains, will the coal residue become more aromatic

or aliphatic? To clarify these uncertainties, this study examined the molecular structure of two coal samples from the Bowen (coal B) and Surat (coal S) basins in Queensland, Australia, and their oxidised coal residues (coal So and coal Bo), using Fourier transform infrared spectroscopy (FTIR), X-ray photoelectron spectroscopy (XPS) and solid state ^{13}C nuclear magnetic resonance spectroscopy (NMR). Previous research has widely reported how these methods work in coal-related areas as well as their advantages and limitations [31, 32, 111, 148, 151-164]. These techniques have enabled an improved fundamental understanding of coal molecular chemical structure. When used in combination, these methods can be more informative than when used alone and can also be used as a means of checking consistency [32]. For instance, Vega et al. (2017) used FTIR combined with XPS to examine the effect of oxygen oxidation on the surface chemistry of bituminous coals and they found that the lowest rank coals were the most affected [165]. Okolo et al. (2015) combined ATR-FTIR and solid state ^{13}C NMR to analyse the chemical-structure of South African bituminous coals [32].

In this chapter, the chemical structural properties of two coals before and after oxidation were measured and compared with ATR-FTIR, XPS and solid state ^{13}C, to gain improved understanding of coal reactive dissolution mechanisms using oxidants. Knowledge gained can then be used to more effectively predict the chemical interactions between coal and various oxidants with a view to increase coal seam permeability for enhancing gas productivity in the coal seam gas industry.

5.2 Methodology

5.2.1 ATR-FTIR

ATR-FTIR measurements were performed using Perkin Elmer Spectrum 100 equipped with an Attenuated Total Reflectance. The samples were analysed at ambient temperature, from

a collection of 32 scans per spectrum (interferograms), at a resolution of 4 cm^{-1} in the frequency range of 4000–650 cm^{-1}. In order to observe the reproducibility of FTIR spectra, two spectra were measured for each sample. ATR-FTIR spectra show good reproducible with regard to peak locations and intensities of individual bands. The qualitative analyses of the spectra and peak assignments followed the procedures described previously [27, 31, 151, 157, 166].

There has been some success in obtaining semi-quantitative data from FTIR spectra [31, 111, 121, 148, 167]. To obtain the semi-quantitative data for further analysis, the Origin-Pro program was used for spectral de-convolution, curve-fitting, and determination of peak integration areas. Deconvolution is the best method for analyzing positions of the absorption peaks. Peak fitting can quantify the contents of each absorption peak in the overlapping area. ATR-FTIR spectra were subject to Kramers–Kronig transformation. For each FTIR spectrum, the selected regions were baseline-linearized before curve-fitting [31, 121, 166, 168]. However, the region close to 1600 cm^{-1} is not suitable for the quantitative study of aromatic groups [154].

5.2.2 XPS

XPS data was acquired using a Kratos Axis ULTRA X-ray Photoelectron Spectrometer incorporating a 165mm hemispherical electron energy analyser. The incident radiation was Monochromatic Al Kα X-rays (1486.6eV) at 150W (15kV, 10ma). Survey (wide) scans were taken at an analyser pass energy of 160eV and multiplex (narrow) high resolution scans at 20eV. Survey scans were carried out over 1200-0eV binding energy range with 1.0eV steps and a dwell time of 100ms. Narrow high-resolution scans were run with 0.05ev steps and 250ms dwell time.

Base pressure in the analysis chamber was 1.0x10-9 torr and during sample analysis is was 1.0x10-8 torr. Atomic concentrations were calculated using the CasaXPS version 2.3.14 software and a Shirley baseline with Kratos library Relative Sensitivity Factors (RSFs). Peak fitting of the high-resolution data was also carried out using the CasaXPS software.

5.2.3 Solid state ^{13}C NMR

The solid state ^{13}C NMR spectra were acquired from a 300 MHz Bruker Avance III spectrometer using 4 mm zirconia rotors spinning at 7kHz, using a combination of cross polarization magic angle spinning (CPMAS) and dipolar dephasing magic angle spinning (DD–MAS) methods. CPMAS method is the most used practice in ^{13}C NMR for the attainment of a well-resolved spectrum after in a moderate time for organic materials [169]. The experiments were conducted at ambient temperature with 100 kHz proton decoupling using a recycle delay of 3s. The contact time for cross-polarization was 2.0 ms. A total of 4000 scans per spectrum were collected for an acceptable signal to noise ratio. The contact time, which provided suitable peak intensity for semi-quantitative analysis, was chosen based on the results of variable contact time experiments.

The coal samples' structural parameters were determined from the integral values of ^{13}C NMR spectra, while the lattice parameters were calculated, according to the methods proposed by Solum and co-workers [32].

There are limitations in the quantitative reliability of CP/MAS spectra: this technique is intrinsically not quantitative unless the signal intensity is carefully calibrated with standards where composition, dipolar coupling constant, relaxation times in a rotating frame, and molecular structures are well known. Notwithstanding, it has been shown that the technique can be used to compare intensity distributions among similar samples [170]. To ascertain

the CPMAS spectra quality, single pulse with high power decoupling spectra were recorded as well for some samples, and the results were almost identical. The CP-MAS in combination with DD–MAS is widely used for coal characterisations. The DD–MAS experiment is used to distinguish strongly proton-coupled carbons from weakly coupled or non-protonated carbons. The DD technique is based on the principle that in the absence of ^{1}H decoupling, strongly ^{1}H coupled carbons will dephase much faster than weakly coupled carbons [16]. As a result, a DD–MAS spectrum is measured with long dephasing delays (45 μs) dominated by signals of non-protonated or weakly coupled carbons. The DD–MAS method, therefore, allows the observation of weakly coupled carbons present in bridgehead aromatics, which allows for the calculation of a number of structural parameters unobtainable by the CPMAS technique alone.

5.3 Results

5.3.1 Leaching test

Figure 5-1 shows the mass loss of coal S and coal B in the NaClO sequential oxidation. In the first contact with 5% NaClO, coal S lost 45.2% mass, while coal B lost only 4.5%. In the second leaching test, coal S mass dropped a further 32.2% and coal B lost 42.5% mass. This shows the influence of kinetics on oxidation. In total, the mass loss for coal S and coal B were 77.4% and 47.0%, respectively.

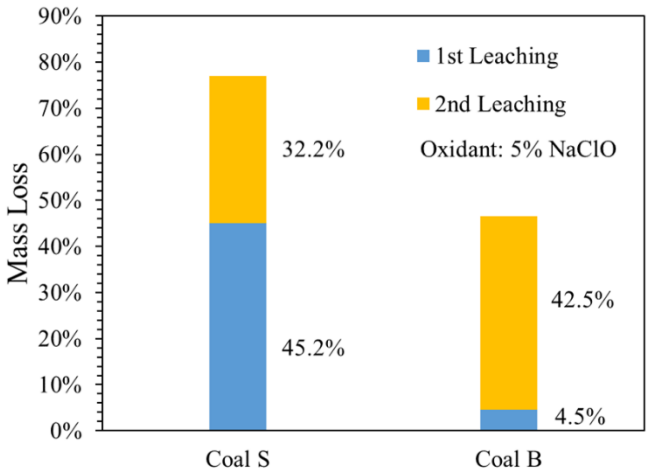

Figure 5-1. Mass loss of coal S and coal B after 2 steps oxidation in 5% NaClO

5.3.2 ATR-FTIR

The ATR–FTIR spectra of the studied coal samples exhibited well-resolved peaks and bands, and flat baselines (Figure 5-2) making them suitable for further qualitative analysis. The qualitative interpretation of FTIR spectra was based on previous work [27, 31, 32, 111, 121, 148, 155, 171-173] and is summarized in Appendix Table 1.

The bands at 3100-3000 cm^{-1} and 3000 - 2800 cm^{-1} could be assigned to aromatic CH stretching vibrations and aliphatic CH stretching vibrations, respectively (Appendix Table 1). As shown in Figure 5-2, the peak between 3100-3000 cm^{-1} was indiscernible for coal S but present for coal B, while the peak between 3000 - 2800 cm^{-1} was more intense for coal S than coal B. These different peak intensities indicate the relatively abundance of aliphatic carbon in coal S and aromatic carbon in coal B. The prevalence of aromatic carbon in coal B was further demonstrated by the relatively higher intensity of the peak at 1600 cm^{-1}, which was assigned to the C=C stretching vibrations of aromatic rings [27, 173, 174].

After oxidation, the absorbance intensity of either aliphatic or aromatic C-C or C-H bonds in coal S did not change significantly, although a slight decrease in the 1600 cm^{-1} peak (C=C) could be observed. By comparison, the oxidation of coal B caused an obvious decrease in the 3100-3000 cm^{-1} region (aromatic CH stretching).

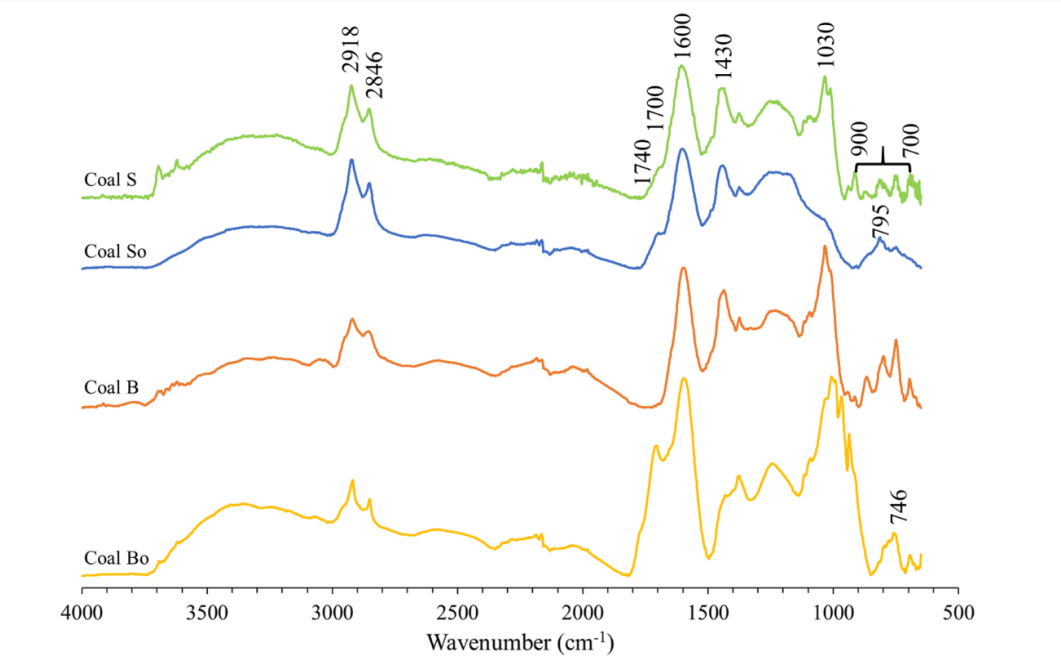

Figure 5-2. ATR-FTIR spectra for coal S and coal B before and after oxidation.

Moreover, a shoulder at the left-hand side of the 1600 cm−1 peak can be ascribed to aromatic C=O stretching (1700 cm-1), and the band within 1300-1100 cm−1 can be ascribed to aromatic C-O stretching vibration [153, 168, 172]. The aliphatic C=O and aliphatic C-O bonds could be assigned to absorbance bands between 1740-1730 cm−1 and 1100-1000 cm−1, respectively [153, 167, 175].

The absorbance intensity of both aromatic C=O and aromatic C-O bands were higher in unreacted coal S than those in coal B, implying that coal S had relatively more chemical species with oxygen atoms bonded to aromatic carbons such as phenolic groups, esters, ketones, aldehyde or –COOH, or a combination of these groups [27].

NaClO oxidation caused significant difference in oxygen bonded structures in coals, especially for coal B. At the peak of 1700 cm^{-1}, both coals showed higher intensity after oxidation and coal Bo particularly exhibited an intensive peak, while it was totally absent in coal B. The aliphatic C-O (1100-1000 cm^{-1}) disappeared for coal So.

Despite the difficulty to estimate absolute content of functional groups in the coals by FTIR [154, 155], the band integral area ratios are still valuable for evaluating the molecular structure of organic matter in coal semi-quantitatively [31, 111, 148, 151, 155-157]. Although many indexes derived from FTIR spectra have been successfully used [31, 148, 167, 168], only the following more intense and stable absorbance peak or area ratios (Table 5-1) were used here. More detailed reasons for selecting these peak ratios have been discussed elsewhere [154].

The CH_2/CH_3 (2920 cm^{-1}/2950 cm^{-1}) ratio, obtained by curve deconvolution, can be used to estimate the length and degree of branching in aliphatic side chains [31]. The curve deconvolution for the aliphatic C-H stretching vibration for coal S, coal So, coal B and coal Bo are shown in Appendix Figure 5, Appendix Figure 6, Appendix Figure 7 and Appendix Figure 8, respectively. The area of the de-convoluted peaks and the CH_2/CH_3 ratios for the studied coals are summarized in Table 5-1. With the aliphatic chains becoming longer or less branched, the CH_2/CH_3 ratio should increase [168, 171]. The values of CH_2/CH_3 ratio of coal S and coal B were 2.56 and 0.75, respectively, demonstrating longer aliphatic chains for coal S than coal B. After oxidation the CH_2/CH_3 ratio increased to 3.59 and 0.95 for coal So and coal Bo, respectively.

The integrated areas of H_{ar} (3100–3000 cm^{-1}) and H_{al} (3000–2800 cm^{-1}) have been used to estimate the concentration of aromatic and aliphatic carbons, respectively [155]. The H_{ar}/H_{al} ratio could indicate the aromaticity of the coal sample structures [31, 154] and the results are summarized in Table 5-1. The H_{ar}/H_{al} ratios for coal S and coal B were 0.07 and 0.10, respectively. The oxidation decreased the ratio to 0.03 and 0.08, for coal So and coal Bo, respectively.

Table 5-1 . Integrated areas of asymmetric CH_3 and asymmetric CH_2 peaks, aromatic and aliphatic carbon band and Infrared indexes.

Coal Samples	Wave Number (cm^{-1})				IR indexes	
	2950	2920	3100-3000	3000-2800	CH_2/CH_3	H_{ar}/H_{al}
Coal S	0.1624	0.4164	0.0565	0.8071	2.56	0.07
Coal So	0.0943	0.3390	0.0269	0.9322	3.59	0.03
Coal B	0.1283	0.0963	0.0658	0.6641	0.75	0.10
Coal Bo	0.1701	0.1617	0.0583	0.6251	0.95	0.08

2950 cm^{-1}: asymmetric CH_3; 2920 cm^{-1}: asymmetric CH_2; H_{ar}: integrated area of 3100-3000 cm^{-1}; H_{al}: integrated area of 3000-2800 cm^{-1}.

5.3.3 XPS

In order to quantify the oxygenated carbons, high resolution XPS spectra of C 1s were de-convoluted using Gaussian-Lorentzian peaks [159, 160, 162, 165]. Appendix Figure 9 and Appendix Figure 10 show the XPS wide energy spectrum of the sample surface for coal S and coal B before and after oxidation, respectively. Coal S was found to have more oxygen, at 22.90% than coal B, 12.67%. After oxidation, the oxygen content increased for both coals to 26.37% for coal So and to 18.94% for coal Bo, respectively, accompanied by a decrease in carbon content.

Figure 5-3 and Figure 5-4 show the high resolution XPS spectra of C 1s for coal S and coal B before and after oxidation, respectively. Peaks at binding energies of 284.6 eV, 285.7 eV, 287.0 eV, and 288.5 eV correspond to the following groups: C-C or C-H, C-O (alcohol, phenol or ether), C=O (carbonyl) or O-C-O (in low rank coals) and COOH (carboxyl) [159, 160, 162].

Deconvolution of the spectra is also shown in Figure 5-3a and Figure 5-4a, where a clear carboxyl peak is present for coal S but absent for coal B. Specifically, coal S contained 38.90% total oxygen-carbon groups including 24.51% C-O group, 9.08% C=O group and 5.31% O-C=O group, while coal B only had 22.63% C-O group. These results were expected since hydroxyl and carboxyl oxygen are abundant in lower rank coals [27, 157, 160, 162], and corresponded to the results obtained by ATR-FTIR. The contents of C-C or C-H were 61.10% and 77.37% for coal S and coal B, respectively.

Comparing the XPS results of each coal before and after oxidation, the dominant difference was the decrease in the proportion of C-C and C-H bonds and an increase in oxygen bonded structures, especially the carbonyl or carboxyl groups. For coal S, oxidation decreased the C-C or C-H proportion from 61.10% to 55.32%, and raised the oxygen bonded carbons from 39.90% to 44.78%. Interestingly, the proportion of C-O decreased, while the proportion of C=O or O-C=O bonds increased.

A comparable situation occurred for coal B. The C-C or C-H proportion dropped from 77.37% to 69.71%, while the oxygen contained structure proportion increased from initial 22.63% to 30.29% after oxidation. Additionally, the decrease of the C-O was also accompanied by the increase of C=O and O-C=O.

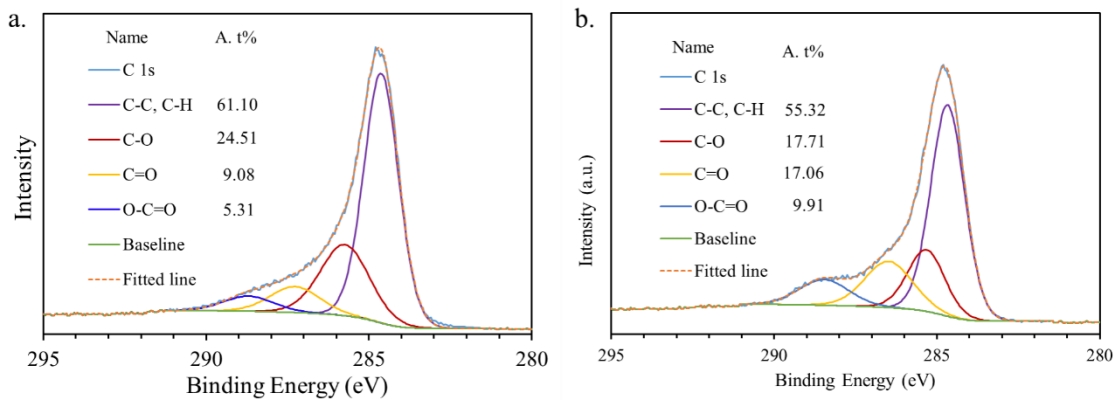

Figure 5-3. XPS results of coal S (a) and coal So (b). A.t% - Area %

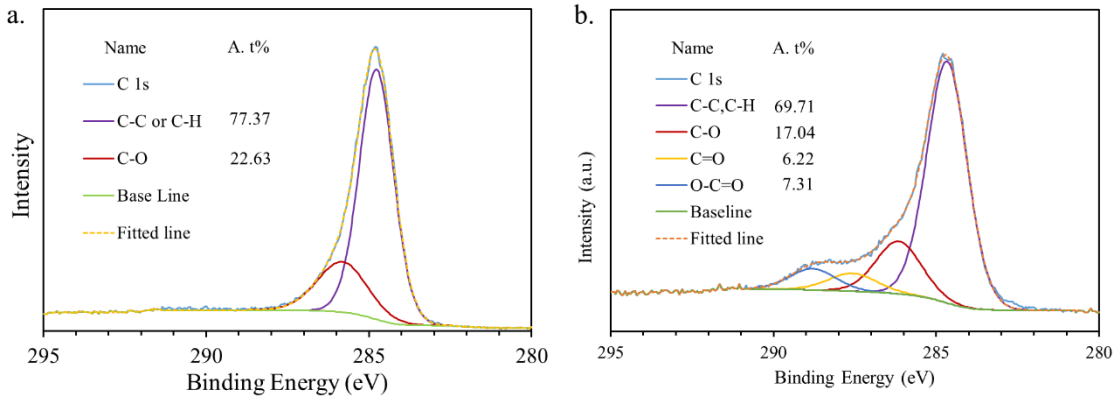

Figure 5-4. XPS results for coal B (a) and coal Bo (b). A.t% - Area %

5.3.4 ^{13}C NMR

^{13}C NMR has been widely applied in the study of carbon structures in coal and oil shale both qualitatively and quantitatively [32, 163, 164, 176]. In this work, ^{13}C NMR was used to analyse the coal molecular structures and calculate various structural parameters defined by Solumn et al. (1989, 2001) [163, 176] .

5.3.4.1 Molecular structure comparison between coal S and coal B

Figure 5-5 and Figure 5-6 show the ^{13}C NMR spectra of the two studied coal samples before and after oxidation. All the samples exhibited two distinct ranges: an aliphatic range (0–60

ppm) and an aromatic region (100 to 200 ppm) [32, 177]. The aliphatic peak range had larger area than the aromatic peak range for coal S (Figure 5-5a), while the opposite result presented for the NMR spectrum of coal B (Figure 5-6a).

In the aliphatic carbon region, an intense peak at 30 ppm for coal S (Figure 5-5a) originated from methylene carbons (CH_2) in aliphatic chains, and its right shoulder at 20 ppm was assigned to terminal methyl groups (CH_3) [164, 170]. The low intensity of methyl groups (20 ppm) relative to the signal of methylene carbons (30 ppm) indicated the presence of long chain aliphatic structures in coals [170]. However, the intensity of these two peaks were similar in coal B (Figure 5-6a), implying that the aliphatic chains in coal B were more branched and/or shorter than that in coal S. Additionally, the peak assigned to aliphatic alcohol and ether carbon (60-90 ppm) [170] exhibited on the NMR spectrum of coal S but was indiscernible for coal B, indicating higher content of aliphatic C-O groups for coal S than coal B.

In the aromatic carbon region, a peak at 125 ppm was assigned to protonated aromatic carbon [170], while a peak at 153 ppm showed the chemical shift of a monohydric phenolic carbon [163, 170]. They were observed for both coal S and coal B. However, the carbonyl carbon assigned to the peak at the range of 165-190 ppm [163, 170, 177, 178] only showed at the spectrum for coal S, but was absent for coal B.

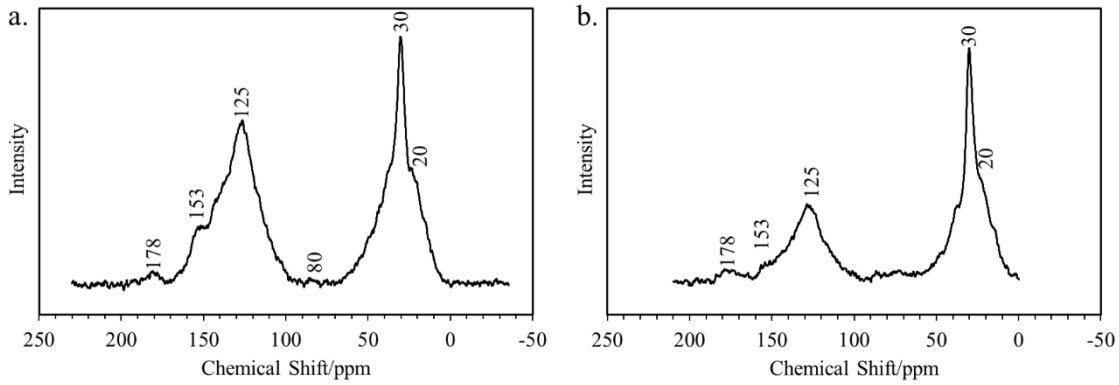

Figure 5-5. ^{13}C CP–MAS NMR spectra of coal S (a) and coal So (b).

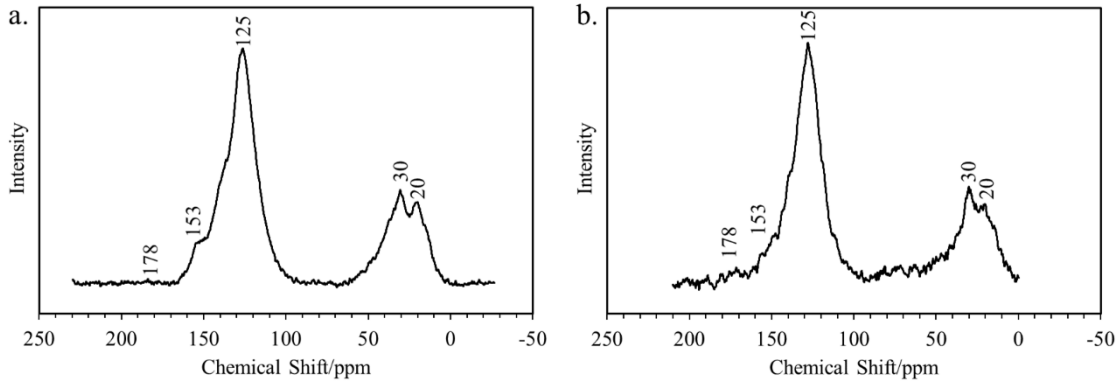

Figure 5-6. ^{13}C CP-MAS NMR spectra of coal B (a) and coal Bo (b).

The structural parameters and lattice data for the studied coal samples were calculated based on the research by Solum and co-authors [163, 176] and are summarized in Table 5-2. Structure parameters f_a and f_{al} show the fraction of aromatic carbon and aliphatic carbon, respectively. Coal S contained 53% aromatic carbon, while coal B had 70% aromatic carbon. The less aromaticity of coal S than coal B agreed well with the observation on the NMR spectra.

Furthermore, the mole fraction of aromatic bridgehead carbon in total carbon (f_a^B) and mole fraction of aromatic bridgehead carbon in aromatic carbon (x_b) are two indicators to characterize the number of condensed aromatic rings in coal [177]. f_a^B for coal S and coal B

were 0.08 and 0.25, respectively, while x_b for coal S and coal B were 0.16 and 0.36, respectively. The comparison of these two parameters showed that coal S was less poly-condensed than coal B. The lower fraction of bridgehead carbon for coal S also determined a smaller average cluster size (C) and less average molecular weight of aromatic clusters (M.W.). Specifically, an average of 9 carbons were composed of one aromatic cluster for coal S, while its counterpart for coal B was 17. Average molecular weights for coal S and coal B were 271.72 and 341.54, respectively.

In terms of the oxygen functional groups in coal structures, the parametersf_a^c, f_a^o, $f_a^{oo}$and f_a^p demonstrated the oxygen bonded to aromatic carbons in different forms, while f_a^o showed the aliphatic oxygen functional groups. Specifically, the parameterf_a^c, assigned from 165 to 190 ppm on the ^{13}C NMR spectra represents the aromatic oxygen atoms in carbonyl (f_a^o) and carboxyl functional groups (f_a^{oo}), and f_a^p indicates the fraction of phenols or phenolic ethers. For coal S, f_a^{oo} and f_a^p were 0.04 and 0.02, agreed with the NMR spectral peaks at 178ppm and 153ppm, respectively. Additionally, coal S also contained 4% aliphatic oxygen, which was also manifested by the signal between 60 – 90 ppm on the NMR spectrum for coal S (Figure 5-5a). By comparison, coal B contained fewer oxygen in both the aromatic structure (1% phenolic oxygen) and aliphatic structure (1%).

The structure and lattice parameters f_a^s, σ+1 and P_0 provided information related to attachments [164, 178]. While f_a^s represents alkylated aromatic carbons with a carbon chain attached, σ+1 illustrated the attachments per aromatic cluster, including both the alkylated aromatic carbons (f_a^s) and phenolic aromatic carbons (f_a^p). The attachments contain aliphatic side chains terminating in methyl groups (chains), connections between two different clusters (bridges) and connections back to the same cluster (loops) [164, 178]. Among the attachments, P_0 showed specifically, the number of intact bridges. The values of

f_a^S and σ+1 for coal S were 0.07 and 1.94, respectively. Their counterparts for coal B were 0.10 and 2.91, respectively. The relatively lower values of f_a^S and σ+1 for coal S indicated it contains less attachments per cluster. Both coal S and coal B had negative P_0 values, showing significant branching in the aliphatic chains with multiple methyl groups on a single chain [164, 176].

The average aliphatic carbon chain length depicted previously using FTIR in section 3.3, could also be determined using ^{13}C NMR, by dividing the percentage of aliphatic carbon by the percentage of alkyl substituted aromatics (f_{al}/f_a^S). This term does not necessarily imply the presence of straight or branched aliphatic chains of specific length. Naphthenic and other aliphatic structures contribute to the NMR parameter f_{al} and thus could also influence the NMR parameter for the average aliphatic chain length [161]. According to the calculated f_{al}/f_a^S values, aliphatic chains for coal S (6.71) were longer than that for coal B (3.00) as shown in Table 5-2.

Table 5-2. Solid state ^{13}C NMR structural and derived lattice parameters of the studied coal samples.

Coal	Structural Parameters													
	f_a	f_a^C	f_a^O	f_a^{OO}	$f_{a'}$	f_a^H	f_a^N	f_a^P	f_a^S	f_a^B	f_{al}	f_{al}^H	f_{al}^*	f_{al}^O
S	0.53	0.02	0.00	0.02	0.51	0.32	0.19	0.04	0.07	0.08	0.47	0.35	0.12	0.04
So	0.37	0.03	0.00	0.03	0.34	0.09	0.25	0.02	0.06	0.17	0.63	0.45	0.18	0.05
B	0.70	0.00	0.00	0.00	0.70	0.33	0.37	0.02	0.10	0.25	0.30	0.16	0.14	0.01
Bo	0.67	0.01	0.00	0.01	0.66	0.46	0.20	0.03	0.07	0.10	0.33	0.21	0.12	0.06

Coal	Lattice Parameters					
	x_b	C	σ+1	P_0	M.W.	f_{al}/f_a^S
S	0.16	9	1.94	-0.09	271.72	6.71
So	0.50	24	5.65	-1.25	1569.93	10.50
B	0.36	17	2.91	-0.17	341.54	3.00
Bo	0.15	9	1.36	-0.20	250.43	4.71

Structure parameters: f_a -fraction of aromatic carbon atoms (sp^2 hybridized); f_a^c-carbonyl/carboxyl carbon; f_a^o-aldehyde and ketone fraction; f_a^{oo}-acid or ester fraction; $f_{a'}$-aromatic carbons, excluding f_a^c; f_a^H-protonated aromatic carbons; f_a^N-nonprotonated aromatic carbons; f_a^p-phenols or phenolic ethers; f_a^s - alkylated aromatic carbons with a carbon chain attached; f_a^B - aromatic bridgehead carbons; f_{al} - total aliphatic carbon (sp^3 Hydridized); f_{al}^H - CH or CH_2; f_{al}^* -methyl and methoxy groups; f_{al}^o - aliphatic carbon and bonded to an oxygen.

Lattice parameters: x_b -mole fraction of aromatic bridgehead carbons; C-average number of aromatic carbon atoms per cluster; M.W.-average molecular weight of the aromatic cluster; σ+1-average number of attachments (bridges, loops and side chains) per cluster; P_0- number of bridges that are intact; f_{al}/f_a^s -average aliphatic chain length.

5.3.4.2 Structural comparison of coal samples before and after oxidation

The comparison of the NMR spectra for each sample before and after oxidation could obtain valuable clues indicting the structure change caused by oxidation. Two peaks, assigned to aliphatic carbons and aromatic carbons, clearly exhibited in the NMR spectra for coal So (Figure 5-5b), however the aromatic peak (100-200 ppm) decreased significantly relative to the aliphatic peak compared to coal S (Figure 5-5a), indicating the oxidation of coal S led to a more aliphatic structure.

For coal B, the change of the relative proportion of aromaticity was minor (Figure 5-6a and Figure 5-6b). However, the variation on oxygen was clear. The oxygen bonded to both aliphatic carbon (60-90 ppm) and aromatic carbon (165-200 ppm) apparently increased after oxidation.

The structural parameters and lattice data reflected that the oxidation of coal had caused significant change on coal molecular structures. Compared with the initial coals, the oxidised coals were characterised by NMR as lower aromaticity, higher oxygen contents, and longer aliphatic chains, regardless of the coal types. The aromaticity (f_a) for coal S decreased from 0.53 to 0.37, while its counterpart for coal B experienced a relative slighter drop from 0.70 to 0.67. Accordingly, the aliphaticity increased from 0.47 to 0.63 for coal S and from 0.30 to 0.33 for coal B, respectively. In terms of the oxygen, coal So contained generally similar aromatic oxygen (f_a^{oo}=0.03, f_a^p =0.02) and marginally higher aliphatic oxygen (f_a^o = 0.05) than coal S, while coal Bo possessed explicitly higher oxygen content in all forms, especially aliphatic oxygen (f_a^o = 0.06). Both coal So and coal Bo had longer aliphatic chains indicated by f_{al}/f_a^s (10.50 and 4.71, respectively) than their parent coals.

However, the coal types affect the average coal molecular cluster size variation caused by oxidation. For coal S, more bridgehead carbons (f_a^B =0.17) appeared in the structure associated with larger average cluster size (C=24) after oxidation. By comparison, coal Bo had lower proportion of bridgehead carbons (f_a^B =0.10) and accordingly, smaller aromatic cluster size (C=9). The difference of the aromatic cluster size change between the two studied coals might result from their initial different structures and will be discussed in the next section.

5.4 Discussion

The results obtained by FTIR, XPS and solid state ^{13}C NMR were used to reveal different molecular structures of the sub-bituminous (coal S) and bituminous (coal B) coals as well as their oxidised samples, coal So and coal Bo. When used in combination, they could provide more comprehensive information and also be used to check the interpretive results for consistency.

5.4.1 Molecular structures of different coal types

The most obvious and best identified structural characteristics of the pre-treatment coals are that coal S appears to be more aliphatic, while the higher rank coal B is more aromatic. These characteristics were unravelled comprehensively by FTIR and NMR.

The FTIR spectrum of coal S exhibited higher aliphatic carbon, while coal B showed stronger intensity in aromatic carbons. Also, the H_{ar}/H_{al} ratio indicated that the aromaticity is lower for coal S than coal B. The prevalence of higher aromaticity for higher rank coals has been previously demonstrated by Okolo et al. (2015) with FTIR results [32].

^{13}C NMR spectra and a series of derived parameters confirmed the results by FTIR where coal S manifested a higher intensity in the aliphatic region, while coal B had a higher peak in the aromatic region. Moreover, this was later quantified by the ^{13}C NMR structure parameters that coal S contained 47% aliphatic carbon, while coal B only had 30%.

Furthermore, ^{13}C NMR lattice parameters showed more skeleton information about the coal structures by comparing x_b and C of the studied coal samples with those organic components having clear molecular structures. Appendix Figure 11 illustrates the relationship between the number of aromatic rings and x_b. The x_b of benzene and naphthalene are 0 and 0.2, respectively, [177] and their C parameters (average number of

carbons per cluster) are 6 and 10, respectively. By comparison, the x_b and C for coal S were 0.16 and 9, which are between the corresponding parameters for benzene and naphthalene. It could be inferred that benzene and/or naphthalene are the main aromatic structures in coal S. The x_b of aromatic components with 3 aromatic rings (Anthracene and Phenanathrene) and 4 aromatic rings (cherysene, Triphenylene, and Pyrene) range from 0.286 to 0.375 (Appendix Figure 11) and the x_b of Picene (five benzene rings in liner catenation) is 0.364. The average x_b for coal B was 0.36, indicating that coal B might contain aromatic clusters with at least 4 benzene rings. This is supported by the average cluster size (C=17) for coal B that was also in the range of Anthracene (14) and Chrysene (18).

In terms of the aromatic oxygen, ATR-FTIR spectra showed coal S had more intensive adsorption of aromatic C=O and aromatic C-O than coal B. This corresponded to the ^{13}C NMR results, which showed that coal S contained higher proportion of carboxyl groups and phenolic groups than coal B. Concurrently, the deconvolution of XPS complemented the oxygen analysis showing coal S contained C-O (24.51%), C=O (9.08%) and O-C=O (5.31%) groups, while coal B had only C-O groups (22.63%) in their molecular structures. Therefore, coal S is proposed to contain aromatic C=O groups in the form of carboxyl and aromatic C-O groups. It also has aliphatic oxygen functional groups mainly as C-O groups. By comparison, coal B may consist of phenols or phenolic oxygen atoms, and relatively less aliphatic C-O groups. This hypothesis also agrees with abundance of oxygen content in coal S examined by proximate analysis (Table 3-1).

The aliphatic chain length could be calculated based on both ATR-FTIR (CH_2/CH_3 ratio) and ^{13}C NMR (f_{al}/f_a^s ratio). In ATR-FTIR, the CH_2/CH_3 ratio demonstrated the longer aliphatic chains for coal S than coal B, which was later approved by the f_{al}/f_a^s ratio. The relatively higher values of f_a^s and σ+1 for coal B indicated that it contains more attachments than coal S. The difference of attachments may be because coal B has higher aromaticity and larger cluster size providing more sites for attachments. Therefore, the chain length and number of attachments revealed that coal S exhibited longer aliphatic chains, although coal B might have more but shorter attachments.

Combining the FTIR, XPS and ^{13}C NMR results, the molecular structural models of the two raw coals were established as shown in Figure 5-7. Coal S was proposed as two aromatic rings as its predominant molecular structure to correspond to the M.W. value (272) obtained by ^{13}C NMR. However, minor larger aromatic clusters likely exist in its molecular structures.

Coal B was mainly exemplified as a liner catenation because Yang et al. (2017) proposed that liner catenations of aromatic rings are more likely to occur in the structure of coal when the carbon content of coal is < 87% [177], and the carbon content for coal B was 85.54% (Table 3-1). Noteworthy is that circular catenations of four aromatic rings or more may also exist in coal B. The actual structures of coals must be significantly more complex [23].

Nevertheless, the simplified models include the main features of the two coal molecular structures and could facilitate the understanding of the structural difference of the two coals providing a basis for the interpretation of coal oxidation with NaClO.

Coal rank and maceral composition correspond well with the different structural properties of the studied coals. It has been reported that the increase of aromaticity, the loss of aliphatic and oxygen content, the decrease of aliphatic chain length are associated with increasing coal maturation [121, 151, 154, 177]. Additionally, the structural characteristics of the two studied coals also agree with their maceral compositions. The two coal samples had comparable vitrinite content but coal S possessed more liptinite (29.0%), while coal B was relatively rich in inertinite (32.4%), as shown in Table 3-2. The molecular structures varied significantly in different maceral compositions [31]. Firstly, liptinite has been shown to contain the highest concentrations of aliphatic moieties and the lowest aromatic moieties compared to other maceral groups at similar maturities, while inertinite consists of the most aromatic moieties, with vitrinite displaying intermediate values. Secondly, liptinite has significantly higher CH_2/CH_3 ratios compared to vitrinite and inertinite, indicating that liptinite generally comprises longer and less branched aliphatic chains containing lower terminal CH_3 relative to methylene CH_2 [31, 153, 167].

a.

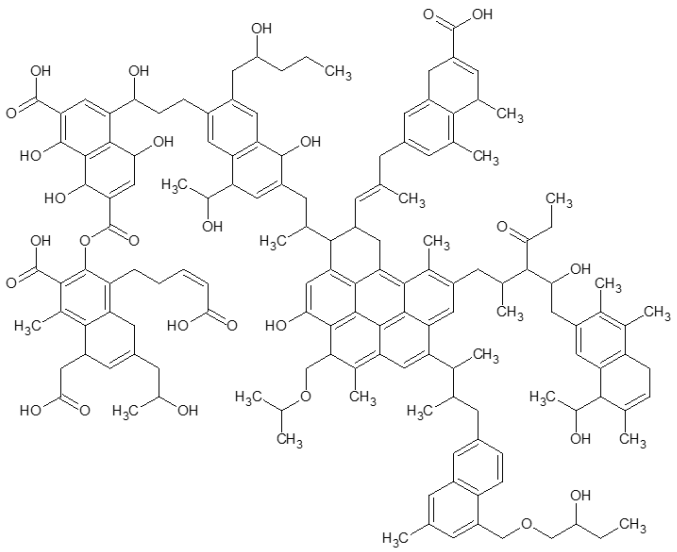

b.

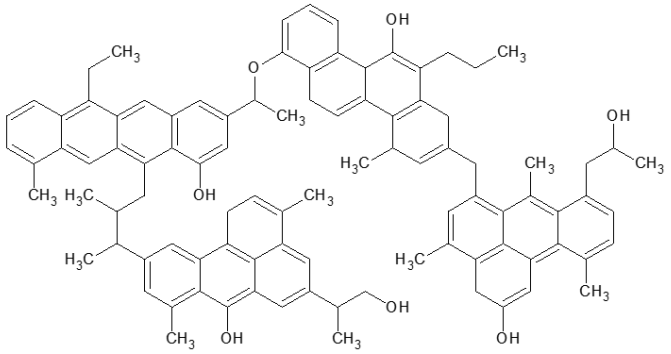

Figure 5-7. Models of molecular cluster of coal S (a) and coal B (b).

5.4.2 Oxidation induced coal structure variation

The oxidation induced coal structures were mainly characterized as lower aromaticity, raised oxygen content and longer aliphatic chains, regardless of the coal types. Coal oxidation could decrease coal molecular aromaticity which is indicated by the parameters including H_{ar}/H_{al} (FTIR) and f_a (NMR). For coal S, NaClO oxidation dropped the H_{ar}/H_{al} index from 0.07 to 0.03, and similarly the f_a decreased from 0.53 to 0.37. Moreover, the NMR spectra for coal S explicitly illustrated the decrease of aromaticity after oxidation. The decrease of H_{ar}/H_{al} index and f_a also occurred for coal B. The decrease of the aromaticity for the oxidised coals indicates the breakage of the aromatic clusters.

Furthermore, NaClO oxidation increases the oxygen content for both coals. It was clearly demonstrated by all the methods, correspondingly and complementally. The results showed the generation of the carboxyl or carbonyl bonds on the oxidised coal structure, and they

could be derived partially from the initial C-O, because after oxidation, the C-O bond proportion decreased for both coals.

Additionally, the aliphatic chains of the oxidised coals were approved to be longer than the initial coal samples. The increase of CH_2/CH_3 ratio and f_{al}/f_a^s ratio identified this change for both coals. It is proposed that the increase in aliphaticity plus existence of longer aliphatic chains are due to breakage of benzene rings, given that, there is no other plausible reason.

The above coal molecular structure variations before and after oxidation appear to be independent on coal types, however the coal types seem to influence the coal molecular cluster size change pattern after oxidation, as identified by NMR results. For coal S, the NaClO oxidation generates more bridgehead carbons (x_b=0.26) than the pre-treatment coal S (x_b=0.16). This is associated with larger cluster size after oxidation, average 24 carbons per cluster for oxidised coal compared to 9 before oxidation. By comparison, the coal oxidation lowered the proportion of bridgehead carbons (f_a^B =0.10) for coal Bo and accordingly, decreased the cluster size (C=9).

Therefore, based on identification by the techniques, the molecular structural models of oxidised coal So and coal Bo were established, as shown in Figure 5-8. Although these schematic models only include carbon, oxygen and hydrogen, it is noteworthy that chlorine (Cl) might exist in the molecular structures of the oxidised coals [20, 122]. For coal S, although large aromatic clusters were detected in the oxidised structure, its proportion was identified to be low, and it is surrounded by long aliphatic chains bonded with abundant oxygen. One reasonable hypothesis could be that NaClO predominantly broke off the smaller aromatic rings, leaving the larger clusters, increased aliphatic chains and more oxygen functional groups in the structure. This oxidised structure led to a further 32% mass loss when contacted to NaClO again.

For coal B, which appears to contain larger aromatic clusters than coal S, the NaClO volume in the first oxidation could only be able to breake poly-condensed aromatic rings into smaller clusters with longer aliphatic chains and more O-C=O groups. This size reduced molecular structure was very similar with that of coal S. Indeed, the subsequent oxidation of coal Bo gave a similar mass loss to that of coal S. The oxidation induced coal structure variations for the two coals shed light on the oxidation mechanism.

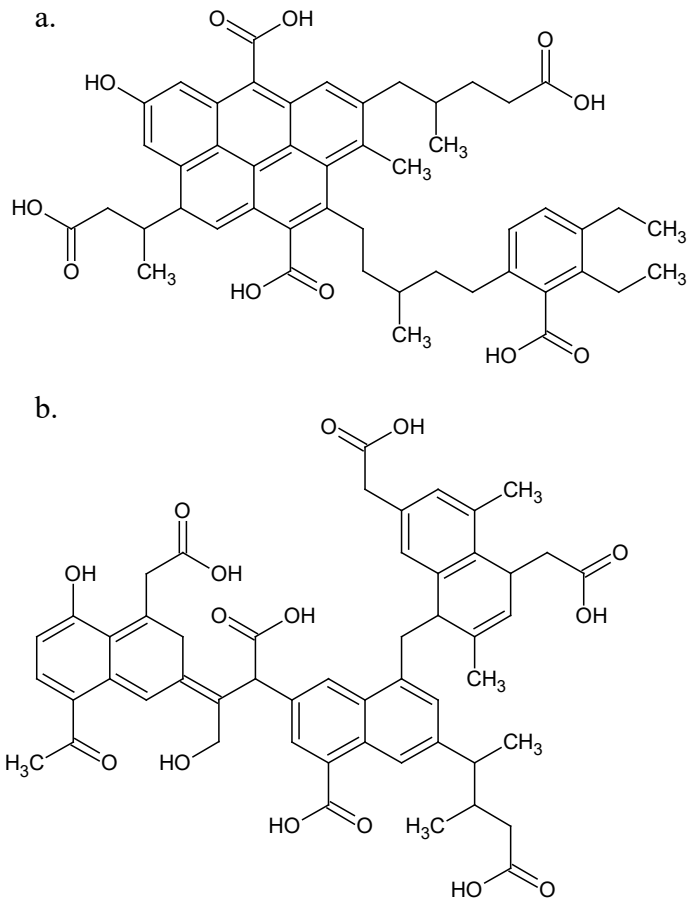

Figure 5-8. Supposed molecular models of coal So (a) and coal Bo (b).

5.4.3 Coal oxidation mechanism in NaClO

Our previous research showed that coal S could react more vigorously than coal B when in contact with NaClO [179]. Firstly coal S dissolved 10 times more than coal B in NaClO and secondly, artificial channels in coal S could be etched more by NaClO than coal B [179]. Combining with the molecular structure of coal S indicated in the current study, the NaClO oxidation could be proposed that it prefers to react with longer aliphatic chains, higher oxygen content, and smaller aromatic clusters.

The preference of NaClO to oxidise aliphatic chains has been supported by previous research, where the reaction filtrate was analysed and showed the abundance of aliphatic acids including short-chain alkanoic acids and alkanedioic acids in the oxidative products [15, 17]. Aliphatic bands, and CH_2 in particular, were widely reported to be prone to oxidation [148, 167]. This might be because the C-C bond in the aliphatic chain is weaker (lower Bond Dissociation Energy, or BDE) than the C- aromatic ring bond [156]. Lin et al. (1993) reported

the BDE of aliphatic C-C in (C_6H_5) CH_2-CH_3 was 72 kcal/mol, compared to 99 kcal/mol for C=C bond [156]. Therefore, the aliphatic C-C bond within the coal structures were inferred to be weak, becoming the most likely sites of bond rupturing during oxidation. Oxygen functional groups were also reported to play a significant role in NaClO oxidation. Firstly, Mae et al. (1997) proposed the weak oxygen-carbon bonds were easy to be oxidised [17, 86]. Secondly, the higher content of oxygen functional groups could improve the coal hydrophilicity, thus promoting the interaction between coals and NaClO [17, 162].

Furthermore, NaClO is able to attack and break the aromatic rings, which could be indicated by the decrease of aromaticity and the increase of aliphatic carbons for both coals. The highly condensed aromatic rings in coal B were oxidised into less condensed aromatic clusters and aliphatic chains firstly. This relatively simple structure (coal Bo), similar to coal S, was favourable to NaClO oxidation and thus, a massive coal dissolution was achieved as expected when coal Bo came to contact with NaClO. Although the second oxidative residue for coal B was not examined, the coal S oxidation might show how NaClO oxidise the less condensed structures. The abundant small aromatic rings together with oxygen functional groups and aliphatic carbons might predominantly consume the NaClO, remaining the highly condensed but rare aromatic clusters. This mechanism could be supported by the molecular structure of coal So, massive average cluster size (C=24) in the aliphatic predominant (63%) structures (Figure 5-8a).

Therefore, the coal oxidation in NaClO mechanism could be summarised as the NaClO preferentially oxidise the side chains in the presence of oxygen functional groups and it could also attack and break some aromatic rings, particularly the smaller ones.

Overall, the findings in this study address the research questions and fill the gap of the knowledge about the different molecular structures between different rank coals and their molecular structure variation after NaClO oxidation. The coal molecular structures before and after oxidation further contribute to the understanding of the coal oxidation mechanism by NaClO. This is of particular importance because it could benefit the determination of a candidate oxidant stimulation target for raising coal permeability.

5.5 Conclusion

To interpret the effect of coal types on NaClO oxidation and to investigate the oxidation mechanism, a subbituminous coal S and a bituminous coal B were collected from the Surat Basin and Bowen Basin, Australia, respectively. The molecular structures of the two coals and their oxidised residues were examined and compared using attenuated total reflectance Fourier transform infrared spectroscopy (ATR-FTIR), X-ray photoelectron spectroscopy (XPS) and solid state ^{13}C nuclear magnetic resonance spectroscopy (^{13}C NMR). Based on the results, the molecular structure schematic models of the studied coals and their oxidised residues were established. After comparing and analysing the molecular structures, the main conclusions are as follows:

1. The lower rank coal S is less aromatic, more aliphatic and higher oxygen content.

2. NaClO prefers to react with aliphatic chains, particularly with oxygen functional groups, evidenced by coal S being more reactive.

3. NaClO tends to react with small aromatic rings first, evidenced by the loss of smaller clusters in coal S, remaining the larger aromatic clusters. Then it is able to attack the larger aromatic clusters, confirmed by the cluster size decrease for coal B.

4. After NaClO oxidation, the aromaticity drops for both coals, suggesting the reaction between NaClO and benzene rings. The breakage of the aromatic rings leads to the longer aliphatic chains in the oxidised coal residues.

5. NaClO oxidation products are rich in C=O and O-C=O, detected for both coals.

The findings in this study promote an understanding of the difference in the initial molecular structures of the two different rank coals and their oxidation mechanisms in NaClO. This understanding will fill the gap of the knowledge in the area of coal oxidation by NaClO and contribute to the decision of selecting the oxidant stimulation targets for enhancing coal permeability.

Chapter 6. Permeability variation and coal structure changes after HCl and NaClO flooding.

6.1 Introduction

Chemical stimulation has attracted increasing interest recently, which includes acid stimulation and oxidant stimulation [9-11, 180]. The former targets at removing the minerals from the cleats, while the latter is dedicated to dissolve the coal matrix to etch the initial cleat surface and/or generate new fractures to increase cleat apertures. In addition, weakening the coal matrix by oxidant reactions may also prove applicable for pre-hydraulic fracturing.

In chapter 4, matrix pore size enlargement and the cleat aperture dilation were reported. However, these results were only obtained based on coal particles and open artificial coal cleats, which are different from the coal cleat system *in-situ*. Additionally, the lack of confining pressures in these experiments further raised questions about the application of these results for *in-situ* conditions where the overburden pressure is considerably high.

Therefore, in this chapter, the coal samples, containing fully developed cleat systems, were used to explore the effect of acidisation and oxidation on coal permeability under confining pressure. Besides, the cubic samples used in the core flooding test is able to measure the horizontal permeability variation and CT scanning of coal samples before and after oxidation. CT scanning can identify the coal structure modification to benefit the understanding of the different stimulation effects and mechanisms.

6.2 Methodology

6.2.1 Samples

The NaClO oxidation effect on coal permeability was studied based on Bowen Basin coals. Coal core samples were used to measure the vertical permeability and labelled as BV coals, while cube samples cut from cores were used for horizontal permeability (BH). Sample BV1 and BV2 used in this study had been flooded with 1% HCl previously by Turner et al. (2016) where they were labelled as sample “A1” and “A2” [11]. In the current research, only oxidant (1% NaClO) is injected into the two core samples. BH samples are raw coals, although they

were from the same borehole with the samples labelled “C” in the research conducted by Turner et al. (2016) [11]. Both acid and oxidant have been injected into BH samples to examine the effects on coal structures and coal horizontal permeability. The mineral in formation in these coals and the acid stimulation results reported by Turner et al. (2016) [11] are summarised in Table 6-1.

Table 6-1. Summary of coal sample information and vertical permeability change after 1% HCl flooding, according to Turner et al. (2016) [11].

Sample name		Minerals in cleats			Permeability change after 1% HCl, vertical
Current study	Turner et al. (2016)	Majors	Moderates	Trace	
BV1	A1	Kaolinite	Pyrite	Apatite, Anatase	decrease 16%
BV2	A2	Kaolinite	Pyrite	Apatite, Anatase	decrease 15%
	C1	Kaolinite, Calcite	Smectite	Illite (K)	increase 132%
	C2	Calcite, Barite	Illite (K), Kaolinite	Smectite (K)	decrease 30%
BH	C3	Calcite, Barite	Illite (K), Smectite	Smectite (K)	increase 23%
	C4	Calcite, Barite	Illite (K), Kaolinite	Smectite (K)	increase 20700%

6.2.2 Core flooding test

Steady state coal permeability was performed using the core flooding rig system shown in Figure 6-1. The system mainly includes a Hassler core holder (Core Laboratories); one high pressure Quizix QX6000 dual cylinder pump (Chandler Engineering) for fluid injection; one Redox gas/oil tank for confining pressure control; Gems 3200 series pressure transducers (0-100 bar) to measure both pore pressure drop and confining pressure; and a dome loaded back pressure regulator (Equilibar, USA) to maintain fluid pressure drop across the sample. Wetted parts were predominantly Hastelloy to provide superior corrosion resistance to brine, dilute acids and oxidants. The components in the system have been reported in details previously [10, 11, 181].

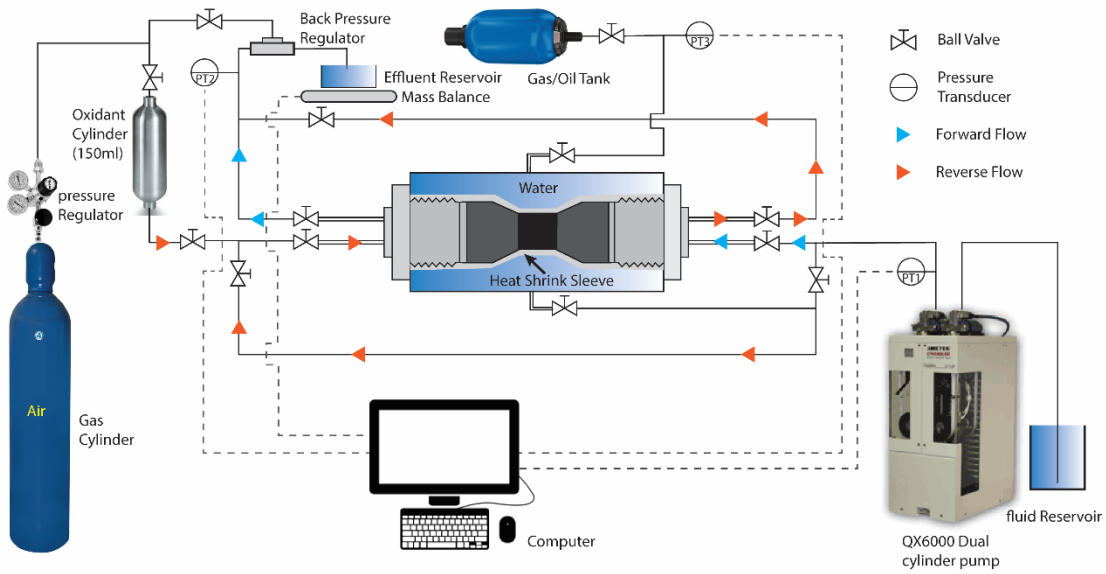

Figure 6-1. Schematic of core flooding system

Instead of flooding brine and the stimulants in the same direction, this system allowed the simulant to flow in a reverse direction to mimic the stimulation procedure *in-situ*. Additionally, the brine and acid was injected through the sample by the pump, while the air was used to push the oxidant candidate into the coal samples, which could protect the pump from the oxidant erosion. For each run, the oxidant volume flowing through the coal was deliberately monitored to be less than the oxidant cylinder volume to prevent the gas from entering the coal samples.

Prior to the flooding test, the coal sample was X-ray CT scanned to characterise the coal sample structures, particularly the fracture systems. The details about X-ray CT scanning is described in the following section 6.2.3 and has been reported previously [10, 13, 182, 183]. The flooding tests start with the coal samples saturated in brine (4% KCl) to enable the coal to be equilibrium and consolidated via repeated loading/unloading cycles. Once the saturation was established, a forward brine injection was conducted until the permeability stabilised to set an initial permeability baseline. Afterwards, the stimulant, 1% HCl in acid stimulation or 1% NaClO in oxidant stimulation, was injected reversely until the permeability stabilised under the same circumstances, i.e. same confining pressure (P_c), inlet pressure (P_1) and outlet pressure (P_2). This was followed by a second forward flow with brine to compare the permeability change before and after stimulation. Subsequently, the sample was X-ray CT scanned again to investigate the coal structure change after flooding test. The pressure details about the core flooding tests are summarised in Table 6-2.

Liquid samples were regularly collected from the core holder outlet and exposed to the element concentration analysis via inductively coupled plasma optical emission spectroscopy (ICP-OES) in acid stimulation or to the total organic carbon (TOC) analysis in oxidant stimulation, respectively. The procedure of ICP-OES or TOC analysis could be found elsewhere [11, 180].

Table 6-2. Pressure system of the coal flooding test for each sample.

Sample	Stimulant	Flooding direction	Pressure system			
			P_1 (bar)	P_2 (bar)	P_c (bar)	P_e (bar)
BV1	1% NaClO & 4% KCl	vertical	10	4	25	18
BV2	1% NaClO & 4% KCl	vertical	10	4	25	18
BH1	1% HCl & 4% KCl	horizontal	15	4	25	15.5
	1% NaClO & 4% KCl	horizontal	10	4	25	18
BH2	1% HCl & 4% KCl	horizontal	15	4	25	15.5
	1% NaClO & 4% KCl	horizontal	10	4	25	18
BH3	1% NaClO & 4% KCl	horizontal	10	4	50	43

P_1= inlet pressure, P_2= outlet pressure, P_c= confining pressure, P_e= effective pressure

6.2.3 X-ray computed tomography (CT) scanning

X-ray computed tomography (CT) studies were employed to detect and map the structural changes in the sample. An Inveon Multimodality PET/CT scanner (Seimens) at the Centre for Advanced Imaging (CAI), The University of Queensland, was used (voltage=80 kV, beam current=0.5 mA) to image the coal sample before and after stimulation.

Scanned images of the core were reconstructed, visualised and normalised using the Inveon™ Research Workplace software (Seimens IRW v4.2). The 3D reconstructions and visualisation enabled qualitative surveys. These surveys were fundamental to understanding core structure and essential for validating the generated core profiles. Greyscale image normalisation, attained by keeping the contrast parameters constant, allowed for comparison of the images before and after stimulation. These axial greyscale images (display resolution=44 μm) were then used for mapping the mineral and fracture profiles of the core before and after stimulation. Core profiling involves image stack generation, slice histogram extraction, image segmentation and fractionation. The image stacks, each containing ~1600 greyscale axial slices (images) were manually registered,

stabilised and cropped prior to extracting the slice histograms using plugins and macros embedded in ImageJ software.

Image segmentation into three coal components, namely unfilled fracture (voids or fracture porosity), coal matrix and minerals, was achieved via greyscale unit (GU) thresholding. Components were allocated specific greyscale ranges following detailed surveys of the greyscale values of visually discernible structures.

Fracture and mineral fractions (X_f) of individual slices were estimated using Equation 6-1, where $\sum PX_{GUrange}$ is the sum of pixels within the greyscale range (lower to upper limit) of the component and $\sum PX_{0-255}$ is the total pixels for the entire slice. Following estimates validation, the core profiles were compared to identify the structural changes and elucidate the effects of the treatment [10].

$$X_f = \frac{\sum PX_{GUrange}}{\sum PX_{0-255}} \qquad \textit{Equation 6-1}$$

6.3 Results

6.3.1 Effect of oxidant stimulation on vertical permeability

Two coal cores, BV1 and BV2, which have been flooded with 1% HCl previously by Turner et al. (2016) [11], were used to examine the effect of oxidation on vertical permeability.

6.3.1.1 Coal core sample BV1

BV1 experienced two stages of oxidation, 30% H_2O_2 and 1% NaClO. Figure 6-2 shows the corresponding permeability changes with each stage. The permeability of initial forward flow (F1) with brine was 2.01mD, followed by the 30% H_2O_2 (total 40ml) oxidation procedure, where the permeability dramatically dropped to 0.08 mD in a reverse flow, although a permeability increase could be observed at the beginning of this stage. To examine the oxidation effect, a second forward flow (F2) was conducted with a measured permeability 0.59 mD, showing the detrimental effect of 30% H_2O_2 on permeability. Afterwards, 50ml of 1% NaClO was injected into the same sample, and the permeability was recorded to be

steadily declining from 0.25 mD to 0.05 mD. Subsequently a final forward flow (F3) showed the permeability stabilised at 0.17 mD, much lower than the initial 2.01 mD.

TOC results (Figure 6-2) reflected that initial TOC concentration was quite low, setting a blank test for the following procedures. During the H_2O_2 flooding, TOC increased slightly, but was still lower compared with the TOC measured during 1% NaClO stimulation. The TOC concentration in the effluent increased with the injection of NaClO. It then dropped to a lower level in the brine flooding. TOC results showed the reaction between coal and 30% H_2O_2 is slighter than that with NaClO.

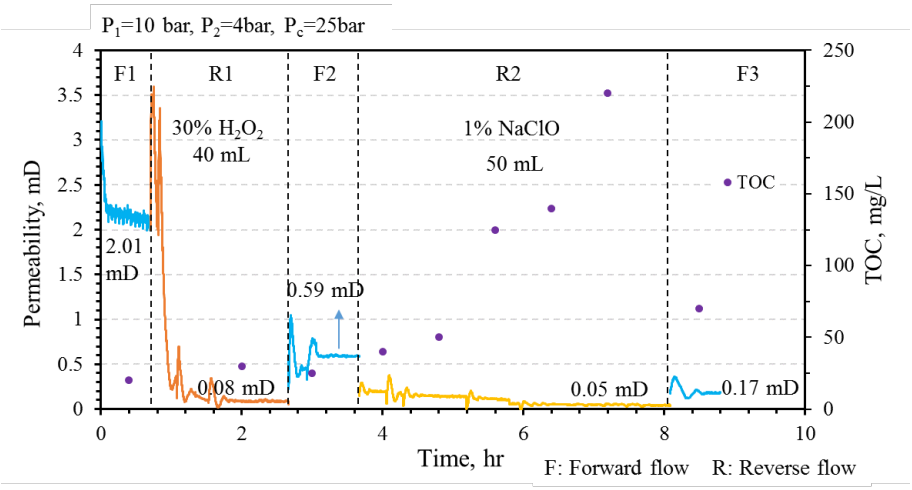

Figure 6-2. Permeability and TOC concentration variation at different oxidation stages (30% H_2O_2 and 1% 5% NaClO) for coal BV1. P_1=10 bar, P_2=4bar, P_c=25bar.

Figure 6-3 shows the structure variation of sample BV1 pre and post 30% H_2O_2 and 1% NaClO oxidation. The coal core was divided into upper and lower sections as shown in Figure 6-3a. In the upper section, more void spaces existed initially, as shown in Figure 6-3e illustrating the VF distribution along the coal axis, while the lower section was physically tighter. After oxidation treatment, it is the upper section where the massive coal structure change occurred by comparing Figure 6-3a and f. The structural change mainly exhibited as massive void space generated by oxidation, while comparable mineral contents remained, as shown in Figure 6-3i. Furthermore, Figure 6-3g shows the coal dissolution occurred along a bedding plane which is clearly shown in Figure 6-3a. In the lower section, by comparison, the structure primarily kept intact without discernible change (Figure 6-3f).

The cross-sections could further contribute to illustrating the difference of the structural change between upper and lower sections. Figure 6-3b and Figure 6-3g are the cross-

section CT images at the same site of the upper coal core before and after oxidation, while Figure 6-3c and Figure 6-3h are from the same position of the lower section. Apparent change could be observed in Figure 6-3g, where the void space accounted for 30% of the whole image and a horizontal fracture existed on the left of the image. However, this change did not occur on Figure 6-3h.

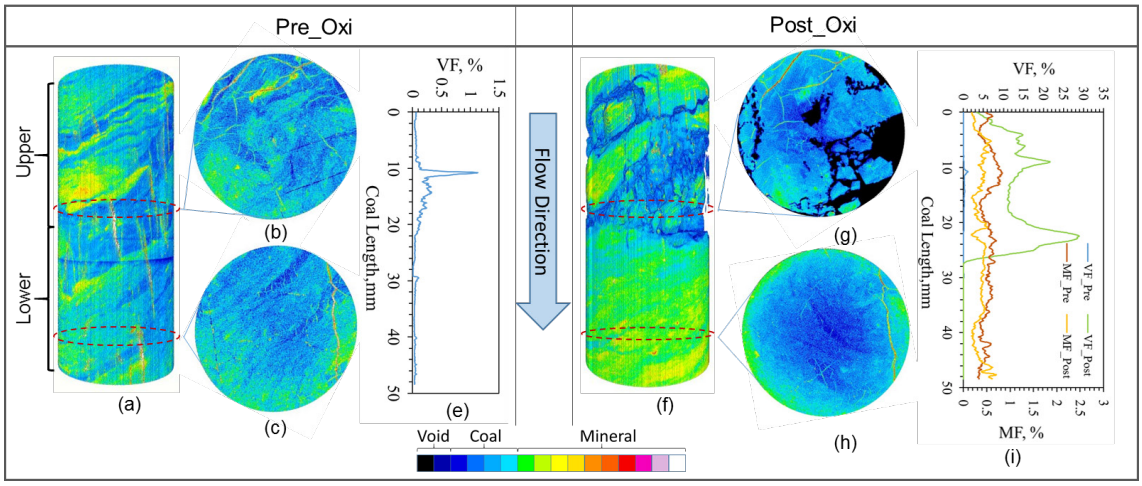

Figure 6-3. Coal BV1 structure analysis with CT scanning models pre and post oxidation.

6.3.1.2 Coal core sample BV2

Due to the slight reactive effect of 30% H_2O_2 on coal, 1% NaClO was singly used for coal BV2 stimulation. Figure 6-4 shows the permeability variation for coal BV2 during oxidant stimulation procedure. The initial permeability was 0.59 mD and gradually dropped to 0.02 mD during the 230 mL NaClO flowing through coal core, albeit fluctuant. Afterwards, a forward 4% KCl flow was conducted and the permeability stabilised at 0.14 mD, which indicated the negative effect of 1% NaClO oxidation on the vertical permeability.

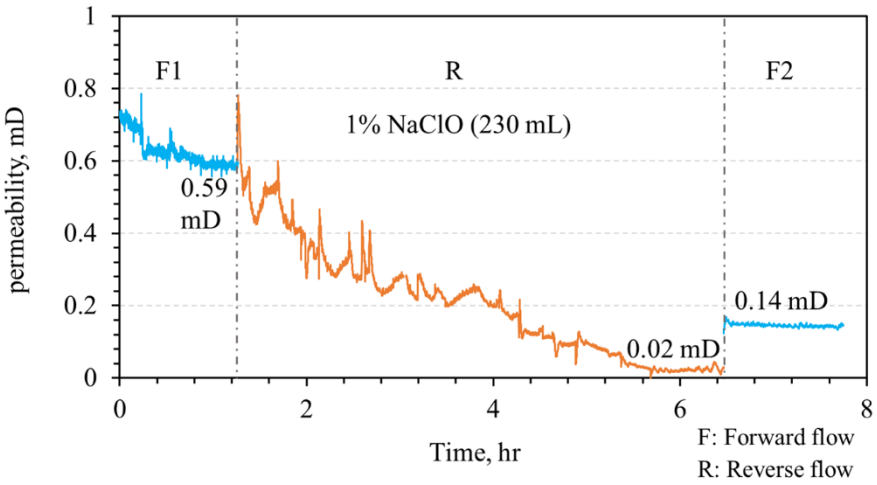

Figure 6-4. Permeability variation of BV2 in 1% NaClO stimulation. P_1=10 bar, P_2=4bar, P_c=25bar.

Figure 6-5 compares the coal core structure change induced by oxidation based on CT scanning data. The core flooding directed from top to bottom. Compared with Figure 6-5a, which shows the initial coal core 3D model, a group of fractures occurred at the middle of the coal core after oxidation (Figure 6-5e). The high TOC in the outlet fluid indicated that these fractures seemed to be generated by chemical attack. The cross-section CT images could further help to illustrate the fracture pattern from a top to bottom view. On Figure 6-5f, the fractures or void spaces, which did not exist pre oxidation (Figure 6-5b), expended horizontally through the coal core. The VF after oxidation increased significantly, particularly located in the middle of the coal (Figure 6-5g), which was initially more porous than the other parts (Figure 6-5c). At the same section the new fractures developed, which formed a connected layer in a ~30° angle with horizontal plane (Figure 6-5h).

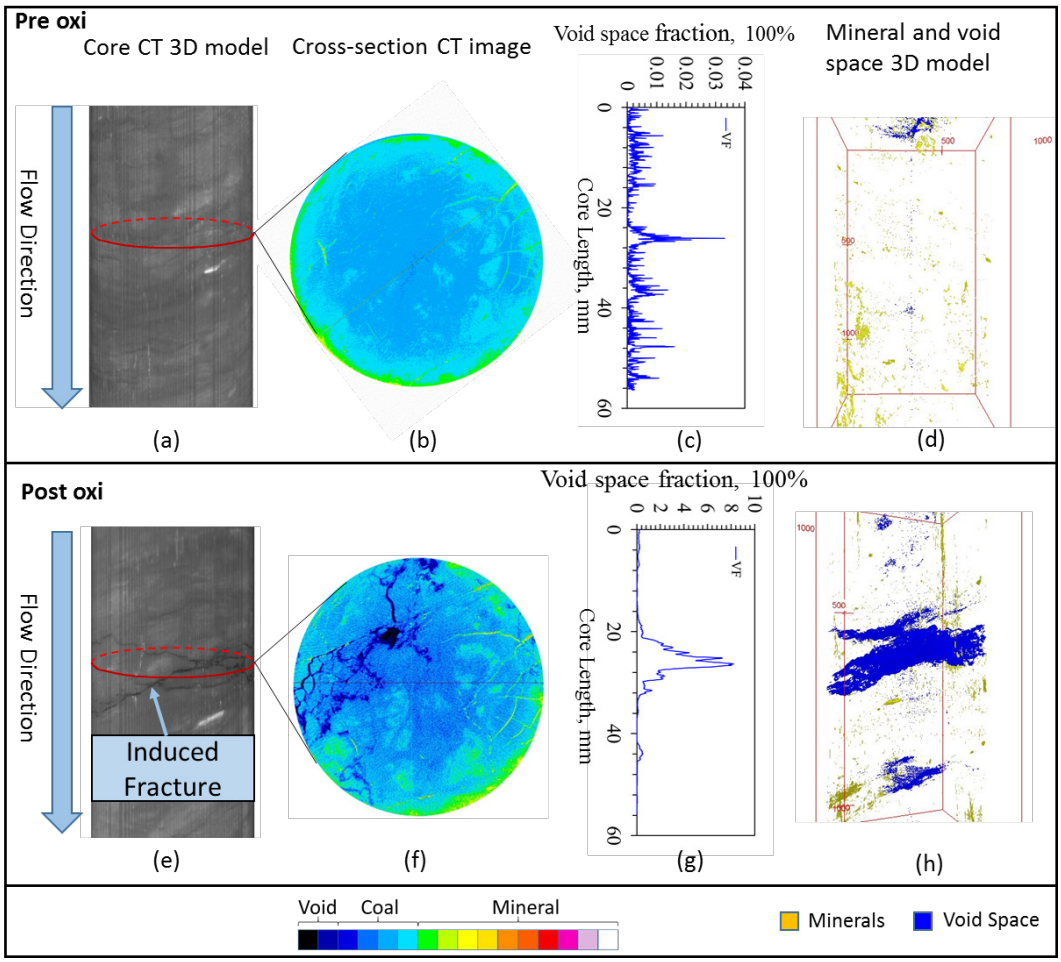

Figure 6-5. BV2 coal structure analysis based on core CT scanning.

6.3.2 Effect of acid and oxidant stimulation on horizontal permeability

6.3.2.1 Cube sample BH1

Cube samples enabled the horizontal permeability to be measured parallel to the coal bedding plane. Figure 6-6 shows the permeability variation and the demineralisation during 1% HCl stimulation for coal BH1. The permeability of initial forward flow was 0.033 mD. When the 1% HCl was injected into the coal and the flow direction reversed, permeability soared to 1.2 mD but gradually declined to 0.38 mD with a total 1550 mL 1% HCl flowing through. The following forward flow started with a high permeability (0.8 mD) at the beginning, but gradually exhibited a declining flow behaviour, eventually reaching 0.35 mD, which was 10 times higher than the initial forward permeability.

The increase of permeability during HCl flooding was accompanied by a drastic elevation of the calcium (Ca) concentration and a minor iron (Fe) as shown in Figure 6-6, indicating the massive dissolution of calcite ($CaCO_3$) and a slight dissolution of ankerite ($Ca(Fe, Mg, Mn)(CO_3)_2$). By contrast, the scarce concentration of phosphorus (P) excluded the existence of apatite ($Ca_5(PO_4)_3(F,Cl,OH)$). The concentration of aluminium (Al) and barium (Ba) were indiscernible. The element analysis results in the flooding test solution by ICP-OES for coal BH1 are summarized in Appendix Table 2.

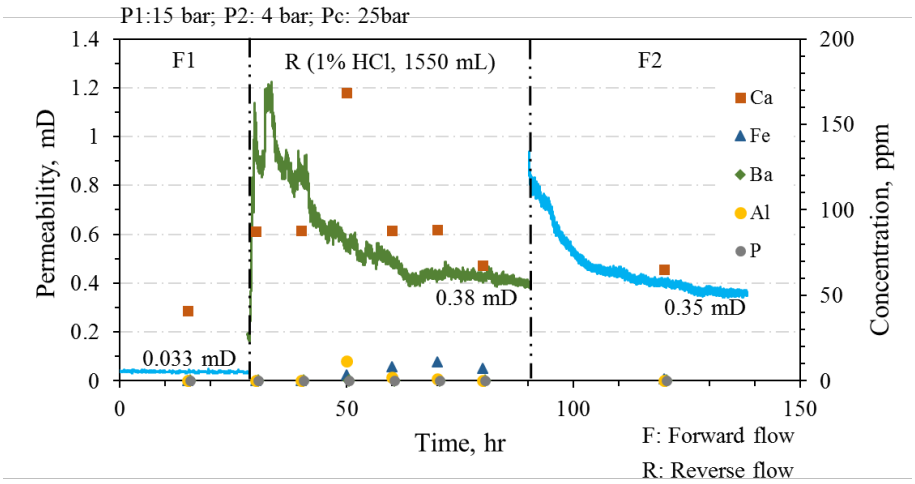

Figure 6-6. Permeability and element concentration change during 1% HCl stimulation for coal BH1. P_1=15 bar, P_2=4bar, P_c=25bar.

Figure 6-7 shows the permeability and TOC concentration variation for coal BH1 during 1% NaClO flooding test. The initial forward permeability was 0.038 mD. The reverse permeability was 0.118 at the beginning and generally dropped to 0.04 mD after 60 mL 1% NaClO flowing through. The forward flow post oxidation showed a horizontal permeability of 0.003 mD, revealing the damage to coal flow capacity caused by oxidation.

TOC concentration in the initial forward flow was only 14 mg/L, and drastically increased with the injection of NaClO to reach 350 mg/L. Afterwards, it dropped to 26.62 mg/L in the post forward flow.

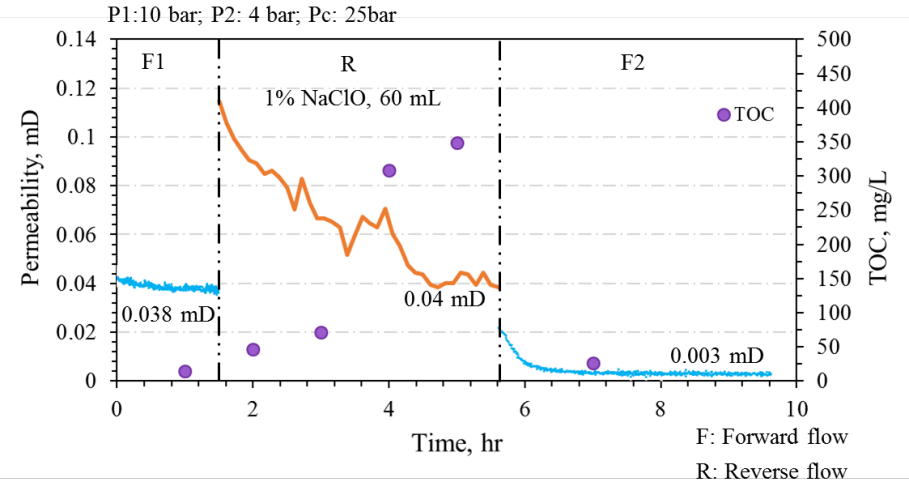

Figure 6-7. Permeability variation during 1% NaClO stimulation for coal BH1. P_1=10 bar, P_2=4bar, P_c=25bar.

Figure 6-8 shows the coal structure change associated with acid and oxidant stimulation based on CT scanning images. The CT images were collected and shown in two directions, Y direction, which was the coal flooding direction, and Z direction. In Y direction, the CT images from the same site of the coal pre stimulation, post acid stimulation and post oxidant stimulation were shown in Figure 6-8b, c and d respectively. The sites selected by the red dash rectangle in these figures were exemplified as a typical change of the coal structure undergoing the stimulations. The "π" type minerals initially filled in the fractures in the bright coal band before stimulation (Figure 6-8b), and vanished after acid stimulation (Figure 6-8c). Then after oxidant flooding, the site was shown as a vacant fracture (Figure 6-8d). The variation of fracture features explicitly indicated the demineralisation procedure during acid stimulation and the fracture etching effect of oxidation.

These fracture feature variations were confirmed by viewing CT images in Z direction as shown in Figure 6-8e (virgin), Figure 6-8f (post-acid) and Figure 6-8g (post oxidant). The images were a cross section selected in the bright coal band which was highly mineralised (Figure 6-8e). The minerals filling in the cleats highlighted by the red ash ellipse obscured after acid stimulation and a void cleat appeared at the same section after oxidation. Moreover, after oxidation, the vacant cleats formed a fracture system across the sample.

Figure 6-8h, Figure 6-8i, Figure 6-8g represent the 3D models of void space and minerals in the coal in the Z direction, before stimulation, post acid and post oxidant stimulation, repetitively. The minerals extensively distributed in the whole sample before acid stimulation, but after acid flooding, the amount of minerals decreased, especially in the middle of the

sample. After oxidation, an apparent void fracture could be observed across the whole sample in the XY plane (horizontal plane).

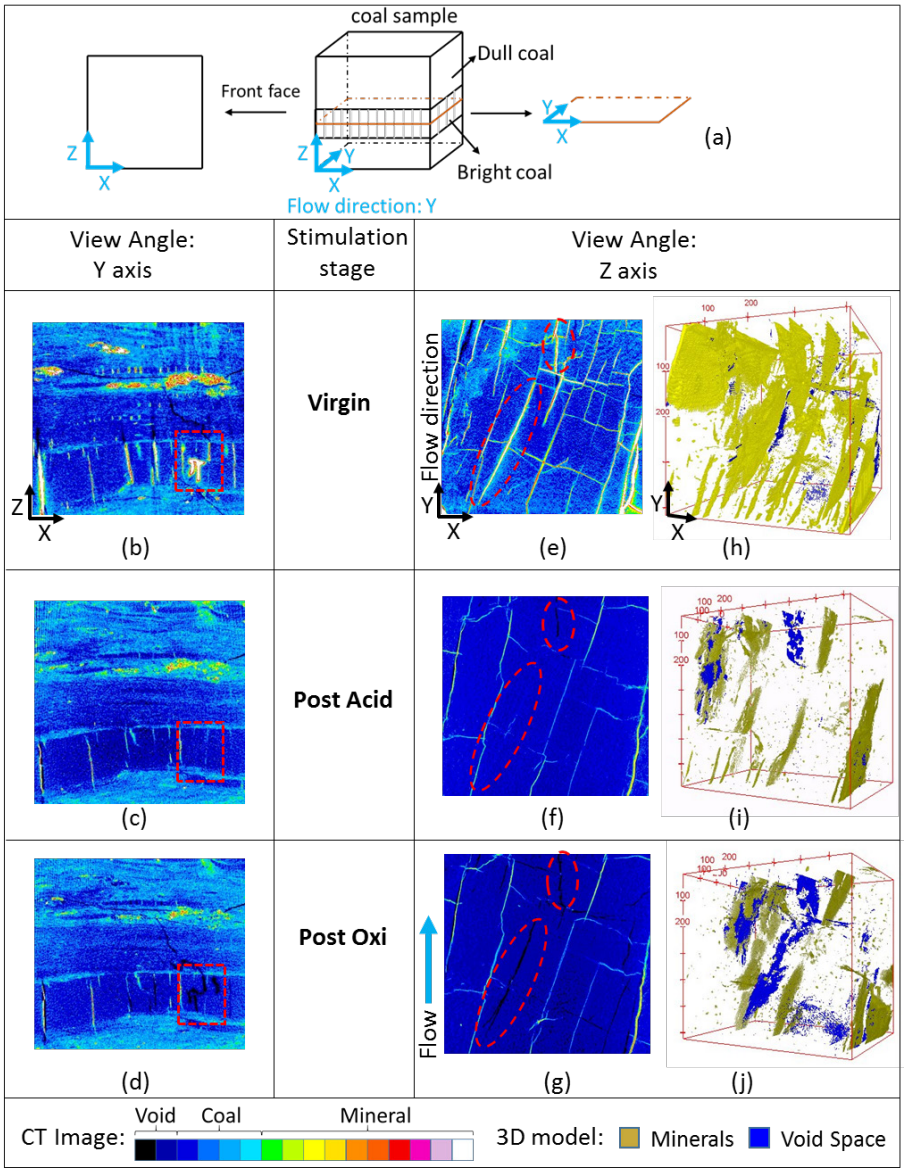

Figure 6-8. BH1 coal structure change after acid and oxidant stimulation.

Figure 6-9 shows the initial structure 3D model for coal BH1 (a) and associated MF distribution (b) and VF distribution (c) calculated along the coal sample vertically. The 3D model illustrates two parts of minerals, of which, the upper part might be dotted in the dull coal and the lower part appeared to fill in cleats in bright coal bed. The mineral distribution was reflected in Figure 6-9b (blue line) with two humps showing the mineral fractions. In the bright coal bed, the 3D model also shows the existing of void space associated with the minerals as quantified in Figure 6-9c (blue line).

After acid stimulation, the drop of mineral fraction is clearly shown in Figure 6-9b that the original two humps disappeared and mineral fraction stayed in a similar low level along the whole coal sample. By comparison, the void space was massively created also shown as two humps at the locations where minerals existed initially. Afterwards, the oxidation further enlarged the void space regardless of the coal types where they existed, as shown in Figure 6-9c. However, NaClO appeared to influence the minerals barely. Overall, the results clearly quantified the demineralisation of acid stimulation and the enlargement of void space after oxidation.

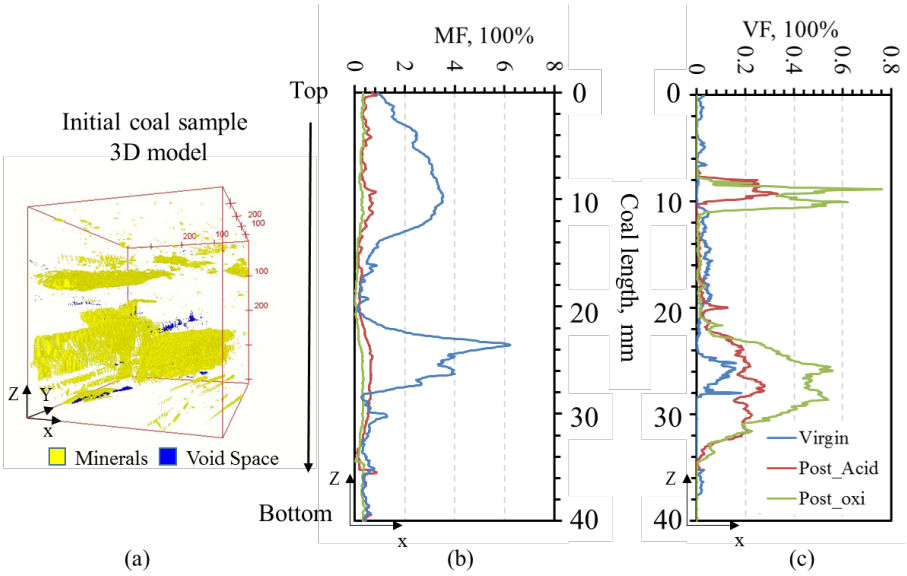

Figure 6-9. Void space fraction and mineral fraction for coal BH1.

6.3.2.2 Cube sample BH2

Figure 6-10 illustrated the permeability variation for coal BH2 during HCl stimulation. The initial forward flow had a horizontal permeability of 0.35 mD, which generally increased to 1.21 mD after 1700 mL 1% HCl flowed through the coal sample. Afterwards, the post-stimulation forward flow started with a significantly high permeability (2.7 mD) and quickly dropped and stabilised at 0.85 mD, eventually. The permeability variation means the 1% HCl stimulation could elevate the permeability 2.42 times for coal BH2.

Upon injection of HCl, there was a spike in the concentration of Ca in the effluent, from 65 ppm in the initial brine flow to 500 ppm in the 1% HCl flooding. Then it decreased dramatically with increasing HCl injection. The concentrations of P and Fe were much higher

than those in BH1, indicating the higher content of apatite ($Ca_5(PO_4)_3(F,Cl,OH)$) and ankerite ($Ca(Fe, Mg, Mn)(CO_3)_2$). Concentration of Ba deriving from barite ($BaSO_4$) was much higher in the initial brine flooding for coal BH2 than that for coal BH1, indicating a high barite content existing in the coal structures. The abundant barite in coal BH was reported by Turner et al. (2016) and shown in Table 6-1. As barite could not be dissolved in HCl, the increasing concentration of the Ba during 1% HCl flooding might be due to the weak hydrofluoric acid (HF) formed by the dissolution of apatite in HCl [181]. The weak HF could also dissolve kaolinite ($Al_2Si_2O_5(OH)_4$)), and this could explain the hump of Al concentration at the end of acid flooding. Besides, previous mineral analyses results showed that the epigenetic minerals in the cube sample were mainly calcite while the syngenetic minerals were clays [11], which also explained why the concentration of Ca existing in the main flowing pathways increased earlier than Al. Nevertheless, the level of Al stayed low generally, indicating a low content of kaolinite in the sample. CT scanning images failed to explain the coal structure change due to the X-ray beam harden caused by massive mineral contents, particular the high concentration of barite. The element analysis results in the flooding test solution by ICP-OES for coal BH2 are summarized in Appendix Table 3.

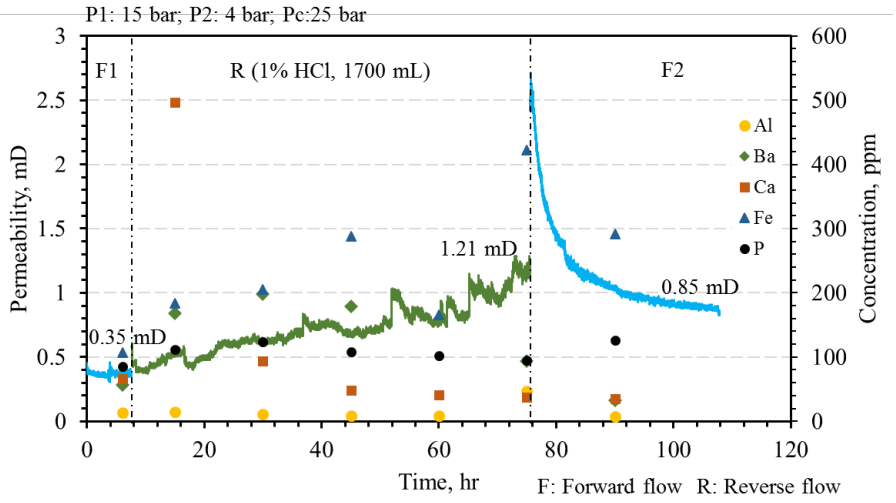

Figure 6-10. Permeability variation in 1% HCl stimulation for coal BH2. P_1=15 bar, P_2=4bar, P_c=25bar.

After acid stimulation, a forward flow was conducted with an inlet pressure reduced to 10 bar to build the permeability baseline for oxidant stimulation, which was measured as 0.14 mD. Then the 1% NaClO flooding followed, where the reverse permeability reached quite high at the beginning (7.5 mD) and declined to 2.3 mD with a total flooding volume of 1300 mL. The post-stimulation forward flow started from 3.5 mD and ended with 0.71 mD, which was 5 times higher than the pre-oxidation permeability as shown in Figure 6-11.

TOC concentration in the initial forward flow was 31 mg/L and immediately shot up to 108 mg/L and then gradually decreased with the injection of NaClO. In the final brine flow, it was 19 mg/L. This TOC trend for coal BH2 was different from those for coal BV1 and BH1, where the TOC concentration gradually increased in the NaClO injection. The difference is proposed to be caused by the permeability level during the NaClO flooding, which was significantly higher here than that for coal BV1 and BH1. The higher permeability allows the dissolved organic carbon to flow out immediately, while the lower permeability hampers the flowing and delays the detection of dissolved coals. Furthermore, the average TOC concentration for coal BH2 was lower than those for coal BV1 and BH1. This is caused by the massive volume of NaClO flowing through coal BH2, that reduced the average TOC concentration in unit volume (10ml here).

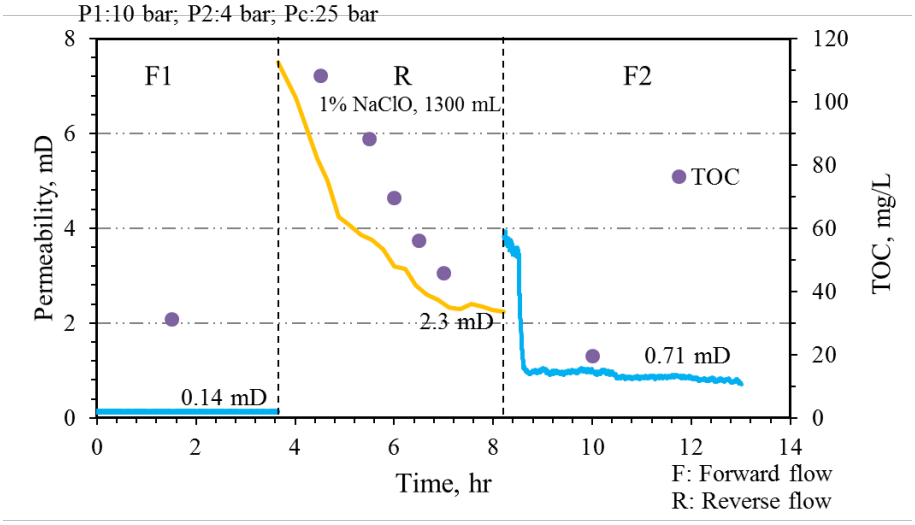

Figure 6-11. Permeability variation in 1% NaClO stimulation for coal BH2. P_1=10 bar, P_2=4bar, P_c=25bar.

6.3.2.3 Cube sample BH3

All the samples described above underwent both the acid stimulation and subsequently oxidant stimulation. Most of them showed the detrimental effect of oxidation on permeability, regardless of the permeability direction, except for coal BH2, which contained a significantly high mineral content. This phenomenon indicated that minerals might play significant contribution to the oxidant stimulation. Therefore, for coal BH3, only oxidant flowed through the coal to keep its minerals intact. Figure 6-12 shows the horizontal permeability variation during the single oxidant simulation. The initial permeability was 1.95 mD, which dropped to

0.62 mD at the beginning of oxidation, and after one hour flowing, the permeability suddenly shot up to 8.2 mD and fluctuated around 8.2 mD. Afterwards, the forward permeability was 6.84 mD, 4.38 times of permeability in the initial forward flow.

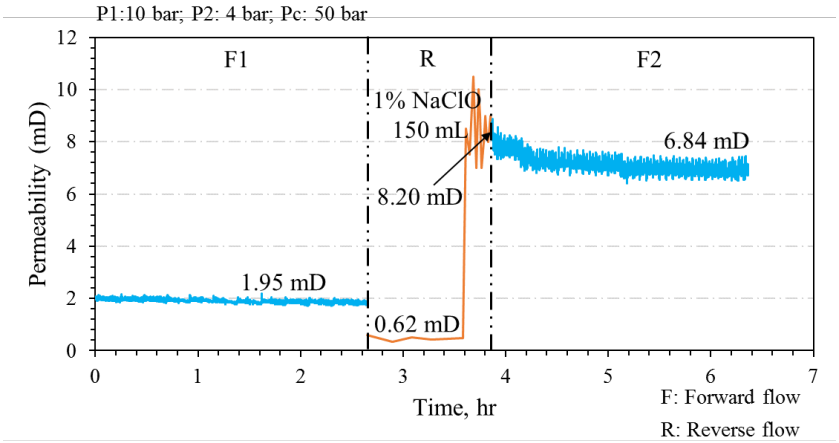

Figure 6-12. Permeability variation during 1% NaClO oxidation for coal BH3. P_1=10 bar, P_2=4bar, P_c=25bar.

Coal 3D models and CT images pre/post oxidation for coal BH3 revealed the coal structure changes caused by oxidation as shown in Figure 6-13. Combining the hand sample observation and the 3D model (Figure 6-13a), it could be confirmed that there existed three layers of bright coal and one dull coal band with an initial fracture across coal BH3. The bright coal layer 2 contained some void spaces which might be related to the un-mineralised cleats. After oxidation, as shown in Figure 6-13c, it was also in layer 2 where the void space proportion increased apparently.

Figure 6-13b and Figure 6-13d show the cross section CT images of the initial fracture in dull coal before and after oxidation, respectively. The comparison of these images could identify two fracture feature changes that could benefit the permeability. The first was the increase of fracture aperture. Before oxidation, the fracture apertures were measured as 134 μm and 126 μm for spot 1 and spot 2, respectively, and they were enlarged to 174 μm and 228 μm after oxidation. The second was the extension of the initially exiting fracture, which was illustrated in Figure 6-13d selected by the red rectangle, where a new fracture was generated and connected to the initial fracture.

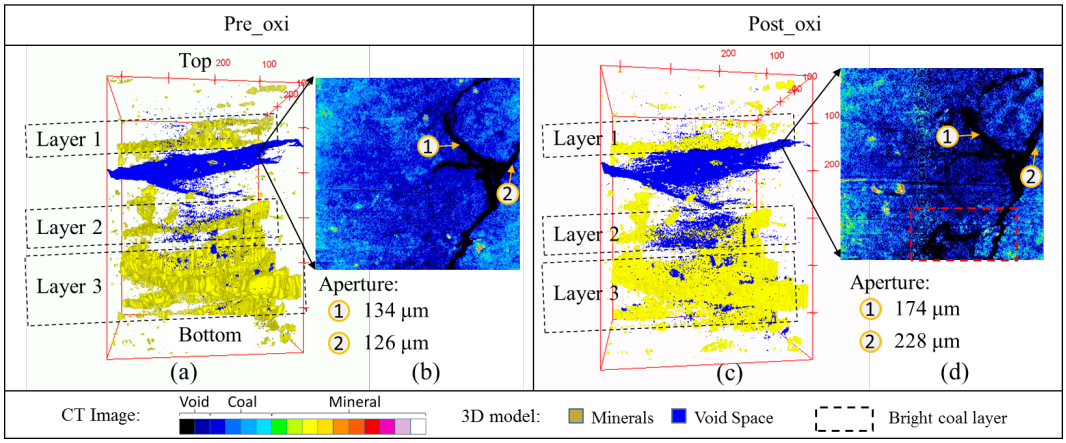

Figure 6-13. Fracture feature change in coal BH3 after 1% NaClO oxidation.

6.4 Discussion

6.4.1 Effect of acid stimulation on horizontal permeability

The horizontal permeability of the two studied cube samples (BH1 and BH2) both increased after acid stimulation. The CT image comparison for coal BH1 before and after oxidation (Figure 6-8) clearly showed the minerals vanished in some parts of the cleats after 1% HCl flooding and the mineral proportion (MF) calculation based on CT images confirmed the demineralizing effect. New void space occurred at the locations where initially existed minerals. These generated void spaces are kept open during the flooding test due to the hydraulic pressure and provided pathways for fluid and thus elevated the permeability during acid stimulation.

The ICP-OES results for the two studied samples confirmed the demineralisation caused by 1% HCl flooding. For both coals, Ca was the main detected element in the effluent, indicating the dissolution of Ca containing minerals including calcite, aparite and ankerite. Combining with the concentrations of other elements, like P and Fe, it is determined that BH1 contained mainly calcite, while in coal BH2, aptite and ankerite also existed in addition to calcite. The Al concentration was detected relatively lower in the effluent for both coals, indicating a scarce distribution of kaolinite in the two studied coals. The mineral types, which were inferred based on the element concentrations in the effluent, agree to the results detected by SEM-EDS previously [11, 181].

The permeability increase for coal BH1 and BH2 is expected. Turner et al. (2016) conducted acid stimulation using coal samples with different mineralisation types [11, 181]. They concluded that the acidizing effect on coal permeability highly depended on the mineral types, that the carbonate dissolution in major cleats could produce permeability increase, while the clay dominate coals showed a permeability decrease.

It is of particular interest that the permeability variation types during acid flooding for the two studied coals, although a final permeability increase were observed for both coals. For coal BH1, the permeability immediately reached its maximum once contacting to HCl and then decreased generally to the final stabilising level, while for coal BH2, the permeability gradually increased with the injection of HCl until its final plateau. This difference is hypothesized to depend on the various mineral types in the two coals, although they both primarily contained carbonate mineralisation. For coal BH1, a possible reason for permeability decline is that although dissolution of minerals (calcite here) allows more liquid into the core, it is not enhancing flow paths, i.e. restrictions to flow in the cleats still exist. Another reason could be destabilisation of slow soluble minerals (e.g. kaolinite), causing them to become mobile fines in the liquid which migrate toward restrictions in the flow and then jam. For coal BH2, except for the massive carbonate minerals, a considerable barite also existed in the coal. The highly distributed barite could hamper the contacting of carbonate with HCl. The successive stages of cleat demineralisation result in a greater proportion mineralised fractures becoming exposed to HCl with continued injection, leading to a stepwise increase in coal BH2 permeability.

The increase of permeability probably benefit significantly from the horizontal direction of acid flooding. This direction is parallel to the face cleats that enables HCl to contact with cleat filled minerals extensively, mainly including carbonate here, and also provides the maximum opportunity for the fines to be flooded out from the coal sample since they do not need to pass through different coal layers, where the cleats always terminate.

6.4.2 Effect of oxidant stimulation on vertical and horizontal permeability

The effect of oxidant stimulation on coal permeability was examined vertically for coal cores and horizontally for coal cubes. After oxidation, the vertical permeability decreased for both

coal cores, while the horizontal permeability decreased for BH1, but increased for BH2 and BH3.

Analysis of CT scanning images enables examination of the coal structure change, especially the key fracture features. The results showed three main changes on coal structures after NaClO oxidation. The first is the increase of void space proportion at the locations where is relatively more porous initially. The second is the generation of new fractures close to the horizontal direction or the extension of existing fractures. The third is the enlargement of fracture apertures as shown in Figure 6-13. Other phenomena might also occur during oxidation, like coal fines generation, but could not be observed due to the resolution of CT scanning (44 μm). All these variations observed tend to favour the permeability increase.

For the coal cores (BV1 and BV2), coal oxidation caused void space proportion soaring and new horizontal fractures appearing in the bright coal bands. However, these potential pathways for fluid did not contribute to the vertical permeability enhancement. It is proposed that the vertical permeability is limited by a low permeable section, where the coal has not been attacked. Furthermore, coal fines generated in the reacted parts may have mobilised to those un-reacted sections and blocked the originally undeveloped pathways. Coal oxidation is likely to generate coal fines, as examined by soaking coal particles in NaClO solution [180].

For the cube sample BH1, CT images also showed massive void space was generated after oxidation (Figure 6-8 and Figure 6-9c), which, however, could not explain the decrease of permeability. CT images for BH2 were not available for the observation of coal structures, but indicated massive mineral contents and most of them were proposed to be barite ($BaSO_4$). The mineral difference in the two samples might be critical for the permeability stimulation effect during oxidation. The two coals both experienced 1% HCl flooding, which dissolved a large number of minerals (from maximum 6% to 0.5% in Figure 6-9b) in cleats for coal BH1 and might destroy its structure integrity. During oxidant flooding, although coal fractures in BH1 were etched and enlarged, the confining pressure may cause the fractures collapsing into newly created cavities and closure of existing fractures with the decline in fluid pressure [10, 184]. By contrast, significant amount of carbonate minerals were also dissolved in coal BH2, however, the considerable barite remained and may maintain the coal integrity. The large amount of barite could also support the cleats as proppants during

the oxidant flooding. To examine this hypothesis, coal BH3 was directly flooded by oxidant without a pre-treatment with acid to keep the minerals intact. The permeability for BH3 increased from initial 1.95 mD to final 6.84 mD (Figure 6-12). The void space proportion in the bright layer 2 was confirmed to be increased (Figure 6-13) and the remaining minerals could protect the cleats from collapsing.

Furthermore, except the minerals, other factors could also affect the permeability during oxidation including specific coal fracture structures, the oxidant volume and contacting time and pressure circumstances. For coal BH1, although the flooding direction was parallel to the face cleats as shown in Figure 6-8, the face cleats terminated in the middle of the coal and connected with another face cleat by a butt cleat. The connection points with a narrow aperture might be the restriction of the permeability increase, because the coal fines could accumulate here and hamper the permeability enhancement. For coal BH3, the face cleats went through the whole sample, making it easier for fluid to flow through without the variation of flowing direction. Besides, a large fracture went through the coal BH3, and the fluid flow rate was quite high, leading to a higher coal fines migration capacity, which likely decreases the possibility for coal fines deposition.

The oxidant volume and its contacting time with coal are important factors. More oxidant and/or longer contacting time might result in over stimulation, because the higher degree of oxidation can soften the coal cleat surface, which could destroy the coal structure integrity. Furthermore, it also generate massive tiny coal fines as imaged previously [180], which could block the fractures. However, optimising the oxidant volume and/or the flooding time is presently difficult due to the significant heterogeneity of coals and it may also depend on the running pressure circumstances of the flooding tests.

The modification of fracture features might be caused by chemical and/or physical reasons. The massive TOC content in the effluent during oxidant flooding tests indicates the chemical attack of NaClO. The swelling test described previously also confirmed the chemical reaction between NaClO and coal causing the coal particle dissolution and breakage [180]. During the core flooding test, when the oxidant flowed through the coal sample, it could etch the original cleat surface widening the cleat aperture and/or dissolve part of the coal generating massive void space and new fractures. This occurred universally in this study. The soft coal with void space under confining pressure might cause the coal break physically, which could be examined by the new fractures for coal BV2, as shown in Figure 6-5f. The massive void

space in the middle might result from chemical dissolution and the new fractures on the left side was likely from squeezing by the confining pressure.

To study the lithotypes where new fractures appear is of particular importance, because it could contribute to optimise the core flooding test but also select the oxidation targets in the future. In this study, the majority of the new fractures and the void space were produced in the bright coal bands. The massive change occurred in the bright coal in this study conflicts with our previous finding that NaClO prefers to attack the dull coal than the bright coal when it flowed through the artificial cleats across both bright coal and dull coal [179]. To examine this confliction, the void space fractions for each coal before and after oxidation were analysed and we found that the NaClO oxidation seems to occur at the locations where high void space exists. It means that in the same coal sample, the NaClO oxidation is lithotype independent and the NaClO would attack any coal types as long as it can come to contact. For example, in coal BH3, where a fracture existed in the dull coal band, and coal oxidation not only widened the fracture aperture, but also produced a new fracture as shown in Figure 6-13. This could be further confirmed chemically by the molecular fractures of vitrinite and inertinite. It is reported that vitrinite and inertinite share the similar molecular structures in the same rank coal [27, 32].

6.5 Conclusion

To enhance coal seam permeability, acid stimulation (1% HCl) and oxidant stimulation (1% NaClO) were both examined in this chapter. The core flooding test could measure the permeability variation during the stimulation procedure, while the CT scanning technique allows to compare the coal structure change after stimulations. The effluent from the core flooding test rig was collected and analysed with ICP-OES and TOC to examine the chemical reaction happened during the stimulation procedure. Combining all the results and analyses, we have the conclusions as follows:

1. Acid stimulation can enhance the horizontal coal permeability through demineralisation evidenced by CT scanning observation and higher element concentration in the effluent.

2. NaClO oxidation can widen coal fracture aperture and generate horizontal fractures and/or void space. These changes could be caused primarily by chemical attack, confirmed by the high TOC concentration in the effluent.
3. Oxidant stimulation decreased the vertical permeability, which is proposed to be the loss of coal structural integrity.
4. Oxidant stimulation has the potential to increase horizontal permeability and minerals appears to play an important role in the permeability enhancement.
5. NaClO oxidation is lithotype independent and it attacks the coal section that is more porous or contains initial fractuers.

This chapter shows the potential of both acid stimulation and oxidant stimulation to increase coal seam permeability. Their mechanism of permeability enhancement are analysed and discussed. Acid stimulation appears to target at minerals, but the oxidant stimulation prefers to attack coal matrix with the existing fractures or the vacancy in the coal sample. Interestingly, minerals also play significant contribution to the oxidant stimulation results. Some questions still need to be answered such as the optimised oxidant volume and contacting time, which is difficult to test, because the permeability enhancement results depend on a number of factors including coal types, mineral types and contents, pressures and even temperatures. The high coal heterogeneity makes it harder. In the future, the oxidant stimulation targeting at different coal types need to be conducted.

Chapter 7. Conclusion and recommendation

7.1 Conclusions

The research objectives outlined in Chapter 1 have been largely accomplished, with some additional investigations required to scale up to a reservoir treatment. In this study, two samples were used (coal B and coal S). High volatile A bituminous (Coal B) and subbituminous (Coal S) coal drill cores were collected from the Bandanna Formation in Bowen Basin and the Walloon Subgroup from Surat Basin, respectively. The main findings of this research are concluded as follows.

The project started with the screening of potentially useful oxidants for coal seam gas application based on both samples. This was achieved by a time-lapse photography-image analysis test combined with leaching test in oxidising solutions. Coal particles (3-4mm) and coal powders (75-212 μm) were used in swelling test and leaching test, respectively. Four oxidants were tested in the study, including NaClO, $KMnO_4$, $K_2S_2O_8$ and H_2O_2. Coal reacted vigorously with NaClO and $KMnO_4$, but slightly with $K_2S_2O_8$ and H_2O_2. After a certain amount of swelling, coal particle breakage was observed (1% and 10% NaClO and 3% and 5% $KMnO_4$). Massive coal solubilisation appears to happen in NaClO and $KMnO_4$, but negligible in $K_2S_2O_8$ and H_2O_2. During $KMnO_4$ oxidation, MnO_2 precipitated as solid particles, which may block the coal cleats when $KMnO_4$ is used as a stimulant in permeability test. Therefore, NaClO was determined as more promising than $KMnO_4$, $K_2S_2O_8$ and H_2O_2, given its high reactivity with coal and water-soluble oxidative products.

In NaClO solution, small coal particles (3-4 mm) for coal B showed coal swelling, while for coal S the particle size decreased. Anisotropic swelling was clearly observed for coal B. Both coals exhibited coal dissolution and breakage. The coal swelling toward to cleats may decrease the cleat aperture and damage the coal permeability, while the dissolution may etch the cleat surface and widen the cleat aperture. For the *in-situ* application in which coal is confined, it was initially unclear if coal swelling and/or coal dissolution would occur and whether there would be an increase or decrease in permeability. In addition, coal breakage

may lead to new void space or new cracks in the coal matrix, which has the potential to increase the coal permeability.

To examine the net effect of coal swelling, dissolution and breakage on coal pores and cleats, a series of experiments were involved including Mercury Intrusion Porosimetry (MIP), Scanned Electron Microscopy (SEM), Optical Microscopy, and a Cleat Flow Cell (CFC). MIP results showed that NaClO oxidation appears to increase the coal particle (3-4 mm) porosity by enlarging the pore size for both coals. The pore size distribution indicated that the number of small pores declined after oxidation, while the number of big pores rose. The SEM illustrated the pore enlargement, especially for coal S. The pore enlargement is proposed to benefit the matrix permeability by increasing the pore connectivity.

The photomicrographs illustrated the change of coal structures under fluorescent light and showed the etching of coal particles (3-4 mm) with clear reacted fringes in the cracks. For a larger scale coal sample (15 mm length), CFC measured the artificial cleat aperture increase on the natural coal surface, especially for lower rank coal S. The CFC results showed the predominant effect of coal dissolution, rather than coal swelling when the oxidant flows through fractures. It is of particular interest that NaClO etched more inertinite (semi-fusinite) than vitrinite. It is proposed that the enhanced reactivity of semi-fusinite is due to its porous structure allowing more oxidant into react. Aperture increases of a natural fracture were also observed which offers confidence of the potential positive effect of oxidation on enhancing connectivity through coal cleat system.

The change in the coal structure after oxidation is proposed to be caused by coal swelling and dissolution. The coal structure is relaxed by oxidant penetration resulting in larger coal pores. The enlargement of coal pores might release some initially trapped substances to further increase the coal porosity. Furthermore, NaClO could dissolve coals to generate a series of water-soluble products, and the removal of these products could generate new void spaces and widen coal cleats.

In terms of the oxidative effect on different coal types, the lower rank coal S was found to be more reactive toward NaClO than coal B according to the larger proportion of mass loss and TOC in solute filtrate, the larger pore size increase degree, and the more obvious cleat aperture increase.

To understand the difference in the reaction between NaClO and different coals, ATR-FTIR, XPS and ^{13}C NMR were used to measure the molecular structures of the two coals and their oxidised residues. Based on the results, the schematic models of the two coals and the residues were established. The main features of the lower rank coal S are less aromatic, more aliphatic and higher oxygen content. The oxidation mechanism could be summarised that NaClO preferentially reacts with aliphatic chains, particularly with oxygen functional groups, evidenced by coal S being more reactive. In terms of attacking aromatic clusters, NaClO tends to react with small aromatic rings first, evidenced by the loss of smaller clusters in coal S, remaining the larger aromatic clusters. Then it is able to attack the larger aromatic clusters, confirmed by the cluster size decrease for coal B.

After NaClO oxidation, the aromaticity drops for both coals, suggesting the reaction between NaClO and benzene rings. The breakage of the aromatic rings leads to the longer aliphatic chains in the oxidised coal residues. NaClO oxidation products are rich in C=O and O-C=O, detected for both coals.

The oxidation of higher rank coal B produced a residual structure similar to lower rank coal S, and a second oxidation of oxidised coal B resulted in a similar mass loss (42.5%) with that for coal S (45%). This work has shown that coals from both the Bowen and Surat basin react to the same degree with NaClO. The Bowen coal just takes longer to reach the same extent of reaction. In addition, this work has shown the potential of NaClO to react with essentially the whole coal.

This new knowledge on the NaClO oxidation mechanism, especially the reactivity of different coals can be used to guide selection of stimulation targets and facilitate the formation water treatment after oxidation. It could also benefit other related areas such as coal molecular structure investigation and valuable organic substances extraction from coal by oxidation.

Finally, the stimulation potential of NaClO on permeability was evaluated and the permeability variation mechanism was investigated accordingly. An updated core flooding test and micro CT scanning were used to measure the permeability change and the coal structure change, respectively.

Prior to the oxidant flooding test, the coal samples were flooded with acid (1% HCl), because previous research on acid stimulation only measured the vertical permeability, instead of a

more realistic horizontal permeability. In the horizontal permeability measurement, 1% HCl flooding test was conducted with cube samples (40 mm in length). The results showed that acid stimulation can enhance the horizontal coal permeability through demineralisation evidenced by μCT scanning observation and higher element concentration, particularly calcium (Ca) in the effluent. Across the two cube samples (BH1 and BH2) exposed to acid stimulation, the permeability increased 10 times for BH1, and 3 times for BH2.

In terms of the oxidant stimulation, the permeability variation was measured in two directions, vertically and horizontally, using coal core samples (76 mm in diameter) and cube samples (40 mm in length), respectively. For the two coal core samples, vertical permeability decreased after NaClO flooding. The permeability of one sample decreased from initial 2.01 mD to 0.17 mD, while for the other, the permeability decreased 2.3 times from 0.59 mD to 0.14 mD. μCT scanning results showed that the coal core were partly oxidised along the axis. In the bright coal section, horizontal fractures following the bright coal layers and massive void spaces were generated, while in the dull coal section, oxidative effects were barely detected. It has already been found that low permeability regions (bedding layers or bottlenecks with in cleat structure) dictate the bulk permeability measure. The worse could be that the coal fines generated by oxidation mobilised to these unreacted sections and plugged the originally undeveloped fracture system.

However, oxidant stimulation have shown the potential to increase horizontal permeability in the presence of minerals. Three cube samples were used in the study, of which two were flooded with 1% HCl (BH1, BH2) first, while the third one was a raw sample (BH3) with intact minerals. The permeability for BH1 decreased, although the μCT scanning showed that void space fraction increased and the horizontal cleat widened. The dramatic decrease in permeability could be due to coal swelling into the restricted regions in cleats. It was not possible to observe this as it would be occurring below the resolution limit of the μCT scanning (44 μm). Furthermore, the dissolution may have softened the coal and allowed to collapse in a void space under the confining pressure. As the μCT scanning was conducted without confining pressure, an open cleat shown by the μCT scanning may be closed under the confining pressure during the experiments. Additionally, the coal fines blockage of the bottleneck caused by coal breakage could also damage the permeability.

In contrast, the horizontal permeability for BH2 increased from 0.35 mD to 0.85 mD. This sample was characterised as containing massive minerals, especially the barite which is

known not to dissolve in 1% HCl. It is proposed that the barite or other undissolved minerals might work as pillars in coal cleats that prevent the cleat from collapsing under confining pressure. To investigate this hypothesis, the raw coal sample BH3 was flooded with NaClO and the permeability increased 3.5 times from 1.95 mD to 6.84 mD. This indicates that minerals may play important role in the oxidant stimulation. It should be noted that the importance of minerals should be further investigated due to the scarcity of sample numbers in the current study and the highly heterogeneous property of coals. In this coal sample, there initially existed two sections of void space, of which, one is a fracture across the sample in the dull coal band and the other section is in the bright coal band with unmineralised cleats. In dull coal band, μCT showed that the fracture aperture increased and a new fracture generated connecting to the initial one, while in the bright coal band, void space fraction increased in the area where void space initially existed. The increased fracture aperture and connectivity could provide more pathways for the fluid and thus increase the permeability. The change of coal structures occurs at the areas that are initially more porous, because these porous areas have more pathways for the oxidant to penetrate and allow reaction.

Given the fact that NaClO reacted more significantly with dull coal bands in CFC test, but more with bright coal bands in core flooding tests, it could be concluded that NaClO oxidation is lithotype independent. It attacks the coal sections that are originally more porous or contain initial fractures. Because in the same coal sample, the molecular structures of initinite and vitrinite are similar, although inertinite is slightly more aromatic and the surface area determines the degree of reaction.

To further explore the oxidant stimulation of coal seams to increase permeability, more research with elaborately characterised samples are recommended to build a relationship between coal properties and permeability change, and to study the kinetics of the stimulation procedure. A detailed recommendation for further study is listed below.

7.2 Recommendations

This thesis has identified the potential of oxidant stimulation to both enhance and damage the permeability of coal. The thesis results and conclusions lead to several

recommendations to continue this research and the recommendations could, in turn, benefit the understanding of oxidant stimulation for enhancing coal seam permeability.

1. Flooding test with lower rank coal S

The results in this thesis showed that lower rank coal S had more drastic reaction with aqueous NaClO, representing as higher mass loss and TOC concentration in the filtrate. The artificial cleat aperture of coal S could be widened significantly by oxidation. Therefore, the oxidant flooding test with coal S is expected to have a strong potential to increase permeability.

2. Fixed volume coal flooding test

The flooding test in this thesis was conducted with uniform axial confining pressure, which may have subjected unrealistic pressures. Establishing core floods where only overburden pressure is applied is strongly recommended. Therefore the confining pressure set in the current experiment should be modified, which, however, is limited by the structure of core holder. Therefore, a fixed volume coal flooding test is recommended. Because if the coal volume is fixed, the cleat wall would keep stable and this will directly show the etching effect on coal permeability without the influence of confining pressure.

3. Characterization of produced coal fines

The abrupt change in permeability during the acid injection period suggests a sudden release of clay fines (by mineral dissolution) that may or may not be constrained by restrictions in the cleat network, thereby leading to permeability enhancement or decline. This could also likely occur in oxidant stimulation, where the coal dissolution could generate coal fines. It is possible that clay and coal fines are emitted from the core outlet in very low concentrations. Characterisation of these produced fines by particle counting, X-ray diffraction (XRD) and SEM-EDS methods would enable a greater understanding of the contribution of fines migration to permeability decline.

The influence of flow velocity may also be investigated, especially in the oxidant stimulation. Because the water-soluble oxidative product could change the flow velocity, which can directly influence the permeability calculation.

5. Kinetic study of the stimulation procedure and the coal sample characterization

In the current flooding test, the experimental temperature effect on the oxidation results was not investigated. Besides, the volume of aqueous NaClO flowing through coal sample and its contacting time with coal were not controlled, and this might under or over stimulate the coal. Because if the NaClO/coal ratio is low, the cleat aperture could not be fully etched, and its permeability enhancing potential would be underestimated. If too much NaClO, especially with concentrated NaClO injected into the sample, the coal structure might be softened and it would be easier to destroy the coal integrity under confining pressure.

Furthermore, the current CT scanning resolution is 44 μm, which is not precise enough to characterise the coal structure change after stimulation. Some tiny, but important to the coal permeability changes would become vague, hampering the explanation of the permeability change. The higher resolution of coal structure examination could facilitate the study of coal heterogeneity. Establishing relationships between permeability change and coal property information is strongly recommended.

6. Molecular structure study of different coal lithotypes

It is observed that NaClO preferred to etch the coal cleat surface in the dull coal band in the cleat flow cell, but in the flooding test, it attacked primarily the bright coal. This conflict was finally explained as NaClO oxidation did not have preference on particular coal lithotypes, and the different oxidation phenomena depended on the void space proportion at the specific coals, rather than their different molecular structures. Therefore, it is of importance to investigate the molecular structures of different coal lithoypes to confirm the expiation. The improved understanding of NaClO oxidation with different coal lithotypes could benefit the selection of oxidant stimulation targets in the future.

7. Coal oxidation with other oxidants under different conditions

Although $KMnO_4$, H_2O_2, $K_2S_2O_8$ have been extensively studied in this thesis, the swelling tests and leaching tests were conducted at uncontrolled conditions. However, the experimental condition might have significant influence on the oxidant activity, including temperature, solution pH. Besides, except for the oxidants used in the current thesis, there

might exist other valuable oxidants that could have interesting results with respect to oxidant stimulation.

Bibliography

1. Underschultz, J., *Chapter 28 Unconventional Gas, in ed. Sheila Devasahayam, Kim Dowling, and Manoj Mahapatra. Sustainability in the Mineral/Energy Sectors*. 2016: CRC Press. 730.
2. Moore, T.A., *Coalbed methane: a review.* International Journal of Coal Geology, 2012. **101**: p. 36-81.
3. Osisanya, S.O. and R.F. Schaffitzel. *A review of horizontal drilling and completion techniques for recovery of coalbed methane*. in *International Conference on Horizontal Well Technology*. 1996. Society of Petroleum Engineers.
4. Palmer, I. *Review of coalbed methane well stimulation*. in *International Meeting on Petroleum Engineering*. 1992. Society of Petroleum Engineers.
5. Palmer, I.D., Z.A. Moschovidis, and J.R. Cameron. *Coal failure and consequences for coalbed methane wells*. in *SPE Annual Technical Conference and Exhibition*. 2005. Society of Petroleum Engineers.
6. Olsen, T.N., et al. *Application of Indirect Fracturing for Efficient Stimulation of Coalbed Methane*. in *Rocky Mountain Oil & Gas Technology Symposium*. 2007. Society of Petroleum Engineers.
7. Puri, R., G. King, and I. Palmer. *Damage to coal permeability during hydraulic fracturing*. in *Low Permeability Reservoirs Symposium*. 1991. Society of Petroleum Engineers.
8. Salmachi, A. and M. Haghighi, *Feasibility Study of Thermally Enhanced Gas Recovery of Coal Seam Gas Reservoirs Using Geothermal Resources.* Energy & Fuels, 2012. **26**(8): p. 5048-5059.
9. Turner, L.G., K.M. Steel, and S. Pell. *Novel chemical stimulation techniques to enhance coal permeability for coal seam gas extraction*. in *SPE 13URCE: Unconventional Resources Conference and Exhibition-Asia Pacific 2013*. 2013. Society of Petroleum Engineers (SPE).
10. Balucan, R.D., L.G. Turner, and K.M. Steel, *Acid-induced mineral alteration and its influence on the permeability and compressibility of coal.* Journal of Natural Gas Science and Engineering, 2016. **33**: p. 973-987.
11. Turner, L.G. and K.M. Steel, *A study into the effect of cleat demineralisation by hydrochloric acid on the permeability of coal.* Journal of Natural Gas Science and Engineering, 2016. **36**: p. 931-942.
12. Vasyuchkov, Y.F., *A study of porosity, permeability, and gas release of coal as it is saturated with water and acid solutions.* Journal of Mining Science, 1985. **21**(1): p. 81-88.
13. Balucan, R.D., L.G. Turner, and K.M. Steel, *X-ray μCT investigations of the effects of cleat demineralization by HCl acidizing on coal permeability.* Journal of Natural Gas Science and Engineering, 2018. **55**: p. 206-218.
14. Ramandi, H.L., et al., *Impact of dissolution of syngenetic and epigenetic minerals on coal permeability.* Chemical Geology, 2018. **486**: p. 31-39.
15. Chakrabartty, S. and H. Kretschmer, *Studies on the structure of coals: Part 1. The nature of aliphatic groups.* Fuel, 1972. **51**(2): p. 160-163.
16. Mayo, F.R., *Application of sodium hypochlorite oxidations to the structure of coal.* Fuel, 1975. **54**(4): p. 273-275.
17. Liu, F.-J., et al., *Investigation on structural features of Shengli lignite through oxidation under mild conditions.* Fuel, 2013. **109**: p. 316-324.
18. Vasilakos, N. and C. Clinton, *Chemical coal beneficiation with aqueous hydrogen peroxide/sulfuric acid solutions.* Prepr. Pap., Am. Chem. Soc., Div. Fuel Chem.;(United States), 1983. **28**(CONF-830814-Vol. 3).
19. Borah, D., M.K. Baruah, and I. Haque, *Oxidation of high sulphur coal. Part 2. Desulphurisation of organic sulphur by hydrogen peroxide in presence of metal ions.* Fuel, 2001. **80**(10): p. 1475-1488.
20. Liu, F.-J., et al., *Oxidation of Shengli lignite with aqueous sodium hypochlorite promoted by pretreatment with aqueous hydrogen peroxide.* Fuel, 2013. **111**: p. 211-215.

21. Wang, Y.-G., et al., *Sequential oxidation of Jincheng No. 15 anthracite with aqueous sodium hypochlorite.* Fuel Processing Technology, 2014. **125**: p. 182-189.
22. Carlson, G., *Computer simulation of the molecular structure of bituminous coal.* Energy & fuels, 1992. **6**(6): p. 771-778.
23. Mathews, J.P. and A.L. Chaffee, *The molecular representations of coal–a review.* Fuel, 2012. **96**: p. 1-14.
24. Marzec, A., *Towards an understanding of the coal structure: a review.* Fuel Processing Technology, 2002. **77**: p. 25-32.
25. Wender, I., *Catalytic synthesis of chemicals from coal.* Catalysis Reviews—Science and Engineering, 1976. **14**(1): p. 97-129.
26. Pappano, P.J., J.P. Mathews, and H.H. Schobert, *Structural determinations of Pennsylvania anthracites.* Carbon, 1999. **3**(4.5): p. 6.7.
27. Van Niekerk, D., et al., *Structural characterization of vitrinite-rich and inertinite-rich Permian-aged South African bituminous coals.* International Journal of Coal Geology, 2008. **76**(4): p. 290-300.
28. Nishioka, M., *The associated molecular nature of bituminous coal.* Fuel, 1992. **71**(8): p. 941-948.
29. Van Niekerk, D. and J.P. Mathews, *Molecular representations of Permian-aged vitrinite-rich and inertinite-rich South African coals.* Fuel, 2010. **89**(1): p. 73-82.
30. Iino, M., *Network structure of coals and association behavior of coal-derived materials.* Fuel processing technology, 2000. **62**(2): p. 89-101.
31. Chen, Y., M. Mastalerz, and A. Schimmelmann, *Characterization of chemical functional groups in macerals across different coal ranks via micro-FTIR spectroscopy.* International Journal of Coal Geology, 2012. **104**: p. 22-33.
32. Okolo, G.N., et al., *Chemical–structural properties of South African bituminous coals: insights from wide angle XRD–carbon fraction analysis, ATR–FTIR, solid state 13 C NMR, and HRTEM techniques.* Fuel, 2015. **158**: p. 779-792.
33. Mathews, J.P., P.G. Hatcher, and A.W. Scaroni, *Proposed model structures for Upper Freeport and Lewiston-Stockton vitrinites.* Energy & fuels, 2001. **15**(4): p. 863-873.
34. Faulon, J.L., G.A. Carlson, and P.G. Hatcher, *Statistical models for bituminous coal: a three-dimensional evaluation of structural and physical properties based on computer-generated structures.* Energy & fuels, 1993. **7**(6): p. 1062-1072.
35. Patrakov, Y.F., V. Kamyanov, and O. Fedyaeva, *A structural model of the organic matter of Barzas liptobiolith coal.* Fuel, 2005. **84**(2): p. 189-199.
36. Moore, T.A., *The Enigma of The Pinang Dome (Kalimantan Timur): a review of its origin, significance and influence on coal rank and coalbed methane properties.* 2013.
37. Gan, H., S. Nandi, and P. Walker, *Nature of the porosity in American coals.* Fuel, 1972. **51**(4): p. 272-277.
38. Senel, I.G., et al., *Characterization of pore structure of Turkish coals.* Energy & fuels, 2001. **15**(2): p. 331-338.
39. Yao, S., et al., *An atomic force microscopy study of coal nanopore structure.* Chinese Science Bulletin, 2011. **56**(25): p. 2706-2712.
40. Rodrigues, C. and M.L. De Sousa, *The measurement of coal porosity with different gases.* International Journal of Coal Geology, 2002. **48**(3): p. 245-251.
41. Parkash, S. and S. Chakrabartty, *Microporosity in Alberta plains coals.* International journal of coal geology, 1986. **6**(1): p. 55-70.
42. Levine, J.R., *Model study of the influence of matrix shrinkage on absolute permeability of coal bed reservoirs.* Geological Society, London, Special Publications, 1996. **109**(1): p. 197-212.
43. Zhang, S., et al., *The characteristics of coal reservoir pores and coal facies in Liulin district, Hedong coal field of China.* International Journal of Coal Geology, 2010. **81**(2): p. 117-127.
44. Lin, W., *Gas sorption and the consequent volumetric and permeability change of coal*. 2010.
45. Bustin, R. and C. Clarkson, *Geological controls on coalbed methane reservoir capacity and gas content.* International Journal of Coal Geology, 1998. **38**(1): p. 3-26.
46. Dawson, G. and J. Esterle, *Controls on coal cleat spacing.* International Journal of Coal Geology, 2010. **82**(3): p. 213-218.

47. Solano-Acosta, W., M. Mastalerz, and A. Schimmelmann, *Cleats and their relation to geologic lineaments and coalbed methane potential in Pennsylvanian coals in Indiana.* International Journal of Coal Geology, 2007. **72**(3): p. 187-208.
48. Wang, G., P. Massarotto, and V. Rudolph, *An improved permeability model of coal for coalbed methane recovery and CO 2 geosequestration.* International Journal of Coal Geology, 2009. **77**(1): p. 127-136.
49. Close, J.C. and M.J. Mavor, *Influence of Coal Composition and Rank on Fracture Development in Fruitland Coal Gas Reservoirs of.* 1991.
50. Laubach, S., et al., *Characteristics and origins of coal cleat: a review.* International Journal of Coal Geology, 1998. **35**(1): p. 175-207.
51. Tremain, C.M., S.E. Laubach, and N.H. Whitehead III, *Coal fracture (cleat) patterns in Upper Cretaceous Fruitland formation, San Juan Basin, Colorado and New Mexico-implications for coalbed methane exploration and development.* 1991.
52. Flores, R.M., *Coal and coalbed gas: fueling the future*. 2013: Newnes.
53. Law, B., *The relationship between coal rank and cleat density—A preliminary report (abstr.): American Association of Petroleum Geologists Bulletin, v. 75.* 1991.
54. Law, B. *The relationship between coal rank and cleat spacing: implications for the prediction of permeability in coal*. in *Proceedings of the 1993 International Coalbed Methane Symposium*. 1993. Twscaloosa, ALabma: University of ALabama.
55. Secor, D.T., *Role of fluid pressure in jointing.* American Journal of Science, 1965. **263**(8): p. 633-646.
56. Ryan, B. and N.V. Branch, *Cleat development in some British Columbia coals.* Geological fieldwork, 2002: p. 2003-1.
57. Flores, R.M., *Styles of coal deposition in Tertiary alluvial deposits, Powder River Basin, Montana and Wyoming.* Geological Society of America Special Papers, 1986. **210**: p. 79-104.
58. Mazumder, S., et al., *Application of X-ray computed tomography for analyzing cleat spacing and cleat aperture in coal samples.* International Journal of Coal Geology, 2006. **68**(3): p. 205-222.
59. Close, J.C., *Natural Fractures in Coal: Chapter 5.* 1993.
60. Yao, Y., et al., *Fractal characterization of adsorption-pores of coals from North China: an investigation on CH 4 adsorption capacity of coals.* International Journal of Coal Geology, 2008. **73**(1): p. 27-42.
61. McCulloch, C.M., M. Deul, and P.W. Jeran, *Cleat in bituminous coalbeds*. 1974: US Department of the Interior, Bureau of Mines.
62. Bilgesu, H.I. and M. Ali. *Well-completion strategies for methane gas production from coal seams using simulation*. in *SPE Eastern Regional Meeting*. 2005. Society of Petroleum Engineers.
63. Gentzis, T., N. Deisman, and R.J. Chalaturnyk, *Effect of drilling fluids on coal permeability: impact on horizontal wellbore stability.* International Journal of Coal Geology, 2009. **78**(3): p. 177-191.
64. Flores, R.M., *Coal Composition and Reservoir Characterization-Chapter 5.* 2014.
65. Methane, C., *Principles and Practice, Rogers, Rudy E*. 1994, Prentice-Hall, Inc.
66. Seidle, J., *Fundamentals of coalbed methane reservoir engineering*. 2011: PennWell Books.
67. Li, Q., et al., *A Review on Hydraulic Fracturing of Unconventional Reservoir.* Petroleum, 2015.
68. Kravits, S. and G. DuBois, *Horizontal Coalbed Methane Wells Drilled from Surface.* Coal Bed Methane: From Prospect to Pipeline, 2014: p. 137.
69. Kalfayan, L., *Production enhancement with acid stimulation*. 2008: Pennwell Books.
70. Steel, K.M., S. Pell, and L.G. Turner. *Novel chemical stimulation techniques to enhance coal permeability for coal seam gas extraction*. in *SPE Unconventional Resources Conference and Exhibition-Asia Pacific*. 2013. Society of Petroleum Engineers.
71. Tsitonaki, A., et al., *In situ chemical oxidation of contaminated soil and groundwater using persulfate: a review.* Critical Reviews in Environmental Science and Technology, 2010. **40**(1): p. 55-91.

72. Yao, Z.-S., et al., *Oxidation of Shenfu coal with RuO4 and NaOCl.* Energy & Fuels, 2010. **24**(3): p. 1801-1808.
73. Miura, K., et al., *New oxidative degradation method for producing fatty acids in high yields and high selectivity from low-rank coals.* Energy & Fuels, 1996. **10**(6): p. 1196-1201.
74. Larsen, J.W., et al., *Multiple mechanisms for the loss of coking properties caused by mild air oxidation.* Fuel, 1986. **65**(4): p. 595-596.
75. Maloney, D.J., R.G. Jenkins, and P.L. Walker, *Low-temperature air oxidation of caking coals. 2. Effect on swelling and softening properties.* Fuel, 1982. **61**(2): p. 175-181.
76. Chuang, K.-C., R. Markuszewski, and T. Wheelock, *Desulfurization of coal by oxidation in alkaline solutions.* Fuel Processing Technology, 1983. **7**(1): p. 43-57.
77. Li, W. and E.H. Cho, *Coal desulfurization with sodium hypochlorite.* Energy & fuels, 2005. **19**(2): p. 499-507.
78. Smith, A.C. and C.P. Lazzara, *Spontaneous combustion studies of US coals.* 1987.
79. Baris, K., S. Kizgut, and V. Didari, *Low-temperature oxidation of some Turkish coals.* Fuel, 2012. **93**: p. 423-432.
80. Liang, Y., et al., *Characteristics of coal re-oxidation based on microstructural and spectral observation.* International Journal of Mining Science and Technology, 2015.
81. Gallagher, L.K., et al., *The effect of coal oxidation on methane production and microbial community structure in Powder River Basin coal.* International Journal of Coal Geology, 2013. **115**: p. 71-78.
82. Yu, J., et al., *Coal oxidation under mild conditions: current status and applications.* Chemical Engineering & Technology, 2014. **37**(10): p. 1635-1644.
83. Matilainen, A. and M. Sillanpää, *Removal of natural organic matter from drinking water by advanced oxidation processes.* Chemosphere, 2010. **80**(4): p. 351-365.
84. Jones, E.J., et al., *The effect of coal bed dewatering and partial oxidation on biogenic methane potential.* International Journal of Coal Geology, 2013. **115**: p. 54-63.
85. Ferrarese, E., G. Andreottola, and I.A. Oprea, *Remediation of PAH-contaminated sediments by chemical oxidation.* Journal of Hazardous Materials, 2008. **152**(1): p. 128-139.
86. Mae, K., et al., *Extraction of low-rank coals oxidized with hydrogen peroxide in conventionally used solvents at room temperature.* Energy & Fuels, 1997. **11**(4): p. 825-831.
87. Kleiser, G. and F. Frimmel, *Removal of precursors for disinfection by-products (DBPs)—differences between ozone-and OH-radical-induced oxidation.* Science of the total environment, 2000. **256**(1): p. 1-9.
88. Mayo, F.R. and N.A. Kirshen, *Oxidations of coal by aqueous sodium hypochlorite.* Fuel, 1979. **58**(10): p. 698-704.
89. Mayo, F.R., et al., *Extractions and reactions of coals below 100 C: 4. Oxidations of Illinois No. 6 coal.* Fuel, 1988. **67**(5): p. 612-618.
90. Gong, G.-z., X.-y. Wei, and Z.-m. Zong, *Separation and analysis of the degradation products of two coals in aqueous NaOCl solution.* Journal of fuel chemistry and technology, 2012. **40**(1): p. 1-7.
91. Wang, Y.-g., et al., *Mild oxidation of Jincheng NO. 15 anthracite.* Journal of Fuel Chemistry and Technology, 2013. **41**(7): p. 819-825.
92. Zhao, Y., et al., *Oxidation of Lingwu coal extraction residue in aqueous sodium hypochlorite under mild conditions.* Transactions of Tianjin University, 2015. **21**(1): p. 19-25.
93. Dash, S., S. Patel, and B.K. Mishra, *Oxidation by permanganate: synthetic and mechanistic aspects.* Tetrahedron, 2009. **65**(4): p. 707-739.
94. Wang, W., et al., *Reducing polycyclic aromatic hydrocarbons content in coal tar pitch by potassium permanganate oxidation and solvent extraction.* Journal of Environmental Chemical Engineering, 2015. **3**(3): p. 1513-1521.
95. Akyol, N.H. and I. Yolcubal, *In-situ chemical oxidation of residual TCE by Permanganate in Epikarst.* World Acad. Sci. Eng. Technol, 2009. **57**: p. 353-355.
96. Struse, A.M., et al., *Diffusive transport of permanganate during in situ oxidation.* Journal of Environmental Engineering, 2002. **128**(4): p. 327-334.
97. Waldemer, R.H. and P.G. Tratnyek, *Kinetics of contaminant degradation by permanganate.* Environmental science & technology, 2006. **40**(3): p. 1055-1061.

98. Moore, T. and K. Swanson, *Application of etching and SEM in the identification of fossil plant tissues in coal.* Organic geochemistry, 1993. **20**(6): p. 769-777.
99. Pierce, B.S., R.W. Stanton, and C.F. Eble, *Facies development in the Lower Freeport coal bed, west-central Pennsylvania, USA.* International Journal of Coal Geology, 1991. **18**(1-2): p. 17-43.
100. Forsey, S.P., N.R. Thomson, and J.F. Barker, *Oxidation kinetics of polycyclic aromatic hydrocarbons by permanganate.* Chemosphere, 2010. **79**(6): p. 628-636.
101. Brown, G., L. Barton, and B. Thomson, *Permanganate oxidation of sorbed polycyclic aromatic hydrocarbons.* Waste Management, 2003. **23**(8): p. 737-740.
102. Norton, G., et al., *Processing and Utilization of High-Sulfur Coals II*. 1987, Elsevier, New York.
103. e Silva, P.T.d.S., et al., *Potassium permanganate oxidation of phenanthrene and pyrene in contaminated soils.* Journal of hazardous materials, 2009. **168**(2): p. 1269-1273.
104. Glaze, W.H. and J.-W. Kang, *Advanced oxidation processes for treating groundwater contaminated with TCE and PCE: laboratory studies.* Journal (American Water Works Association), 1988: p. 57-63.
105. Watts, R.J. and A.L. Teel, *Treatment of contaminated soils and groundwater using ISCO.* Practice Periodical of Hazardous, Toxic, and Radioactive Waste Management, 2006. **10**(1): p. 2-9.
106. Liang, C., Z.-S. Wang, and C.J. Bruell, *Influence of pH on persulfate oxidation of TCE at ambient temperatures.* Chemosphere, 2007. **66**(1): p. 106-113.
107. Neta, P., et al., *Rate constants and mechanism of reaction of sulfate radical anion with aromatic compounds.* Journal of the American Chemical Society, 1977. **99**(1): p. 163-164.
108. Rodríguez, R.A., C.C. Jul, and D. Gómez-Limón, *The influence of process parameters on coal desulfurization by nitric leaching.* Fuel, 1996. **75**(5): p. 606-612.
109. Alvarez, R., C. Clemente, and D. Gómez-Limón, *The influence of nitric acid oxidation of low rank coal and its impact on coal structure☆.* Fuel, 2003. **82**(15): p. 2007-2015.
110. Alam, H., A. Moghaddam, and M. Omidkhah, *The influence of process parameters on desulfurization of Mezino coal by HNO 3/HCl leaching.* Fuel Processing Technology, 2009. **90**(1): p. 1-7.
111. Pietrzak, R. and H. Wachowska, *Low temperature oxidation of coals of different rank and different sulphur content☆.* Fuel, 2003. **82**(6): p. 705-713.
112. Rodríguez, R.Á., C.C. Jul, and D. Gómez-Limón, *Evolution of the organic sulfur and other components during nitric acid leaching of Mequinenza coal.* Fuel, 1997. **76**(14): p. 1445-1450.
113. Cody Jr, G.D., J.W. Larsen, and M. Siskin, *Anisotropic solvent swelling of coals.* Energy & Fuels, 1988. **2**(3): p. 340-344.
114. Gao, H., et al., *An improved three-dimensional microscope image analysis method for studying solvent swelling of single coal particles.* Energy & Fuels, 2008. **23**(1): p. 342-348.
115. Milligan, J., K. Thomas, and J. Crelling, *Solvent swelling of maceral concentrates.* Energy & fuels, 1997. **11**(2): p. 364-371.
116. Murata, S., et al., *Kinetic study on solvent swelling of coal particles.* Fuel Processing Technology, 2008. **89**(4): p. 434-439.
117. Gao, H., et al., *Statistical distribution characteristics of pyridine transport in coal particles and a series of new phenomenological models for overshoot and nonovershoot solvent swelling of coal particles.* Energy & fuels, 1999. **13**(2): p. 518-528.
118. Van Niekerk, D., et al., *Solvent Swelling Extent of Permian-Aged Vitrinite-and Inertinite-Rich Coals: Experiments and Modeling Using the Perturbed-Chain Statistical Associating Fluid Theory (PC-SAFT).* Energy & Fuels, 2011. **25**(6): p. 2559-2564.
119. Van Niekerk, D., P.M. Halleck, and J.P. Mathews, *Solvent swelling behavior of Permian-aged South African vitrinite-rich and inertinite-rich coals.* Fuel, 2010. **89**(1): p. 19-25.
120. Gao, H., et al., *A novel orthogonal microscope image analysis method for evaluating solvent-swelling behavior of single coal particles.* Energy & fuels, 1998. **12**(5): p. 881-890.
121. Ibarra, J., E. Munoz, and R. Moliner, *FTIR study of the evolution of coal structure during the coalification process.* Organic Geochemistry, 1996. **24**(6): p. 725-735.

122. Liu, F.-J., et al., *Separation and structural characterization of the value-added chemicals from mild degradation of lignites: A review.* Applied Energy, 2016. **170**: p. 415-436.
123. Lv, J.-H., et al., *Insight into the structural features of macromolecular aromatic species in Huolinguole lignite through ruthenium ion-catalyzed oxidation.* Fuel, 2014. **128**: p. 231-239.
124. Murata, S., et al., *Structural analysis of coal through RICO reaction: detailed analysis of heavy fractions.* Fuel, 2001. **80**(14): p. 2099-2109.
125. ISO 7404-5, *Methods for the petrographic analysis of coals—Part 5: Method of determining microscopically the reflectance of vitrinite.* International Organization for Standardization, Geneva, 2009: p. 14 pp.
126. ISO 7404-3, *Methods for the petrographic analysis of coals—Part 5: Method of determining maceral group composition.* International Organization for Standardization,Geneva, 2009: p. 7pp.
127. Larsen, J.W., J.C. Cheng, and C.S. Pan, *Solvent extraction of coals during analytical solvent swelling. A potential source of error.* Energy & fuels, 1991. **5**(1): p. 57-59.
128. Otake, Y. and E.M. Suuberg, *Temperature dependence of solvent swelling and diffusion processes in coals.* Energy & fuels, 1997. **11**(6): p. 1155-1164.
129. Cody, G., et al., *Temperature dependence of the swelling of coals in pyridine.* Energy & fuels, 1992. **6**(6): p. 716-719.
130. Otake, Y. and E.M. Suuberg, *Solvent swelling rates of low rank coals and implications regarding their structure.* Fuel, 1998. **77**(8): p. 901-904.
131. Barati, R. and J.T. Liang, *A review of fracturing fluid systems used for hydraulic fracturing of oil and gas wells.* Journal of Applied Polymer Science, 2014. **131**(16).
132. Rajput, S. and N.K. Thakur, *Chapter 8 - Some Facts, Data Analysis, and Examples*, in *Geological Controls for Gas Hydrate Formations and Unconventionals*. 2016, Elsevier. p. 225-286.
133. Aften, C.W. and R.K. Gabel, *Clay stabilizer*. 1994, Google Patents.
134. Li, X.D. and F.W. Schwartz, *DNAPL mass transfer and permeability reduction during in situ chemical oxidation with permanganate.* Geophysical Research Letters, 2004. **31**(6).
135. Schroth, M.H., et al., *In-situ oxidation of trichloroethene by permanganate: effects on porous medium hydraulic properties.* Journal of Contaminant Hydrology, 2001. **50**(1): p. 79-98.
136. Dimitrijević, M., M. Antonijević, and V. Dimitrijević, *Investigation of the kinetics of pyrite oxidation by hydrogen peroxide in hydrochloric acid solutions.* Minerals engineering, 1999. **12**(2): p. 165-174.
137. Mae, K., et al., *Examination of relationship between coal structure and pyrolysis yields using oxidized brown coals having different macromolecular networks.* Fuel, 2000. **79**(3): p. 417-425.
138. Gamson, P., B. Beamish, and D. Johnson, *Coal microstructure and secondary mineralization: their effect on methane recovery.* Geological Society, London, Special Publications, 1996. **109**(1): p. 165-179.
139. Mahoney, S.A., et al., *The effect of rank, lithotype and roughness on contact angle measurements in coal cleats.* International Journal of Coal Geology, 2017. **179**: p. 302-315.
140. Mahoney, S.A., et al., *Creation of microchannels in Bowen Basin coals using UV laser and reactive ion etching.* International Journal of Coal Geology, 2015. **144**: p. 48-57.
141. Shearer, J. and T. Moore, *Botanical control on banding character in two New Zealand coal beds.* Palaeogeography, palaeoclimatology, palaeoecology, 1994. **110**(1-2): p. 11-27.
142. Harris, L.A. and C.S. Yust, *Transmission electron microscope observations of porosity in coal.* Fuel, 1976. **55**(3): p. 233-236.
143. Clarkson, C.R. and R.M. Bustin, *Variation in micropore capacity and size distribution with composition in bituminous coal of the Western Canadian Sedimentary Basin: implications for coalbed methane potential.* Fuel, 1996. **75**(13): p. 1483-1498.
144. Khorasani, G.K., *Oil-prone coals of the Walloon coal measures, Surat Basin, Australia.* Geological Society, London, Special Publications, 1987. **32**(1): p. 303-310.
145. Pickel, W., et al., *Classification of liptinite–ICCP System 1994.* International Journal of Coal Geology, 2017. **169**: p. 40-61.

146. Wang, S.-H. and P.R. Griffiths, *Resolution enhancement of diffuse reflectance ir spectra of coals by Fourier self-deconvolution: 1. CH stretching and bending modes.* Fuel, 1985. **64**(2): p. 229-236.
147. Ibarra, J. and R. Juan, *Structural changes in humic acids during the coalification process.* Fuel, 1985. **64**(5): p. 650-656.
148. Mastalerz, M. and R.M. Bustin, *Electron microprobe and micro-FTIR analyses applied to maceral chemistry.* International Journal of Coal Geology, 1993. **24**(1-4): p. 333-345.
149. Mastalerz, M. and R. Bustin, *Variation in maceral chemistry within and between coals of varying rank: An electron microprobe and micro‐Fourier transform infra‐red investigation.* Journal of Microscopy, 1993. **171**(2): p. 153-166.
150. Jing, Z., J.R. Underschultz, and K.M. Steel, *Oxidant stimulation for enhancing coal seam permeability: Effects of sodium hypochlorite oxidation on subbituminous and bituminous Australian coals.* International Journal of Coal Geology (in press), 2018.
151. Wang, S., et al., *Investigation of coal components of Late Permian different ranks bark coal using AFM and Micro-FTIR.* Fuel, 2017. **187**: p. 51-57.
152. Tian, B., et al., *FTIR study on structural changes of different–rank coals caused by single/multiple extraction with cyclohexanone and NMP/CS 2 mixed solvent.* Fuel Processing Technology, 2016. **154**: p. 210-218.
153. Chen, Y., et al., *Applications of micro-Fourier transform infrared spectroscopy (FTIR) in the geological sciences—A review.* International journal of molecular sciences, 2015. **16**(12): p. 30223-30250.
154. Li, Z., et al., *Application of attenuated total reflectance micro-Fourier transform infrared (ATR-FTIR) spectroscopy to the study of coal macerals: Examples from the Bowen Basin, Australia.* International Journal of Coal Geology, 2007. **70**(1): p. 87-94.
155. Orrego-Ruiz, J.A., R. Cabanzo, and E. Mejía-Ospino, *Study of Colombian coals using photoacoustic Fourier transform infrared spectroscopy.* International Journal of Coal Geology, 2011. **85**(3): p. 307-310.
156. Lin, R. and G.P. Ritz, *Studying individual macerals using ir microspectrometry, and implications on oil versus gas/condensate proneness and "low-rank" generation.* Organic Geochemistry, 1993. **20**(6): p. 695-706.
157. Mastalerz, M. and R. Bustin, *Application of reflectance micro-Fourier Transform infrared analysis to the study of coal macerals: an example from the Late Jurassic to Early Cretaceous coals of the Mist Mountain Formation, British Columbia, Canada.* International Journal of Coal Geology, 1996. **32**(1-4): p. 55-67.
158. Levi, G., et al., *Probing the chemical nature of surface oxides during coal char oxidation by high-resolution XPS.* Carbon, 2015. **90**: p. 181-196.
159. Gong, B., P.J. Pigram, and R.N. Lamb, *Surface studies of low-temperature oxidation of bituminous coal vitrain bands using XPS and SIMS.* Fuel, 1998. **77**(9-10): p. 1081-1087.
160. Buckley, A. and R. Lamb, *Surface chemical analysis in coal preparation research: complementary information from XPS and ToF-SIMS.* International Journal of Coal Geology, 1996. **32**(1-4): p. 87-106.
161. Kelemen, S., et al., *Characterization of organically bound oxygen forms in lignites, peats, and pyrolyzed peats by X-ray photoelectron spectroscopy (XPS) and solid-state 13C NMR methods.* Energy & fuels, 2002. **16**(6): p. 1450-1462.
162. Wang, B., Y. Peng, and S. Vink, *Diagnosis of the surface chemistry effects on fine coal flotation using saline water.* Energy & Fuels, 2013. **27**(8): p. 4869-4874.
163. Solum, M.S., et al., *13C NMR analysis of soot produced from model compounds and a coal.* Energy & Fuels, 2001. **15**(4): p. 961-971.
164. Solum, M.S., et al., *Characterization of macromolecular structure elements from a Green River oil shale, I. Extracts.* Energy & Fuels, 2013. **28**(1): p. 453-465.
165. Vega, M., et al., *Effect of mild oxidation on the surface chemistry of bituminous coals under different humidity conditions.* International Journal of Coal Geology, 2017.
166. Zhang, Y., et al., *Kinetic study on changes in methyl and methylene groups during low-temperature oxidation of coal via in-situ FTIR.* International Journal of Coal Geology, 2016. **154**: p. 155-164.

167. Guo, Y. and R.M. Bustin, *Micro-FTIR spectroscopy of liptinite macerals in coal.* International Journal of Coal Geology, 1998. **36**(3): p. 259-275.
168. Wang, S., et al., *FTIR and 13C NMR investigation of coal component of late Permian coals from southern China.* Energy & Fuels, 2011. **25**(12): p. 5672-5677.
169. Freitas, J.C., T.J. Bonagamba, and F.G. Emmerich, *13C high-resolution solid-state NMR study of peat carbonization.* Energy & Fuels, 1999. **13**(1): p. 53-59.
170. Erdenetsogt, B.-O., et al., *Solid-state C-13 CP/MAS NMR study of Baganuur coal, Mongolia: Oxygen-loss during coalification from lignite to subbituminous rank.* International Journal of Coal Geology, 2010. **82**(1): p. 37-44.
171. Lin, R. and G.P. Ritz, *Reflectance FT-IR microspectroscopy of fossil algae contained in organic-rich shales.* Applied Spectroscopy, 1993. **47**(3): p. 265-271.
172. Iglesias, M.J., et al., *FTIR study of pure vitrains and associated coals.* Energy & Fuels, 1995. **9**(3): p. 458-466.
173. Lis, G.P., et al., *FTIR absorption indices for thermal maturity in comparison with vitrinite reflectance R 0 in type-II kerogens from Devonian black shales.* Organic Geochemistry, 2005. **36**(11): p. 1533-1552.
174. Thomasson, J., et al., *Attenuated total reflectance infrared microspectroscopy of coal.* Fuel, 2000. **79**(6): p. 685-691.
175. Sun, X., *The investigation of chemical structure of coal macerals via transmitted-light FT-IR microspectroscopy.* Spectrochimica Acta Part A: Molecular and Biomolecular Spectroscopy, 2005. **62**(1): p. 557-564.
176. Solum, M.S., R.J. Pugmire, and D.M. Grant, *Carbon-13 solid-state NMR of Argonne-premium coals.* Energy & Fuels, 1989. **3**(2): p. 187-193.
177. Yang, F., et al., *The relationship between benzene carboxylic acids from coal via selective oxidation and coal rank.* Fuel Processing Technology, 2017. **160**: p. 207-215.
178. Fletcher, T.H., et al., *Characterization of macromolecular structure elements from a Green River oil shale, II. Characterization of pyrolysis products by 13C NMR, GC/MS, and FTIR.* Energy & Fuels, 2014. **28**(5): p. 2959-2970.
179. Jing, Z., J.R. Underschultz, and K.M. Steel, *Oxidant stimulation for enhancing coal seam permeability: Effects of sodium hypochlorite oxidation on subbituminous and bituminous Australian coals.* International Journal of Coal Geology, 2018. **(Submitted)**.
180. Jing, Z., et al., *Oxidant stimulation for enhancing coal seam permeability: Swelling and solubilisation behaviour of unconfined coal particles in oxidants.* Fuel, 2018. **221**: p. 320-328.
181. Turner, L., *Chemical stimulation techniques for increasing the permeability of coal seams.* 2015.
182. Espinoza, D.N., et al., *Natural and induced fractures in coal cores imaged through X-ray computed microtomography—Impact on desorption time.* International Journal of Coal Geology, 2016. **154**: p. 165-175.
183. Ramandi, H.L., et al., *Porosity and permeability characterization of coal: a micro-computed tomography study.* International Journal of Coal Geology, 2016. **154**: p. 57-68.
184. Kumar, H., et al., *Inducing fractures and increasing cleat apertures in a bituminous coal under isotropic stress via application of microwave energy.* International Journal of Coal Geology, 2011. **88**(1): p. 75-82.

Appendices

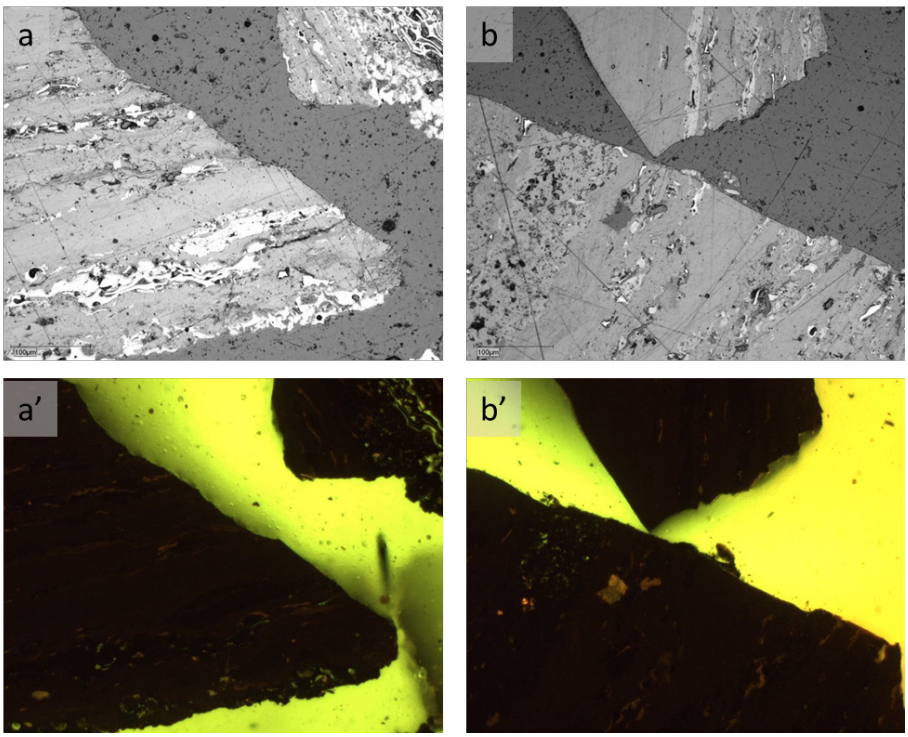

Figure 1. Photomicrographs coal B before treatment. (a) & (b), particle a and particle b, reflected white light; (a') & (b'), particle a and particle b, fluorescent light. Images taken with air objectives (20x).

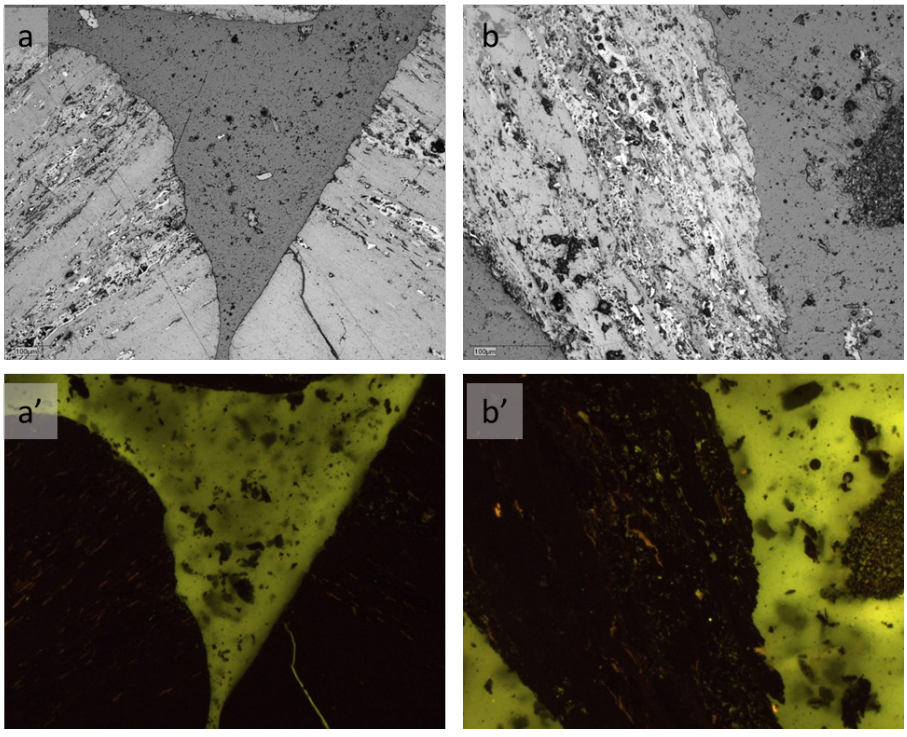

Figure 2. Photomicrographs coal B after treatment. (a) & (b), particle a and particle b, reflected white light; (a') & (b'), particle a and particle b, fluorescent light. Images taken with air objectives (20x).

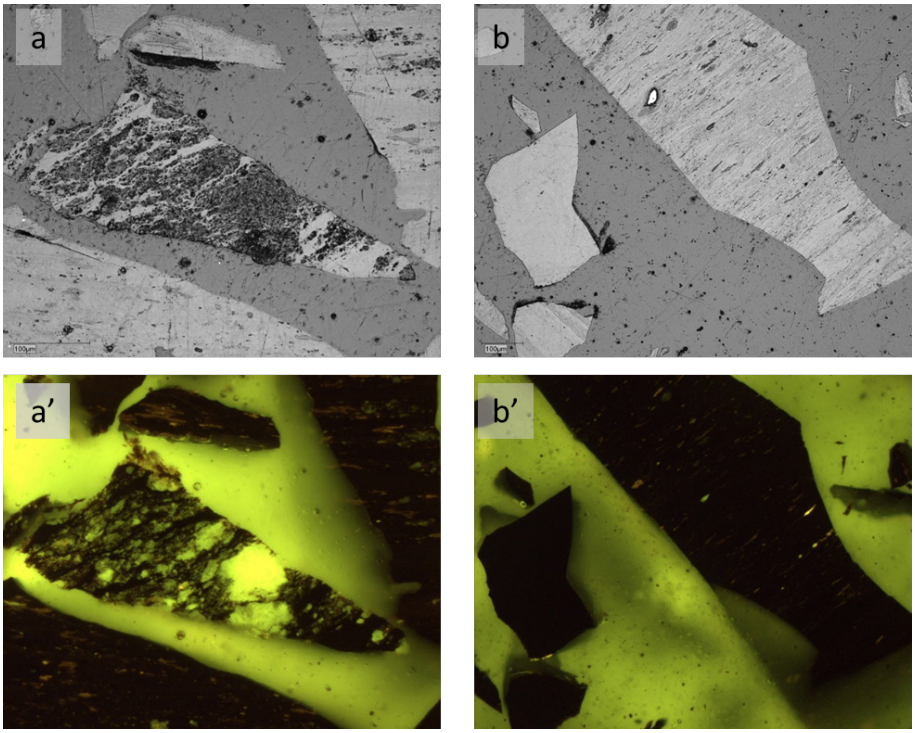

Figure 3. Photomicrographs coal S before treatment. (a) & (b), particle a and particle b, reflected white light; (a') & (b'), particle a and particle b, fluorescent light. Images taken with air objectives (20x).

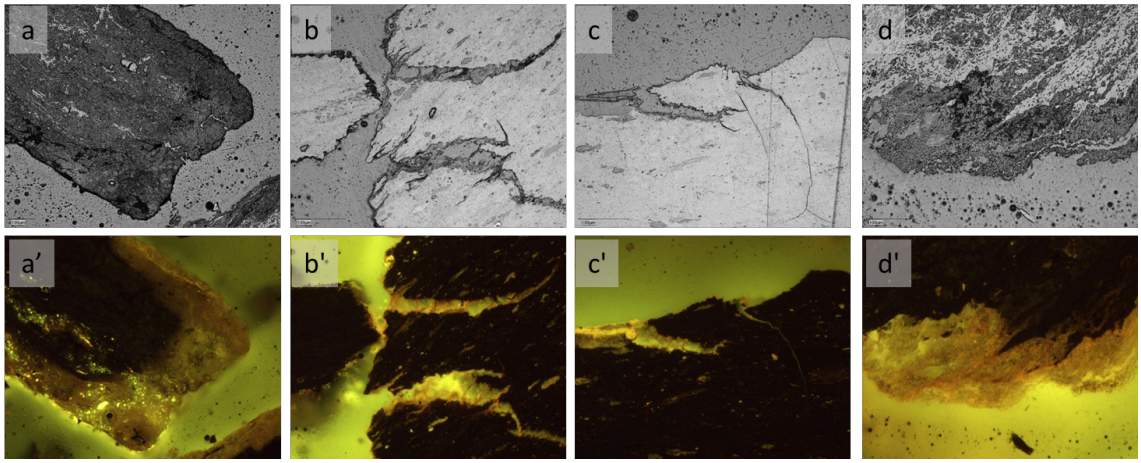

Figure 4. Photomicrographs coal S after treatment. (a), (b), (c) & (d), particle a, b, c, d, reflected white light; (a'), (b'), (c') & (d'), particle a, b, c, d, fluorescent light. Images taken with air objectives (20x).

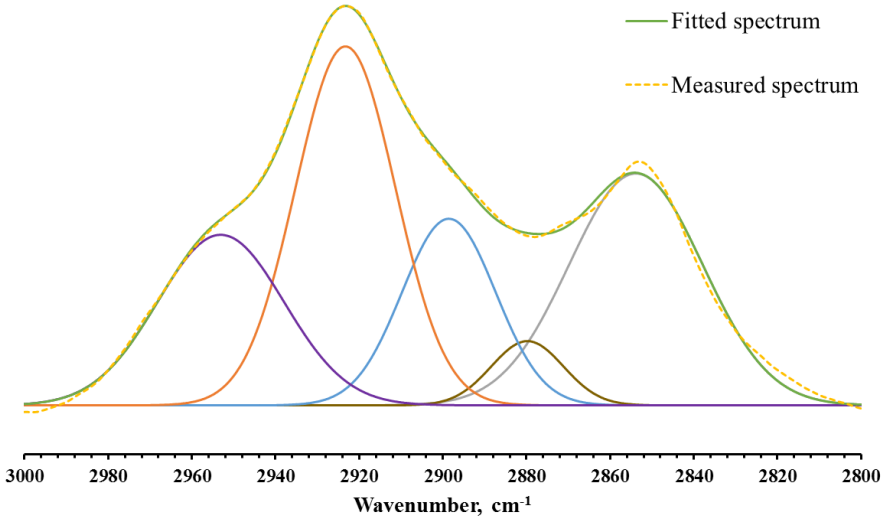

Figure 5. Curve-fitting of coal S spectrum in the wavenumber of 3000-2800 cm^{-1}. Asym. CH_3: CH_3 asymmetrical stretching vibration at ~2950 cm^{-1}; asym. CH_2: CH_2 asymmetrical stretching vibration at ~2920 cm^{-1}; CH: CH stretching vibration at ~2890 cm^{-1}; sym. CH_3: CH_3 symmetrical stretching vibration at ~2870 cm^{-1}; sym. CH_2: CH_2 symmetrical stretching vibration at ~2850 cm^{-1}.

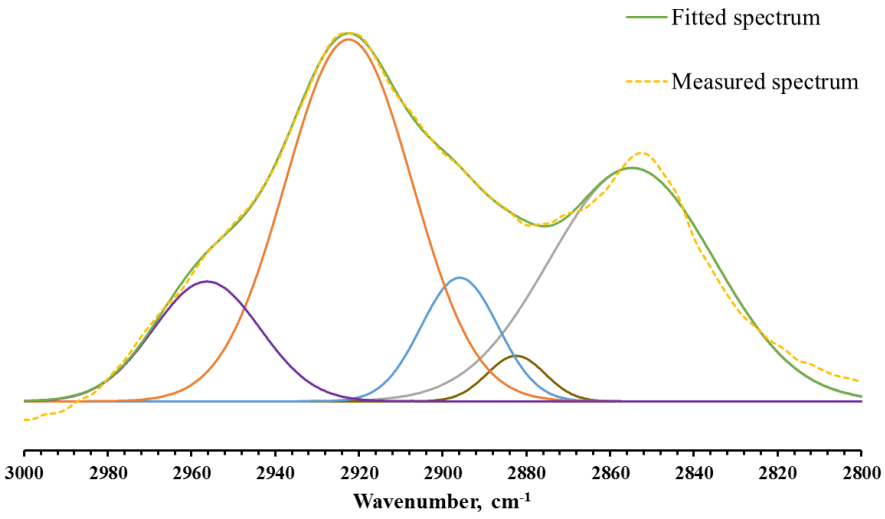

Figure 6. Curve-fitting of coal So spectrum in the wavenumber of 3000-2800 cm^{-1}. Asym. CH_3: CH_3 asymmetrical stretching vibration at ~2950 cm^{-1}; asym. CH_2: CH_2 asymmetrical stretching vibration at ~2920 cm^{-1}; CH: CH stretching vibration at ~2890 cm^{-1}; sym. CH_3: CH_3 symmetrical stretching vibration at ~2870 cm^{-1}; sym. CH_2: CH_2 symmetrical stretching vibration at ~2850 cm^{-1}.

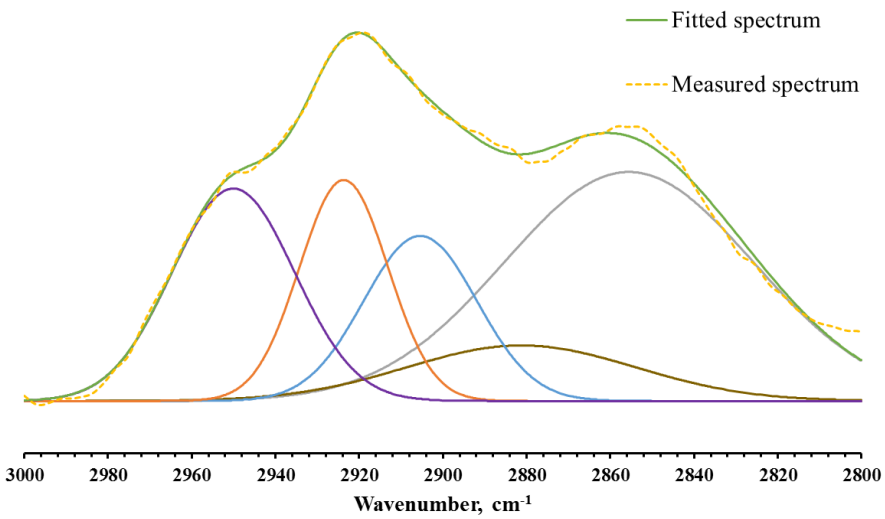

Figure 7. Curve-fitting of coal C spectrum in the wavenumber of 3000-2800 cm^{-1}. Asym. CH_3: CH_3 asymmetrical stretching vibration at ~2950 cm^{-1}; asym. CH_2: CH_2 asymmetrical stretching vibration at ~2920 cm^{-1}; CH: CH stretching vibration at ~2890 cm^{-1}; sym. CH_3: CH_3 symmetrical stretching vibration at ~2870 cm^{-1}; sym. CH_2: CH_2 symmetrical stretching vibration at ~2850 cm^{-1}.

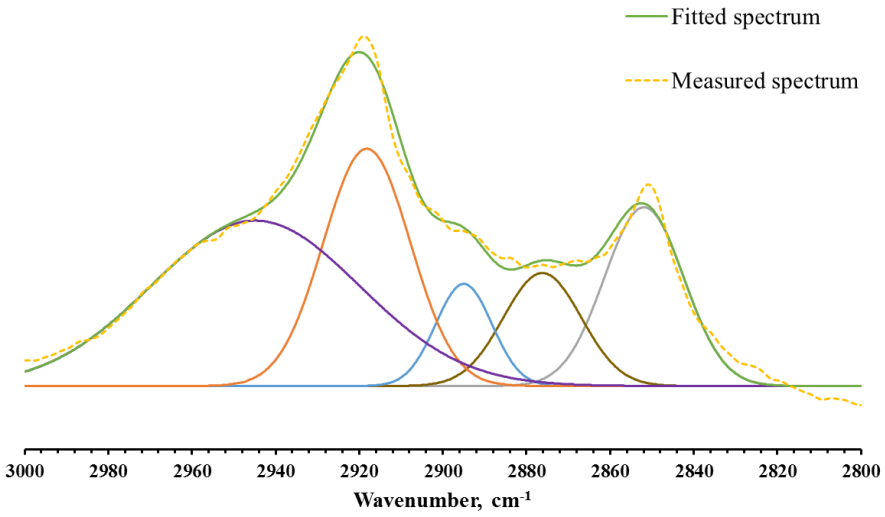

Figure 8. Curve-fitting of coal Bo spectrum in the wavenumber of 3000-2800 cm^{-1}. Asym. CH_3: CH_3 asymmetrical stretching vibration at ~2950 cm^{-1}; asym. CH_2: CH_2 asymmetrical stretching vibration at ~2920 cm^{-1}; CH: CH stretching vibration at ~2890 cm^{-1}; sym. CH_3: CH_3 symmetrical stretching vibration at ~2870 cm^{-1}; sym. CH_2: CH_2 symmetrical stretching vibration at ~2850 cm^{-1}.

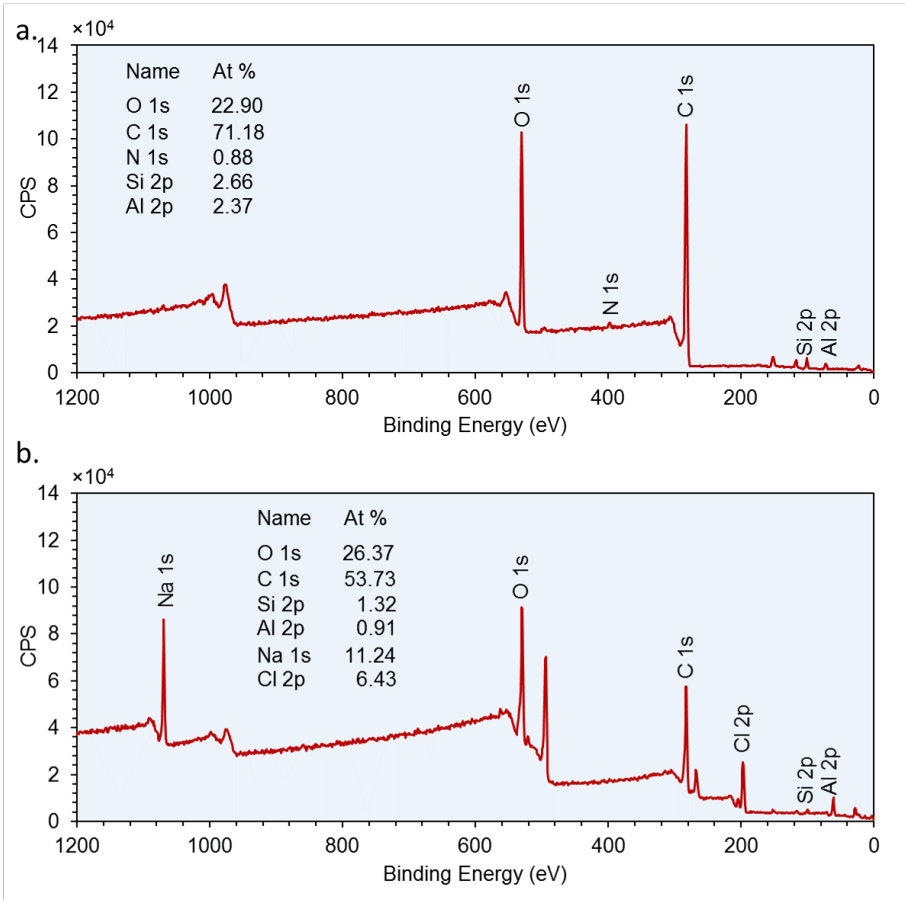

Figure 9. XPS wide scan results for coal S (a) and coal So (b).

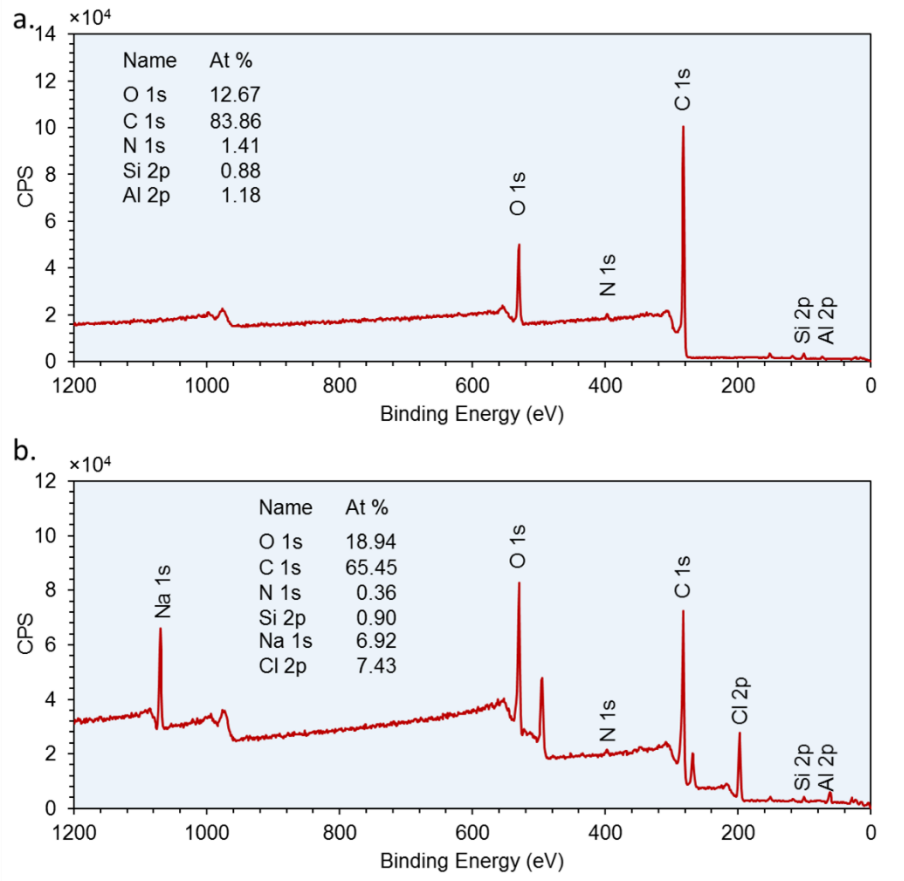

Figure 10. XPS wide scan results for coal B (a) and coal Bo (b).

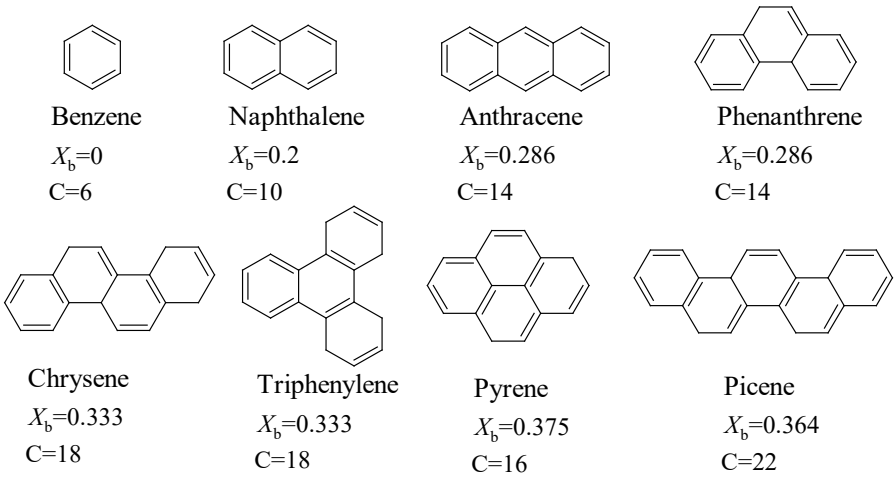

Figure 11. The relationship between structures of example aromatic rings and their lattice parameters x_b and C.

Table 1. Band assignments for the infrared spectra of coals.

Organic Functional Groups		
Wavenumber (cm^{-1})	Assignment	Ref.
3700-3100	O-H groups	[32, 152, 172]
3100-3000	aromatic CHx stretching vibrations	[27, 31, 32, 153-155, 168, 172, 173, 175]
3000-2800	Aliphatic CHx stretching vibrations	[27, 31, 32, 152, 154, 167, 168, 172-175]
~2950	Asymmetric $–CH_3$ stretching	[152, 166]
~2920	Asymmetric $–CH_2–$ stretching	[32, 151, 152, 166]
~2890	methyne C-H stretching	[152, 166]
~2870	Symmetric $–CH_3$-stretching	[152, 166]
~2850	Symmetric $–CH_2$-stretching	[151, 152, 166]
1740-1730	aliphatic ester C=O groups	[31, 153, 167, 168, 171-173, 175]
1710-1700	aromatic carbonyl/carboxyl C=O groups	
1600	Aromatic ring C=C stretching vibration	[32, 151-154, 168, 172, 175]
1450-1435	Aliphatic CH_2 and CH_3 bending vibration	[27, 32, 151-155, 167, 168, 173, 175]
1375-1370	Aliphatic deformation CH_3 absorption bands	[32, 152, 153, 167, 168, 172, 173, 175]
1300-1100	aromatic C-O stretching vibration in phenolic, phenoxy and hydroxyl benzene structures	[152, 153, 155, 167, 168, 175]
1100-1000	Aliphatic C-O ethers, alcohols	[153, 167, 175]
900-700	aromatic nucleus C–H out-of-plane bending	[27, 31, 32, 153-155, 168, 171, 172]
~870	one H deformation	
~815	two adjacent H deformation	
~745	three or four adjacent H deformations	

Table 2: Element analysis in the flooding test solution by ICP-OES for coal BH1.

Element	Unit	Time (hrs from the start) & solution							
		15	30	40	50	60	70	80	120
		4% KCl	1% HCl	1% HCl	1% HCl	1% HCl	1% HCl	1% HCl	4% KCl
Al	mg/L	0.00	0.00	0.00	0.23	0.05	0.03	0.00	0.01

As	mg/L	0.01	0.01	0.01	0.02	0.01	0.01	0.01	0.02
B	mg/L	0.01	0.01	0.01	0.01	0.01	0.01	0.01	0.01
Ba	mg/L	0.01	0.00	0.00	0.00	0.00	0.00	0.00	0.00
Ca	mg/L	1.82	1.75	1.76	3.36	1.76	1.77	1.35	1.30
Cd	mg/L	0.00	0.00	0.00	0.00	0.00	0.00	0.00	0.00
Co	mg/L	0.00	0.00	0.00	0.00	0.00	0.00	0.00	0.00
Cr	mg/L	0.00	0.00	0.00	0.01	0.03	0.05	0.03	0.00
Cu	mg/L	0.00	0.00	0.00	0.17	0.24	0.27	0.01	0.01
Fe	mg/L	0.00	0.00	0.00	0.07	0.17	0.22	0.15	0.02
K	mg/L	843.78	907.37	752.75	856.12	920.54	924.50	931.05	914.50
Mg	mg/L	0.93	0.83	0.81	0.87	0.83	0.90	0.79	0.79
Mn	mg/L	0.00	0.00	0.00	0.02	0.01	0.01	0.00	0.00
Mo	mg/L	0.01	0.00	0.00	0.00	0.01	0.01	0.01	0.00
Na	mg/L	7.86	6.63	6.43	6.49	6.52	6.68	6.22	6.40
Ni	mg/L	0.00	0.01	0.02	0.34	0.50	0.57	0.05	0.03
P	mg/L	0.00	0.00	0.00	0.00	0.00	0.00	0.00	0.00
Pb	mg/L	0.02	0.01	0.00	0.01	0.02	0.01	0.04	0.00
S	mg/L	0.45	0.39	0.33	0.40	0.40	0.41	0.31	0.31
Se	mg/L	0.00	0.00	0.00	0.00	0.00	0.00	0.00	0.00
Zn	mg/L	0.00	0.00	0.00	0.00	0.00	0.00	0.00	0.00

Table 3: Element analysis in the flooding test solution by ICP-OES for coal BH2.

Element	Unit	Time (hrs from the start) & solution						
		6	15	30	45	60	75	90
		4% KCl	1% HCl	1% HCl	1% HCl	1% HCl	1% HCl	4% KCl
Al	mg/L	0.268	0.289	0.224	0.176	0.177	0.931	0.150
As	mg/L	0.007	0.003	0.004	0.005	0.005	0.006	0.007
B	mg/L	0.021	0.013	0.015	0.017	0.018	0.011	0.010
Ba	mg/L	1.128	3.358	3.951	3.569	3.138	1.882	0.658
Ca	mg/L	1.335	9.924	1.868	0.971	0.832	0.739	0.699
Cd	mg/L	0.003	0.005	0.003	0.009	0.007	0.008	0.006
Co	mg/L	0.036	0.046	0.032	0.025	0.040	0.030	0.041
Cr	mg/L	0.061	0.280	0.146	0.249	0.274	0.207	0.072
Cu	mg/L	0.168	1.037	1.507	1.179	1.211	0.953	0.018
Fe	mg/L	2.134	3.669	4.111	5.768	3.308	8.441	5.820
K	mg/L	5005	4293	5018	4862	4776	4601	4446
Mg	mg/L	0.596	0.495	0.473	0.336	0.336	0.346	0.362
Mn	mg/L	0.019	0.107	0.073	0.064	0.058	0.088	0.019
Mo	mg/L	0.039	0.071	0.047	0.027	0.029	0.033	0.034
Na	mg/L	3.6	3.1	3.2	2.9	2.8	2.9	2.7
Ni	mg/L	0.234	0.960	1.296	1.113	1.166	0.935	0.047
P	mg/L	1.701	2.232	2.471	2.163	2.042	1.889	2.521
Pb	mg/L	0.015	0.014	0.004	0.015	0.014	0.010	0.015
S	mg/L	1.517	1.953	1.263	0.920	0.761	0.600	1.121
Se	mg/L	0.011	0.011	0.008	0.007	0.014	0.012	0.012
Si	mg/L	0.621	0.662	0.624	0.635	0.585	0.594	0.544
Sr	mg/L	0.014	0.057	0.028	0.019	0.020	0.012	0.012
Zn	mg/L	0.032	0.050	0.075	0.038	0.068	0.046	0.003